Final Report (No. VI)

to Magistato alle Acqua

& Consorzio Venezia Nuova

HYBRID ELEMENT METHOD FOR SYNCHRONOUS RESONANCE OF MOBILE GATES BY INCIDENT WAVES

A. Theory, validation and examples

Guangda Li[1], Yile Li[2], Mengyi Chen[1] & Chiang C Mei[1],

[1]Department of Civil & Environmental Engineering

[2]Department of Civil & Environmental Engineering

Massachusetts Institute of Technology

August 30, 2004

Contents

List of Figures

List of Tables

Chapter 1

Introduction

This is the final report of a study on the linear resonance of mobile gates for Venice Inlets. It expands and replaces the interim report (No. VI)[1] submitted on June 6, 2004. The overall objective is to calculate and predict the response of gates under normally incident waves from the Adriatic. In earlier studies the gates are assumed to span the full width of an infinitely long channel. The natural modes of the oscillating gates can only be excited nonlinearly through a subharmonic resonance. The real geometry of the three inlets is however quite different, since long jetties are present only on the sea side and the lagoon side is quite open. The inlet is better modeled by a long channel only on the Adriatic side, and open water on the lagoon side. Because of this asymmetry, trapping of the natural modes is no longer perfect; a window now exists for energy exchange with the distant sea. Excitation of a nearly trapped mode by incident waves of the same frequency is possible via a linear mechanism. The goal of the project is to calculate the single-frequency response for a wide range of frequencies, in order to provide the basis for predicting the mean square response to random incident waves described by JONSWAP spectrum, for example.

In Report IV by Adamo & Mei (2003), an analytical theory is described for an inlet with a straight barrier of 20 gates dividing the inlet channel and the open lagoon. For analytical convenience all gates are assumed to be vertical and of rectangular cross section. In the response/frequency diagram, all resonance peaks are quite narrow. Since

[1]Due to numbering errors there are no reports No. III and No. V.

the actual gates will be inclined and of non-simple cross section, the next step is to develop an effective numerical scheme. In this report we describe the basics of the hybrid finite elements method (HFEM), where the far field of the gates is described by analytical series expansions, while the near field surrounding the gates is approximated by discrete finite elements. The principles of this hybrid analytical and discrete analysis is reported here. For the purpose of checking the correctness and numerical accuracy of the mixed method, the associated computer code is first modified for the simple case of vertical gates. Sample computations of gate responses for a wide range of frequencies are then compared with the results in Report IV based on an analytical theory. For this reason, the hybrid element analysis is explained first for the vertical gates. Full implementation of the hybrid method for inclined gates with the design cross sections is finally described. The energy conservation theorem is used to check the overall accuracy. Numerical results for a 7-gate configuration are compared with the measurements at Voltaborrozo for a 1-to-30 model. Sample computations for Chioggia gates with 20 gates are presented. Computer programs for all four inlets with different water-level differences and user's manual are presented in Appendices.

In order to ensure safe and reliable operations, further research on the combined effects of random waves and nonlinear mechanism of subharmonic resonance is needed. Future direction are outlined in the conclusions.

Chapter 2

Mathematical formulation

We assume the fluid to be inviscid and the flow irrotational, and the amplitudes of gates and waves are infinitesimal, so that all boundary conditions can be linearized. The entire fluid domain consists of two parts. One is in the rectangular channel on the sea side (Adriatic) and the other is the open water on the lagoon side. These two parts are separated by the gates at the junction.

For the inclined gates, it is advantageous to use the symmetry about the center axis and study only half of the fluid domain, see Figure 2.1.

In the channel on the sea side, we have the incident (Φ^I), reflected (Φ^R) and radiated wave potentials. The radiation potential on the sea side is denoted by Φ^- distinguished by the superscript $-$. The diffraction problem ($\Phi^D = \Phi^I + \Phi^R$) due to the incident towards and reflected from the fixed gate in the rectangular channel is two-dimensional since we consider only normally incident wave. The radiation problems due to the motion of the gate elements are 3-dimensional. In the open water on the lagoon side, there is only radiated wave denoted by Φ^+.

Let us use the lower case ϕ to denote the spatial component of all potentials Φ, i.e.

$$\Phi(x, y, z, t) = \Re\left(\varphi(x, y, z)e^{-i\omega t}\right) \tag{2.1}$$

The governing equations are summarized below:

(1) Diffraction Potential on the sea side : The diffraction problem is governed by 2-D Laplace equation

$$\varphi^D_{xx} + \varphi^D_{zz} = 0 \tag{2.2}$$

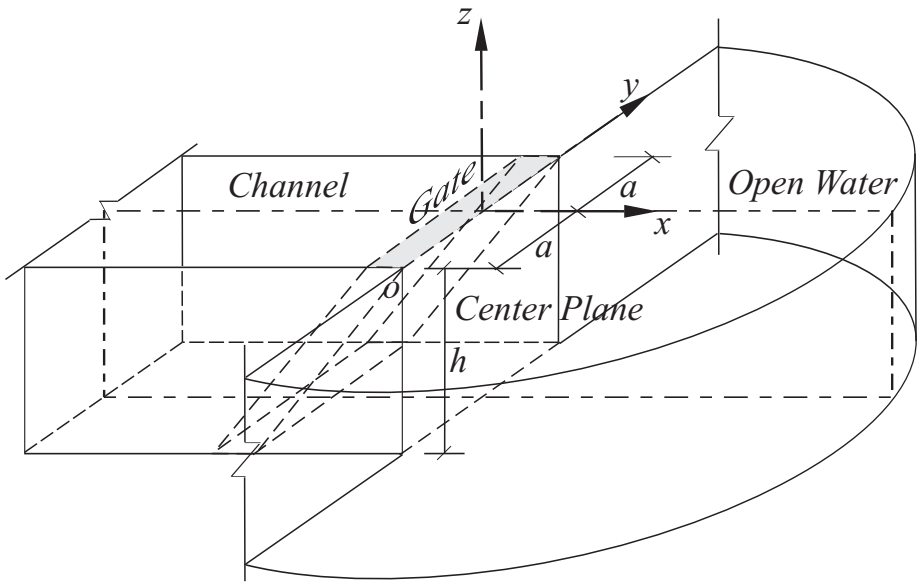

Figure 2.1: Schematic plan

where $\varphi^D = \varphi^I + \varphi^R$, with boundary conditions

$$\frac{\partial \varphi^D}{\partial n} = 0 \tag{2.3}$$

on the wall and the bottom of the channel and fixed gates surface,

$$\frac{\partial \varphi^D}{\partial z} - \frac{\omega^2}{g}\varphi^D = 0, \quad z = 0 \tag{2.4}$$

on the free surface. In addition the Sommerfeld radiation condition must be satisfied by the reflected wave φ^R at the far end of the channel $x \sim -\infty$.

(2) Radiation Potentials on two sides: For N gates across the channel, the barrier has N degrees of freedom. As is common in floating-body dynamics, it is convenient to decompose the radiation problems as follows:

$$\varphi^{\pm} = \sum_{\alpha} \vartheta_\alpha \phi_\alpha^{\pm}, \tag{2.5}$$

where ϑ_α is the unknown angular displacement of gate α with $\alpha = 1, ..., N$. Then $\phi_\alpha^{\pm}$ represents the radiation potential due to unit-amplitude motion of gate α alone and is governed by 3-D Laplace equation

$$\nabla^2 \phi_\alpha^{\pm} = \phi_{xx}^{\pm} + \phi_{yy}^{\pm} + \phi_{zz}^{\pm} = 0 \tag{2.6}$$

with boundary conditions

$$\frac{\partial \phi_\alpha^\pm}{\partial n} = 0, \quad \text{on channel walls, coast lines and sea bed.} \tag{2.7}$$

Moreover, if α denotes the moving gate with all other gates fixed, then we have, on the gate surfaces,

$$\frac{\partial \phi_\beta^\pm}{\partial n} = 0, \quad \beta \neq \alpha \tag{2.8}$$

and

$$\frac{\partial \phi_\alpha^\pm}{\partial n} = -i\omega\{-[n_3(x-X) - n_1(z-Z)]\}, \quad \text{on gate } \alpha \text{ only.} \tag{2.9}$$

where (X, Z) is the center of the gate rotation. In this study the axis is located at $X = 0, Z = -h$. Let the profile of the gate surface be denoted by $z = f(x)$, then the unit normal vector $\mathbf{n}$ pointing into the body is

$$\mathbf{n} = (n_1, n_3) = (-f_x, 1)[1 + (f_x)^2]^{-1/2}$$

On the free surface $z = 0$, we have

$$\frac{\partial \phi_\alpha^\pm}{\partial z} - \frac{\omega^2}{g}\phi_\alpha^\pm = 0 \tag{2.10}$$

Finally $\phi_\alpha^\pm$ must satisfy the Sommerfeld radiation condition and be outgoing in the far field.

The basic steps of the hybrid element method (Chen and Mei,1974; Yue and Mei, 1980; Mei, 1989) involve the following:

1. Divide both sides into near and far-fields. In the near field the geometry can be complex. In the far field the depth is constant. The lateral boundaries are straight and vertical.

2. Express the far-field potentials analytically by eigenfunction expansions with unknown coefficients.

3. Develop variational principles to replace the partial differential equations for the near field, subject to the requirements of continuity of pressure and flux at the borders.

4. Discretize the near field into finite elements, with nodal unknowns.

5. By extremization, get a matrix equation for all the unknown coefficients.

6. Solve the matrix equation, hence the radiation potentials for unit displacement.

7. Solve the dynamical equation of all gates to get the gate displacements.

8. The total potential can now be computed to get wave forces, etc.

On the channel side the geometry is best treated in Cartesian coordinates; the border between the near and far fields is a vertical plane. On the lagoon side polar coordinates are more appropriate; the border is a vertical surface of semi circular plan form.

In this way costly discretization is limited to the near field. We first explain the far field solutions.

Chapter 3

Series solutions in the far field

3.1 The diffraction problem on the sea side

For normal incidence the diffraction problem is two dimensional.

$$\varphi^D = \varphi^I + \varphi^R \tag{3.1.1}$$

where

$$\varphi^I = -\frac{igA}{\omega}\frac{\cosh k(z+h)}{\cosh kh}e^{ikx} \tag{3.1.2}$$

is the normally incident wave. Due to the stationary presence of the stationary gates, the total φ^R in the far field consists of outward-propagating and evanescent modes

$$\varphi^R = -\frac{igA}{\omega}\left\{a_0 f_0(z)\, e^{-ikx} + \sum_{m=1}^{\infty} a_m f_m(z) e^{\bar{k}_m x}\right\} \tag{3.1.3}$$

where k_0 and $\bar{k}_m$ are the real roots of

$$\omega^2 = gk_0 \tanh k_0 h, \quad -\omega^2 = g\bar{k}_m \tan \bar{k}_m h, \quad m = 1, 2, 3, ... \tag{3.1.4}$$

and

$$f_0 = \frac{\sqrt{2}\cosh k_0(z+h)}{\sqrt{h + (g/\omega^2)\sinh^2 k_0 h}}, \quad f_m = \frac{\sqrt{2}\cos \bar{k}_m(z+h)}{\sqrt{h - (g/\omega^2)\sin^2 \bar{k}_m h}} \tag{3.1.5}$$

are orthonormal eigenfunctions in $[-h, 0]$. The complex coefficients a_0 and a_m are unknown. Two dimensional finite-element discretization and variational principles will be discussed later.

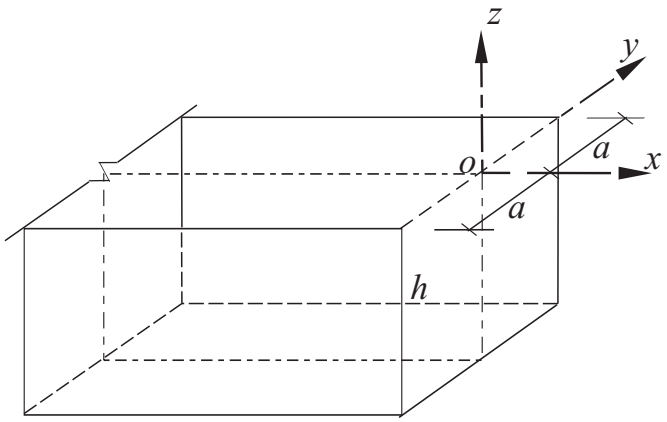

Figure 3.1: Coordinate system on the sea side

3.2 The 3D normalized radiation potentials on the sea side

On the sea side, we shall write ϕ^- for ϕ_α^- for brevity, and assume

$$\phi^-(x,y,z) = X(x)Y(y)Z(z) \tag{3.2.1}$$

we get after substituting (3.2.1) into the Laplace equation,

$$\frac{X''}{X} + \frac{Z''}{Z} + \frac{Y''}{Y} = 0 \tag{3.2.2}$$

The eigen function in y is

$$Y_m = \cos\frac{m\pi y}{a} \tag{3.2.3}$$

so that the boundary conditions on the inlet jetties

$$\frac{\partial\phi^-}{\partial y} = 0, \qquad y = -a \text{ and } a \tag{3.2.4}$$

can be satisfied. Then (3.2.2) becomes

$$\frac{X''}{X} + \frac{Z''}{Z} = -\frac{Y''}{Y} = (\frac{m\pi}{a})^2 \tag{3.2.5}$$

The eigenfunction in z is

$$Z_n = \cosh\left[k_n(z+h)\right] \tag{3.2.6}$$

so that the boundary condition

$$\frac{\partial \phi^-}{\partial z} = 0 \qquad at \quad z = -h \tag{3.2.7}$$

can be satisfied. Substituting Eqn(3.2.6) into the free surface boundary condition

$$\frac{\partial \phi^-}{\partial z} - \frac{\omega^2}{g}\phi^- = 0 \qquad at \quad z = 0 \tag{3.2.8}$$

we get the dispersion relation

$$\omega^2 = gk \tanh kh, \tag{3.2.9}$$

There are infinitely many solutions for k. Among the discrete roots k_0 is real and positive and corresponds to propagating modes. For $n = 1, 2, 3, ...$, $k_n = i\bar{k}_n$ are the positive imaginary roots, or,

$$k_n = i\bar{k}_n, \quad \omega^2 = -g\bar{k}_n \tan \bar{k}_n h, \quad n = 1, 2, 3, ... \tag{3.2.10}$$

and correspond to the evanescent modes. From the Laplace equation we get

$$\frac{X''}{X} = \left(\frac{m\pi}{a}\right)^2 - \frac{Z''}{Z} = \left(\frac{m\pi}{a}\right)^2 - k_n^2 = -\alpha_{mn}^2 \tag{3.2.11}$$

It follows that the eigen function in x is of the generic form

$$X = e^{-i\alpha_{mn}x} \tag{3.2.12}$$

where

$$\alpha_{mn} = \sqrt{k_n^2 - \left(\frac{m\pi}{a}\right)^2} \tag{3.2.13}$$

For $n = 0$, there can in general be M real α_{m0}'s for $m = 0, 1, 2, ...M$. For $m > M$, we have

$$\alpha_{0m} = i\bar{\alpha}_{0m}$$

so that

$$X = e^{\bar{\alpha}_{m0}x}$$

representing evanescent modes. For $n > 0$,

$$\alpha_{nm} = i\bar{\alpha}_{nm} = i\sqrt{\bar{k}_n^2 + (\frac{m\pi}{a})^2}$$

are all imaginary, so that

$$X = e^{\bar{\alpha}_{mn} x}$$

are evanescent modes. The radiation potential is formally,

$$\phi^- = \sum_{m=0}^{\infty} \sum_{n=0}^{\infty} A_{mn} e^{-i\alpha_{mn} x} \cos \frac{m\pi y}{a} \cosh\left[k_n(z+h)\right] \tag{3.2.14}$$

For vertical gates, this series solution is valid in the entire channel due to the simple geometry. Therefore, the coefficients A_{mn} will be determined by satisfying directly the boundary condition at gate surface ($x = 0$). For inclined gates, the above solution is only valid and useful in the far field[1].

3.3 The lagoon side

On the lagoon side only the radiation potentials matter. We consider first the vertical gates and then the inclined gates.

3.3.1 Vertical gates and local coordinates

The analysis for vertical gates is simpler since all stationary gates can be regarded as parts of the coastline. The radiation problem for ϕ_α^+ is formally the same for all α except for a shift of origin. It is sufficient to consider the *local* coordinate system where the x axis is along the center line of the moving gate as shown in Figure 3.2. In term of the global Cartesian coordinates (x, y), the local polar coordinates are:

$$r_\alpha = \sqrt{x^2 + (y - Y_\alpha)^2}, \quad \tan\theta_\alpha = \frac{y - Y\alpha}{x} \tag{3.3.1}$$

and $(0, Y_\alpha)$ refers to the center of gate α. In this section the subscript α will be suppressed for brevity.

After separating the time factor $e^{-i\omega t}$ from $\Phi^+ = \text{Re}\,\{\phi^+ e^{-i\omega t}\}$, the radiation potential on the lagoon side ϕ^+ satisfies the Laplace equation in local polar coordinates

$$\frac{1}{r}\frac{\partial}{\partial r}\left(r\frac{\partial \phi^+}{\partial r}\right) + \frac{1}{r^2}\frac{\partial^2 \phi^+}{\partial \theta^2} + \frac{\partial^2 \phi^+}{\partial z^2} = 0 \tag{3.3.2}$$

[1]Later in the numerical method we shall take advantage of the symmetry with respect to the centerline (x axis) and only use half of the channel in $0 < y < a$. The same solution is still valid in the far field.

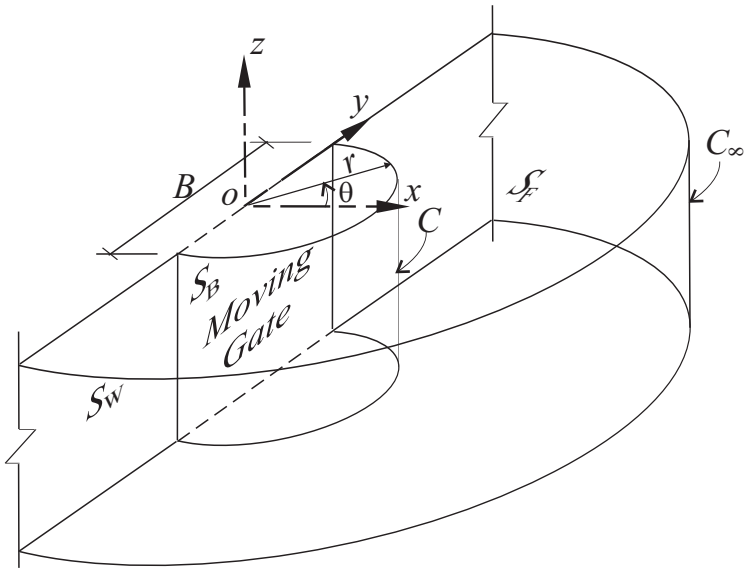

Figure 3.2: Local coordinate system for vertical gates

Separation of variables gives

$$\phi^+(r,\theta,z) = R(r)\Theta(\theta)Z(z) \tag{3.3.3}$$

Upon substituting (3.3.3) into (3.3.2), we get

$$\frac{R''}{R} + \frac{1}{r}\frac{R'}{R} + \frac{1}{r^2}\frac{\Theta''}{\Theta} + \frac{Z''}{Z} = 0 \tag{3.3.4}$$

The eigen function in z is

$$Z_n = \cosh\left[k_n(z+h)\right] \tag{3.3.5}$$

subject to the dispersion relation

$$\omega^2 = k_n g \tanh k_n h, \quad n = 0, 1, 2, 3, . \tag{3.3.6}$$

with $k_0 =$ real, $k_n = i\bar{k}_n$, with $\bar{k}_n =$ real. Symmetry of our problem requires no velocity across the center plane, i.e.

$$u_\theta = \frac{\partial \phi^+}{\partial \theta} = 0 \qquad at \;\; \theta = 0$$

Furthermore, no flux along the banks $\theta = \pm\frac{\pi}{2}$ requires

$$\frac{\partial \phi^+}{\partial \theta} = 0 \qquad at \;\; \theta = \pm\frac{\pi}{2} \tag{3.3.7}$$

These boundary conditions lead to the eigen functions in θ,

$$\Theta_m = \cos 2m\theta, \quad m = 1, 2, 3, ..., \cdots \tag{3.3.8}$$

From (3.3.4) the radial eigenfunction is governed by Bessel's equation

$$r^2 R'' + rR' + (k_n^2 r^2 - (2m)^2)R = 0 \tag{3.3.9}$$

For $n = 0$, the general solution is

$$R_{m0}(r) = B_{m0} H_{2m}^{(1)}(k_0 r) + B'_{m0} H_{2m}^{(2)}(k_0 r) \tag{3.3.10}$$

where $H_{2m}^{(1)}, H_{2m}^{(2)}$ are the Hankel functions of the first and second kind. As the argument $|x| \to \infty$, they behave asymptotically as

$$H_{2m}^{(1)}(x) \sim \sqrt{\frac{2}{\pi x}} e^{i(x - m\pi - \frac{\pi}{4})}; \qquad H_{2m}^{(2)}(x) \sim \sqrt{\frac{2}{\pi x}} e^{-i(x - \ m\pi - \frac{\pi}{4})}$$

Imposing the radiation condition, only outgoing waves are permitted at $r \to \infty$. Only $H_{2m}^{(1)}(k_0 r)$ can be kept.

For imaginary roots, $k_n = i\bar{k}_n$, $n = 1, 2, 3...$, Eqn (3.3.9) can be written as

$$r^2 R'' + rR' - \left[\bar{k}_n^2 r^2 + (2m)^2\right] R = 0 \tag{3.3.11}$$

The general solution is

$$R_{mn}(r) = B_{mn} I_{2m}(\bar{k}_n r) + B'_{mn} K_{2m}(\bar{k}_n r) \tag{3.3.12}$$

where I_{2m}, K_{2m} are the modified Hankel function of the first and second kind. As the argument $x \to \infty$,

$$I_{2m}(x) \to \infty; \qquad K_{2m}(x) \to 0$$

Boundedness at $r \to \infty$ excludes I_{2m} from our solution. The admissible eigenfunctions are proportional to

$$K_{2m}(\bar{k}_n r) = \frac{\pi}{2} i^{2m+1} H_{2m}^{(1)}(i\bar{k}_n r)$$

Finally the potential in the far field on the sea side can be written as,

$$\phi^+ = \sum_{m=0}^{\infty} \sum_{n=0}^{\infty} B_{mn} \cos 2m\theta \cosh\left[k_n(z+h)\right] H_{2m}^{(1)}(k_n r) \tag{3.3.13}$$

We emphasize that the above results are to be interpreted finally in terms of the global coordinates, i.e., we must replace for each potential ϕ_α^+ :

$$r \to r_\alpha = \sqrt{x^2 + (y - Y_\alpha)^2}, \quad \theta \to \theta_\alpha \tag{3.3.14}$$

where

$$\tan\theta_\alpha = \frac{y - Y\alpha}{x} \tag{3.3.15}$$

and $(0, Y_\alpha)$ refers to the center of gate α. Thus,

$$\phi_\alpha^+ = \sum_{m=0}^{\infty}\sum_{n=0}^{\infty} B_{mn}^{(\alpha)} \cos 2m\theta_\alpha \cosh\left[k_n(z+h)\right] H_{2m}^{(1)}(k_n r_\alpha) \tag{3.3.16}$$

3.3.2 Inclined gates and global coordinates

For inclined gates, we cannot use the local coordinates and must use the global coordinates where the origin is at the center of the vertical plane flush with the junction line (the lagoon coast). The far field solution for α is therefore given by

$$\phi_\alpha^+ = \sum_{m=0}^{\infty}\sum_{n=0}^{\infty} B_{mn}^{(\alpha)} \cos 2m\theta \cosh\left[k_n(z+h)\right] H_{2m}^{(1)}(k_n r) \tag{3.3.17}$$

For computational economy in the later method of HFEM, we shall use half of the fluid domain as shown in Figure 3.3. Eq. (3.3.17) of course still applies.

In the Hybrid Finite Element Method (HFEM), the coefficients $B_{mn}^{(\alpha)}$ will be determined by matching with the near field solution, where discrete finite elements cover all of the inclined gates. For large order but finite argument, Hankel functions of the first kind become very large. For example, $H_{20}^{(1)}(0.3) = 9.7978 \times 10^{15} - 1.1658 \times 10^{33} i$. To avoid numerical difficulty we shall use $H_{2m}^{(1)}(k_n r_C)$ to normalize the Hankel eigenfunctions in r, where r_C is the radius of the semi circle separating the near and far fields. Similarly we use $\cosh(k_n h)$ to normalize the eigenfunctions in z. Introducing new coefficient $\nu_{mn}^{(\alpha)}$, we can rewrite (3.3.17) as

$$\phi_\alpha^+ = \sum_{m=0}^{\infty}\sum_{n=0}^{\infty} \nu_{mn}^{(\alpha)} \cos 2m\theta \frac{\cosh\left[k_n(z+h)\right]}{\cosh(k_n h)} \frac{H_{2m}^{(1)}(k_n r)}{H_{2m}^{(1)}(k_n r_C)} \tag{3.3.18}$$

with

$$B_{mn}^{(\alpha)} = \frac{\nu_{mn}^{(\alpha)}}{\cosh(k_n h) H_{2m}^{(1)}(k_n r_C)}$$

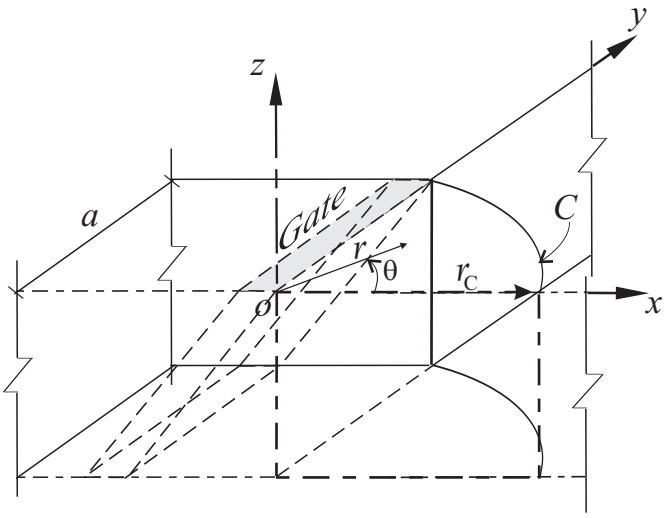

Figure 3.3: Global coordinate system for inclined gates

Chapter 4

Hybrid Finite Element Method

4.1 Variational principles and HFEM

We shall first derive the variational principle for our Hybrid Finite Element Method (HFEM) from the governing equations for a radiation problem. To facilitate understanding of the mathematics we shall also reverse the reasoning and start from the variational principle then prove its equivalence to the boundary value problem. Since the mathematical procedure is the same for the sea side and the lagoon side, we use a generic ϕ without superscripts to represent either ϕ^- or ϕ^+ in this section.

4.1.1 From BVP to Variational principle

We shall employ Galerkin's method to derive the variational principle directly from the boundary value problem. Let us first divide the fluid domain into the near and far fields, V and $\tilde{V}$, separated by a vertical surface C. The corresponding potentials are ϕ and $\tilde{\phi}$ respectively. These potentials must satisfy Laplace equation and all the boundary conditions in their own domains; they and their normal derivatives must be continuous across C. The far-field potential $\tilde{\phi}$ must also obey the radiation condition at infinity.

According to Galerkin's method, we require that for any approximate solutions $\phi \in V$ and $\tilde{\phi} \in \tilde{V}$,

$$\int_V \nabla^2\phi \ \delta\phi dV \ = \ \int_{S_F} \left(\frac{\partial\phi}{\partial n} - \frac{\omega^2}{g}\phi\right) \delta\phi dS + \int_{S_B} \left(\frac{\partial\phi}{\partial n} - \mathcal{U}_n\right) \delta\phi dS +$$

$$+ \int_C \left(\frac{\partial \phi}{\partial n} - \frac{\partial \tilde{\phi}}{\partial n} \right) \delta\phi dS \tag{4.1.1}$$

for any weight functions $\delta\phi$ and $\tilde{\phi}$, which vary within the same solution space as ϕ and $\tilde{\phi}$. S_B and S_F are the parts of the barrier and free surface inside V.

On the left-hand side, integrating by part gives

$$\begin{aligned} \int_V \nabla^2\phi\delta\phi dV &= \int_V \left[\nabla \cdot (\delta\phi\nabla\phi) - \int_V \nabla\phi \cdot \nabla\delta\phi \right] dV \\ &= \int_S (\delta\phi\nabla\phi) \cdot \vec{n} dS - \int_V \frac{1}{2}\delta(\nabla\phi)^2 dV \\ &= \int_{S_B+S_F+B+C} \delta\phi \frac{\partial\phi}{\partial n} dS - \delta \int_V \frac{1}{2}(\nabla\phi)^2 dV \end{aligned}$$

where use is made of Gauss' divergence theorem. With this result (4.1.1) can be rewritten as

$$-\delta \int_V \frac{1}{2}(\nabla\phi)^2 dV = -\delta \int_{S_F} \frac{\omega^2}{2g}\phi^2 dS - \delta \int_{S_B} \mathcal{U}_n \phi dS - \int_C \frac{\partial\tilde{\phi}}{\partial n}\delta\phi dS \tag{4.1.2}$$

We shall now rewrite the last term in the form of a first variation

$$\delta \int (.)$$

Note first that

$$-\int_C \frac{\partial\tilde{\phi}}{\partial n}\delta\phi dS = -\delta \int_C \frac{\partial\tilde{\phi}}{\partial n}\phi dS + \int_C \frac{\partial\delta\tilde{\phi}}{\partial n}\phi dS \tag{4.1.3}$$

To proceed further we add two integrals which are zero in view of the continuity conditions and the radiation condition at infinity,

$$\begin{aligned} -\int_C \frac{\partial\tilde{\phi}}{\partial n}\delta\phi dS &= -\delta \int_C \frac{\partial\tilde{\phi}}{\partial n}\phi dS + \int_C \frac{\partial\delta\tilde{\phi}}{\partial n}\phi dS \\ &+ \int_C (\tilde{\phi} - \phi)\frac{\partial\delta\tilde{\phi}}{\partial n} dS + \frac{1}{2}\int_C \left(\delta\tilde{\phi}\frac{\partial\tilde{\phi}}{\partial n} - \tilde{\phi}\frac{\partial\delta\tilde{\phi}}{\partial n} \right) dS \end{aligned} \tag{4.1.4}$$

In particular the first added integral vanishes because of continuity of pressure. To show that the second vanishes we use the fact that both $\tilde{\phi}$ and $\delta\tilde{\phi}$ satisfy Laplace's equation and the same boundary conditions. By Green's formula,

$$\frac{1}{2}\int_C \left(\delta\tilde{\phi}\frac{\partial\tilde{\phi}}{\partial n} - \tilde{\phi}\frac{\partial\delta\tilde{\phi}}{\partial n} \right) dS + \frac{1}{2}\int_{C_\infty} \left(\delta\tilde{\phi}\frac{\partial\tilde{\phi}}{\partial n} - \tilde{\phi}\frac{\partial\delta\tilde{\phi}}{\partial n} \right) dS = 0$$

The integral along C_∞ vanishes by virtue of the radiation condition, hence the integral along C also vanishes.

After some cancelations and combinations, the preceding equation (4.1.4) becomes

$$-\delta\int_C \frac{\partial\tilde{\phi}}{\partial n}\phi dS + \frac{1}{2}\int_C \left(\delta\tilde{\phi}\frac{\partial\tilde{\phi}}{\partial n} + \tilde{\phi}\frac{\partial\delta\tilde{\phi}}{\partial n}\right) dS = -\delta\int_C \frac{\partial\tilde{\phi}}{\partial n}\phi dS + \frac{1}{2}\delta\int_C \tilde{\phi}\frac{\partial\tilde{\phi}}{\partial n}dS$$
$$= \delta\int_C \left(\frac{1}{2}\tilde{\phi} - \phi\right)\frac{\partial\tilde{\phi}}{\partial n}dS \tag{4.1.5}$$

Finally by using (4.1.3) (4.1.4)(4.1.5) in (4.1.2) we rewrite the Galerkin formula as a variational principle

$$\delta\mathcal{F}(\phi,\tilde{\phi}) = 0, \tag{4.1.6}$$

where

$$\mathcal{F}(\phi,\tilde{\phi}) = \int_V \frac{1}{2}(\nabla\phi)^2 dV - \int_{S_F}\frac{\omega^2}{2g}\phi^2 dS - \int_{S_B}\mathcal{U}_n\phi dS + \int_C\left(\frac{\tilde{\phi}}{2} - \phi\right)\frac{\partial\tilde{\phi}}{\partial n}dS \tag{4.1.7}$$

4.1.2 From variational principle to BVP

Alternatively, it can be proven that the boundary-value problem defined by (Eqs. (2.6) to (2.10) is the result of the stationarity of the functional defined in (4.1.7).

The first variation of (4.1.7) is

$$\delta\mathcal{F} = \int_V \nabla\phi\cdot\nabla\delta\phi dV - \int_{S_F}\frac{\omega^2}{g}\phi\delta\phi dS - \int_{S_B}\mathcal{U}_n\delta\phi dS + \int_C\left[\left(\frac{\delta\tilde{\phi}}{2} - \delta\phi\right)\frac{\partial\tilde{\phi}}{\partial n} + \left(\frac{\tilde{\phi}}{2} - \phi\right)\frac{\partial\delta\tilde{\phi}}{\partial n}\right]dS$$

Integrating by parts, the first term on the right-hand side gives

$$\begin{aligned}\int_V \nabla\phi\cdot\nabla\delta\phi dV &= \int_V\left[\nabla\cdot(\delta\phi\nabla\phi) - \delta\phi\nabla^2\phi\right]dV \\ &= \int_S(\delta\phi\nabla\phi)\cdot\vec{n}dS - \int_V\delta\phi\nabla^2\phi dV \\ &= \int_{S_B+S_F+B+C}\delta\phi\frac{\partial\phi}{\partial n}dS - \int_V\delta\phi\nabla^2\phi dV\end{aligned}$$

where Gauss' divergence theorem is used. Collecting the terms according to the integration domains, we get

$$\begin{aligned}\delta\mathcal{F} &= -\int_V\nabla^2\phi\delta\phi dV + \int_{S_F}\left(\frac{\partial\phi}{\partial n} - \frac{\omega^2}{g}\phi\right)\delta\phi dS \\ &+ \int_{S_B}\left(\frac{\partial\phi}{\partial n} - \mathcal{U}_n\right)\delta\phi dS + \int_B\delta\phi\frac{\partial\phi}{\partial n}dS \\ &+ \int_C\left[\delta\phi\frac{\partial\phi}{\partial n} + (\frac{\delta\tilde{\phi}}{2} - \delta\phi)\frac{\partial\tilde{\phi}}{\partial n} + (\frac{\tilde{\phi}}{2} - \phi)\frac{\partial\delta\tilde{\phi}}{\partial n}\right]dS\end{aligned}$$

After some rearrangement, the last integral can be written as

$$\int_C \left(\frac{\partial\phi}{\partial n} - \frac{\partial\tilde{\phi}}{\partial n}\right)\delta\phi dS + \int_C \left(\phi - \tilde{\phi}\right)\frac{\partial\delta\tilde{\phi}}{\partial n}dS + \frac{1}{2}\int_C \left(\delta\tilde{\phi}\frac{\partial\tilde{\phi}}{\partial n} - \tilde{\phi}\frac{\partial\delta\tilde{\phi}}{\partial n}\right)dS$$

Since $\tilde{\phi}$ and $\delta\tilde{\phi}$ are harmonic in the outer region, we can replace the integral domain C with $C_\infty + S_W + S_F + B$ by Green's theorem. Finally this integral goes to zero due to the radiation condition at infinity and boundary conditions on the wall S_W ($\frac{\partial\tilde{\phi}}{\partial n} = 0$), the bottom B ($\frac{\partial\tilde{\phi}}{\partial n} = 0$) and the free surface S_F ($\frac{\partial\tilde{\phi}}{\partial n} = \frac{\omega^2}{g}\tilde{\phi}$). Thus the solution to the boundary value problem is equivalent to the stationary of the functional (4.1.7).

4.1.3 The procedure of Hybrid Finite Element Method (HFEM)

When trial functions are introduced to approximate the exact solution, unknown coefficients appear in the functional. Application of Rayleigh-Ritz procedure to minimize the functional leads to algebraic equations for these unknown coefficients, which will be solved numerically. For convenience, we first label various integrals in (4.1.7) as follows

$$\mathcal{F} = \overbrace{\int_V \frac{1}{2}(\nabla\phi)^2 dV}^{I_1} + \overbrace{\int_{S_F} -\frac{\omega^2}{2g}\phi^2 dS}^{I_2} + \overbrace{\int_C \frac{\tilde{\phi}}{2}\frac{\partial\tilde{\phi}}{\partial n}dS}^{I_3} + \overbrace{\int_C -\phi\frac{\partial\tilde{\phi}}{\partial n}dS}^{I_4} + \overbrace{\int_{S_B} -\mathcal{U}_n\phi dS}^{I_5} \quad (4.1.8)$$

$\mathcal{U}_n$ is the normal velocity of the gate for unit amplitude of angular displacement. The scheme of HFEM is as follows:

1. Discretize the near field of the gate with finite elements. Introduce an interpolation function for each element to approximate the exact solution ϕ, with unknown nodal potentials $\hat{\phi}$.

2. Represent the far-field $\tilde{\phi}$ by eigenfunction expansions and treat series coefficients $\hat{\nu}$ as unknowns.

3. Combine the solutions from (1) and (2) into Eq.(4.1.7) and evaluate the integrals.

4. Extremize the functional and get algebraic equations for $\hat{\phi}$, $\hat{\nu}$. Solve the algebraic equations.

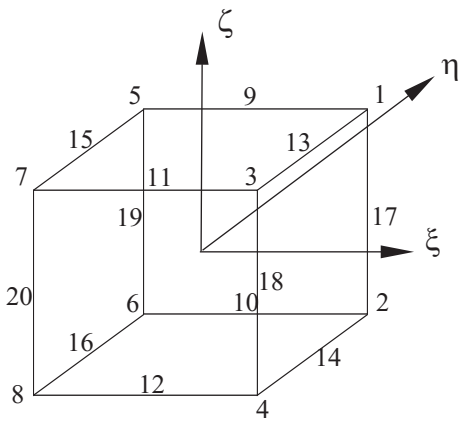

Figure 4.1: 20-node isoparametric cube element

In principle the imaginary boundary C can be chosen arbitrarily as long as it encloses the complex geometry. We naturally choose a l semicircle (refer to Figure 3.3.1) for convenience.

The theory described so far applies equally for both two and three dimensional problems.

4.2 3-D FEM discretization

4.2.1 General cubic element

For 3-D problems, we employ 20-node isoparametric cube elements as shown in Figure 4.1. For each element, the global coordinates (x, y, z) are related to local coordinates (ξ, η, ζ) by the interpolation functions $h_i(\xi, \eta, \zeta)$ in the following way:

$$x = \sum_{i=1}^{20} h_i(\xi, \eta, \zeta) x_i \,;\; y = \sum_{i=1}^{20} h_i(\xi, \eta, \zeta) y_i \,;\; z = \sum_{i=1}^{20} h_i(\xi, \eta, \zeta) z_i \tag{4.2.9}$$

where $(x_i,\, y_i,\, z_i)$ are the global coordinates of the nodes and the interpolation functions are defined as follows (refer to Figure 4.1):

$$h_i = \frac{1}{8}(1 + \xi_i\xi)(1 + \eta_i\eta)(1 + \zeta_i\zeta)(\xi_i\xi + \eta_i\eta + \zeta_i\zeta - 2), \quad i = 1 \sim 8;$$

$$h_i = \frac{1}{4}(1 - \xi^2)(1 + \eta_i\eta)(1 + \zeta_i\zeta), \quad i = 9 \sim 12;$$

$$h_i = \frac{1}{4}(1-\eta^2)(1+\xi_i\xi)(1+\zeta_i\zeta), \quad i = 13 \sim 16;$$

$$h_i = \frac{1}{4}(1-\zeta^2)(1+\xi_i\xi)(1+\eta_i\eta), \quad i = 17 \sim 20;$$

with

$$\xi_i,\ \eta_i,\ \zeta_i = \pm 1$$

Similarly, the potential within the element is related to the nodal potential ϕ_i in the same way:

$$\phi(x_{(\xi,\eta,\zeta)}, y_{(\xi,\eta,\zeta)}, z_{(\xi,\eta,\zeta)}) = \sum_{i=1}^{20} h_i(\xi,\eta,\zeta)\phi_i$$

In matrix form,

$$\phi = \begin{bmatrix} h_1 & h_2 & \cdots & h_{20} \end{bmatrix} \begin{bmatrix} \phi_1 \\ \phi_2 \\ \vdots \\ \phi_{20} \end{bmatrix} = \mathbf{H}\hat{\phi} \tag{4.2.10}$$

$$(\nabla\phi)^2 = (\frac{\partial\phi}{\partial x})^2 + (\frac{\partial\phi}{\partial y})^2 + (\frac{\partial\phi}{\partial z})^2 = \begin{bmatrix} \frac{\partial\phi}{\partial x} & \frac{\partial\phi}{\partial y} & \frac{\partial\phi}{\partial z} \end{bmatrix} \begin{bmatrix} \frac{\partial\phi}{\partial x} \\ \frac{\partial\phi}{\partial y} \\ \frac{\partial\phi}{\partial z} \end{bmatrix} \tag{4.2.11}$$

By chain rule,

$$\begin{bmatrix} \frac{\partial}{\partial\xi} \\ \frac{\partial}{\partial\eta} \\ \frac{\partial}{\partial\zeta} \end{bmatrix} = \begin{bmatrix} \frac{\partial x}{\partial\xi} & \frac{\partial y}{\partial\xi} & \frac{\partial z}{\partial\xi} \\ \frac{\partial x}{\partial\eta} & \frac{\partial y}{\partial\eta} & \frac{\partial z}{\partial\eta} \\ \frac{\partial x}{\partial\zeta} & \frac{\partial y}{\partial\zeta} & \frac{\partial z}{\partial\zeta} \end{bmatrix} \begin{bmatrix} \frac{\partial}{\partial x} \\ \frac{\partial}{\partial y} \\ \frac{\partial}{\partial z} \end{bmatrix} = \mathbf{J} \begin{bmatrix} \frac{\partial}{\partial x} \\ \frac{\partial}{\partial y} \\ \frac{\partial}{\partial z} \end{bmatrix}$$

For a proper isoparametric element, the Jacobian determinant of the transformation does not vanish

$$det(\mathbf{J}) = \begin{vmatrix} \frac{\partial x}{\partial\xi} & \frac{\partial y}{\partial\xi} & \frac{\partial z}{\partial\xi} \\ \frac{\partial x}{\partial\eta} & \frac{\partial y}{\partial\eta} & \frac{\partial z}{\partial\eta} \\ \frac{\partial x}{\partial\zeta} & \frac{\partial y}{\partial\zeta} & \frac{\partial z}{\partial\zeta} \end{vmatrix} \neq 0$$

and its inverse $\mathbf{J}^{-1}$ exists. Therefore

$$\begin{bmatrix} \frac{\partial\phi}{\partial x} \\ \frac{\partial\phi}{\partial y} \\ \frac{\partial\phi}{\partial z} \end{bmatrix} = \mathbf{J}^{-1} \begin{bmatrix} \frac{\partial\phi}{\partial\xi} \\ \frac{\partial\phi}{\partial\eta} \\ \frac{\partial\phi}{\partial\zeta} \end{bmatrix} = \mathbf{J}^{-1} \begin{bmatrix} \mathbf{H}_{,\xi} \\ \mathbf{H}_{,\eta} \\ \mathbf{H}_{,\zeta} \end{bmatrix} \hat{\phi} = \mathbf{B}\hat{\phi}$$

where use is made of (4.2.10) and "$_{,\xi}$" denotes "$\frac{\partial}{\partial \xi}$" and so on. The $\mathbf{B}$ matrix is defined as

$$\mathbf{B} = \mathbf{J}^{-1} \begin{bmatrix} h_{1,\xi} & h_{2,\xi} & \cdots & h_{20,\xi} \\ h_{1,\eta} & h_{2,\eta} & \cdots & h_{20,\eta} \\ h_{1,\zeta} & h_{2,\zeta} & \cdots & h_{20,\zeta} \end{bmatrix}$$

where

$$h_{i,\xi} = \frac{1}{8}\xi_i(2\xi_i\xi + \eta_i\eta + \zeta_i\zeta - 1)(1 + \eta_i\eta)(1 + \zeta_i\zeta), \quad i = 1 \sim 8;$$

$$h_{i,\xi} = -\frac{1}{2}\xi(1 + \eta_i\eta)(1 + \zeta_i\zeta), \quad i = 9 \sim 12;$$

$$h_{i,\xi} = \frac{1}{4}\xi_i(1 - \eta^2)(1 + \zeta_i\zeta), \quad i = 13 \sim 16;$$

$$h_{i,\xi} = \frac{1}{4}\xi_i(1 - \zeta^2)(1 + \eta_i\eta), \quad i = 17 \sim 20;$$

$$h_{i,\eta} = \frac{1}{8}\eta_i(2\eta_i\eta + \xi_i\xi + \zeta_i\zeta - 1)(1 + \xi_i\xi)(1 + \zeta_i\zeta), \quad i = 1 \sim 8;$$

$$h_{i,\eta} = \frac{1}{4}\eta_i(1 - \xi^2)(1 + \zeta_i\zeta), \quad i = 9 \sim 12;$$

$$h_{i,\eta} = -\frac{1}{2}\eta(1 + \xi_i\xi)(1 + \zeta_i\zeta), \quad i = 13 \sim 16;$$

$$h_{i,\eta} = \frac{1}{4}\eta_i(1 - \zeta^2)(1 + \xi_i\xi), \quad i = 17 \sim 20;$$

$$h_{i,\zeta} = \frac{1}{8}\zeta_i(2\zeta_i\zeta + \xi_i\xi + \eta_i\eta - 1)(1 + \xi_i\xi)(1 + \eta_i\eta), \quad i = 1 \sim 8;$$

$$h_{i,\zeta} = \frac{1}{4}\zeta_i(1 - \xi^2)(1 + \eta_i\eta), \quad i = 9 \sim 12;$$

$$h_{i,\zeta} = \frac{1}{4}\zeta_i(1 - \eta^2)(1 + \xi_i\xi), \quad i = 13 \sim 16;$$

$$h_{i,\zeta} = -\frac{1}{2}\zeta(1 + \xi_i\xi)(1 + \eta_i\eta), \quad i = 17 \sim 20;$$

with

$$\xi_i,\ \eta_i,\ \zeta_i = \pm 1$$

The Jacobi for each element can be obtained by making use of (4.2.9)

$$\mathbf{J} = \begin{bmatrix} h_{1,\xi} & h_{2,\xi} & \cdots & h_{20,\xi} \\ h_{1,\eta} & h_{2,\eta} & \cdots & h_{20,\eta} \\ h_{1,\zeta} & h_{2,\zeta} & \cdots & h_{20,\zeta} \end{bmatrix} \begin{bmatrix} x_1 & y_1 & z_1 \\ x_2 & y_2 & z_2 \\ \vdots & \vdots & \vdots \\ x_{20} & y_{20} & z_{20} \end{bmatrix}$$

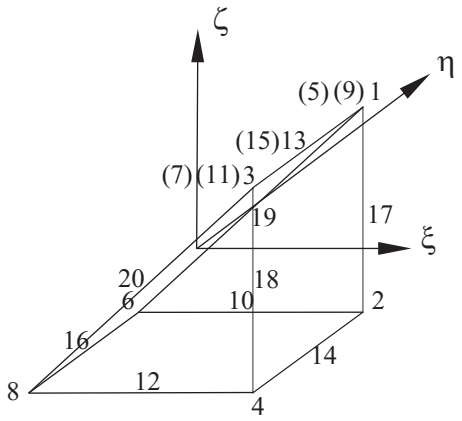

Figure 4.2: Degenerate prism element

4.2.2 Degenerate prism element

For better fit to the inclined gate surface, we use another kind of 3-D element, degenerate prism element, as shown in Figure 4.2. Later on we will see that just one layer of this kind of elements on the inclined surface is needed between the general cubic elements in the interior and the gate surface. For prism elements, we simply let the local nodes 5, 9 and 1 overlap each other, i.e., local nodes 5, 9 and 1 has the same global coordinates. This also happens on nodes 7, 11 and 3, as well as nodes 15 and 13. In this way we can just treat prisms as the general cube elements; all the formula in the last section still hold. No extra work is needed.

4.3 Evaluation of integrals in the functional

With these preparations, we now evaluate each integral in the functional 4.1.8 explicitly. All the coordinates are local. Again the subscripts α are omitted for brevity.

4.3.1 Integrals on the lagoon side

For vertical gates, we use local polar coordinates with the origin at the center of the gate α. imaginary boundary C is chosen to be $r = r_C = \frac{B}{2}$ also centered at the origin

(Figure 3.2). Thus

$$\frac{\partial\tilde{\phi^+}}{\partial n} = \frac{\partial\tilde{\phi^+}}{\partial r} = \sum_{m=0}^{M}\sum_{n=0}^{N}\nu_{mn}\cos 2m\theta\frac{\cosh\left[k_n(z+h)\right]}{\cosh(k_n h)}\frac{H_{2m}^{(1)'}(k_n r)}{H_{2m}^{(1)}(k_n r_C)}k_n$$

The integral on C can be easily evaluated in the cylindrical coordinate system. They are given as follows.

1) I_1

For an element V^{el},

$$\int_{V^{el}}(\nabla\phi^+)^2 dV^{el} = \left\{\hat{\phi^+}\right\}^T\int_{V^{el}}\mathbf{B}^T\mathbf{B}dV^{el}\left\{\hat{\phi^+}\right\} = \left\{\hat{\phi^+}\right\}^T[K_1]^{el}\left\{\hat{\phi^+}\right\}$$

where $[K_1]^{el}$ is element stiffness matrix. For evaluating $[K_1]^{el}$ we turn to the isoparametric element from the physical element

$$\int_{V^{el}}\mathbf{B}^T\mathbf{B}dV^{el} = \int_{-1}^{+1}\int_{-1}^{+1}\int_{-1}^{+1}\mathbf{B}^T\mathbf{B}det(\mathbf{J})d\xi d\eta d\zeta$$

Then the standard Gaussian integration is applied.

After assemblage and redefining $\left\{\hat{\phi}^+\right\}$ as the global nodal potential vector, we get

$$I_1 = \frac{1}{2}\left\{\hat{\phi}^+\right\}^T[K_1]\left\{\hat{\phi}^+\right\}^*$$

2) I_2

For an element with one face on the free surface, say $\zeta = 1$,

$$\int_{S_F^{el}}-\frac{\omega^2}{g}\phi^{+2}dS_F^{el} = \left\{\hat{\phi}^+\right\}^T\int_{-1}^{+1}\int_{-1}^{+1}-\frac{\omega^2}{g}\left[\mathbf{H}^T\mathbf{H}det(\mathbf{J})\right]_{\zeta=1}d\xi d\eta\left\{\hat{\phi}^+\right\}$$

where $[K_2]^{el}$ is element stiffness matrix. For the surface integral, our 20-node isoparametric cubic elements will degenerate to 8-node isoparametric plane elements. In general, the Jacobian of transformation for 3D global face (x, y, z) to 2D local face (ξ, η) is

$$\begin{aligned} det(\mathbf{J}) &= \left|\frac{\partial\vec{X}(x,y,z)}{\partial\xi}\times\frac{\partial\vec{X}(x,y,z)}{\partial\eta}\right| \\ &= \left[\left(\frac{\partial x}{\partial\xi}\frac{\partial y}{\partial\eta}-\frac{\partial y}{\partial\xi}\frac{\partial x}{\partial\eta}\right)^2+\left(\frac{\partial y}{\partial\xi}\frac{\partial z}{\partial\eta}-\frac{\partial z}{\partial\xi}\frac{\partial y}{\partial\eta}\right)^2+\left(\frac{\partial z}{\partial\xi}\frac{\partial x}{\partial\eta}-\frac{\partial x}{\partial\xi}\frac{\partial z}{\partial\eta}\right)^2\right]^{\frac{1}{2}} \quad (4.3.12) \end{aligned}$$

The interpolation functions for the 2D element in Figure 4.3.1 are defined as follows:

$$h_i = \frac{1}{4}(1+\xi_i\xi)(1+\eta_i\eta)(\xi_i\xi+\eta_i\eta-1), \quad i = 1,3,5,7;$$

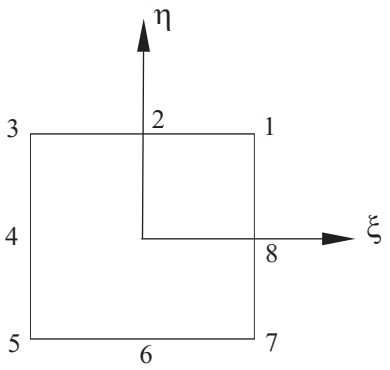

Figure 4.3: 8-node isoparametric plane element

$$h_i = \frac{1}{2}(1-\xi^2)(1+\eta_i\eta), \quad i = 2, 6;$$
$$h_i = \frac{1}{2}(1-\eta^2)(1+\xi_i\xi), \quad i = 4, 8;$$

where

$$\xi_i,\ \eta_i = \pm 1$$

Therefore,

$$h_{i,\xi} = \frac{1}{4}\xi_i(1+\eta_i\eta)(2\xi_i\xi+\eta_i\eta), \quad i = 1, 3, 5, 7;$$
$$h_{i,\xi} = \xi(1+\eta_i\eta), \quad i = 2, 6;$$
$$h_{i,\xi} = \frac{1}{2}\xi_i(1-\eta^2), \quad i = 4, 8;$$

and

$$h_{i,\eta} = \frac{1}{4}\eta_i(1+\xi_i\xi)(2\eta_i\eta+\xi_i\xi), \quad i = 1, 3, 5, 7;$$
$$h_{i,\eta} = \frac{1}{2}\eta_i(1-\xi^2), \quad i = 2, 6;$$
$$h_{i,\eta} = \eta(1+\xi_i\xi), \quad i = 4, 8;$$

After assemblage and using the global $\hat{\phi}$, we get

$$I_2 = \frac{1}{2}\left\{\hat{\phi}^+\right\}^T [K_2] \left\{\hat{\phi}^+\right\}$$

3) I_3

$$
\begin{aligned}
\int_C \tilde{\phi^+}\frac{\partial\tilde{\phi^+}}{\partial n}dS &= \int_{-h}^{0} dz \int_{-\frac{\pi}{2}}^{\frac{\pi}{2}} r_C d\theta \left\{ \sum_{p=0}^{M}\sum_{q=0}^{N} \nu_{pq}\cos 2p\theta \frac{\cosh\left[k_q(z+h)\right]}{\cosh(k_q h)} \frac{H_{2p}^{(1)}(k_q r_C)}{H_{2p}^{(1)}(k_q r_C)} \right\} \\
&\quad \left\{ \sum_{m=0}^{M}\sum_{n=0}^{N} \nu_{mn}\cos 2m\theta \frac{\cosh\left[k_n(z+h)\right]}{\cosh(k_n h)} \frac{H_{2m}^{(1)'}(k_n r_C)}{H_{2m}^{(1)}(k_n r_C)} k_n \right\} \\
&= \sum_{p=0}^{M}\sum_{q=0}^{N}\sum_{m=0}^{M}\sum_{n=0}^{N} \frac{r_C k_n \nu_{pq}\nu_{mn}}{\cosh(k_q h)\cosh(k_n h)} \frac{H_{2m}^{(1)'}(k_n r_C)}{H_{2m}^{(1)}(k_n r_C)} \\
&\quad \int_{-\frac{\pi}{2}}^{\frac{\pi}{2}} \cos 2p\theta \cos 2m\theta d\theta \int_{-h}^{0} \cosh\left[k_q(z+h)\right]\cosh\left[k_n(z+h)\right] dz \\
&= \sum_{m=0}^{M}\sum_{n=0}^{N} \nu_{mn}^2 \frac{\pi r_C k_n C_n}{\epsilon_m \cosh^2(k_n h)} \frac{H_{2m}^{(1)'}(k_n r_C)}{H_{2m}^{(1)}(k_n r_C)}
\end{aligned}
$$

where ϵ_m is the Jacobi symbol,

$$\epsilon_0 = 1, \quad \epsilon_m = 2,\ m = 1, 2, 3, \ldots \tag{4.3.13}$$

and C_n is defined by

$$C_n = \int_{-h}^{0} \cosh[k_n(z+h)]\cosh[k_n(z+h)]dz = \frac{1}{2k_n}(q_n + \frac{1}{2}\sinh 2q_n) \tag{4.3.14}$$

and $q_n = k_n h$. Use has been made of the orthogonality of the eigen functions. Derivatives of Hankel function are calculated by

$$H'_\nu = \frac{1}{2}(H_{\nu-1} - H_{\nu+1})$$

If we define an unknown column coefficient vector

$$\{\hat{\nu}\} = \Big[\ \nu_{00}\ \ \nu_{10}\ \ \cdots\ \ \nu_{M0}\vdots\ \ \nu_{01}\ \ \nu_{11}\ \ \cdots\ \ \nu_{M1}\vdots\ \ \cdots\vdots\ \ \nu_{0N}\ \ \nu_{1N}\ \ \cdots\ \ \nu_{MN}\ \Big]^T_{(M+1)\times(N+1)}$$

then the integral can be written in matrix form

$$\int_C \tilde{\phi^+}\frac{\partial\tilde{\phi^+}}{\partial n}dS = \{\hat{\nu}\}^T [K_3] \{\hat{\nu}\}$$

where K_3 is a diagonal and

$$[K_3]_{j,j} = \frac{\pi r_C k_n C_n}{\epsilon_m \cosh^2(k_n h)} \frac{H_{2m}^{(1)'}(k_n r_C)}{H_{2m}^{(1)}(k_n r_C)}$$

where

$$j = (M+1)\times n + m + 1$$

Therefore

$$I_3 = \frac{1}{2}\{\hat{\mu}\}^T [K_3] \{\hat{\mu}\}$$

4) I_4

With one face of the element on C, say $\eta = 1$,

$$\begin{aligned}\int_{C^{el}} \phi^+ \frac{\partial \tilde{\phi^+}}{\partial n} dC^{el} &= \int_{-1}^{+1}\int_{-1}^{+1} \left[\mathbf{H}\hat{\phi}\mathbf{M}\hat{\mu} det(\mathbf{J})\right]_{\eta=1} d\xi d\zeta \\ &= \left\{\hat{\phi^+}\right\}^T \int_{-1}^{+1}\int_{-1}^{+1} \left[\mathbf{H}^T\mathbf{M} det(\mathbf{J})\right]_{\eta=1} d\xi d\zeta \{\hat{\nu}\} \\ &= \left\{\hat{\phi}\right\}^T [K_4]^{el} \{\hat{\nu}\}\end{aligned}$$

where $[K_4]^{el}$ is element stiffness matrix and $\mathbf{M}$ is a row vector with

$$\mathbf{M}_{(M+1)\times n+m+1} = \cos\left[2m\cos^{-1}\left(\frac{x}{r_C}\right)\right] \frac{\cosh\left[k_n(z+h)\right]}{\cosh(k_n h)} \frac{H_{2m}^{(1)'}(k_n r_C)}{H_{2m}^{(1)}(k_n r_C)} k_n$$

Keep it in mind that the whole integrand will be evaluated at $\eta = 1$. The x and z are about to be replaced by (ξ, η, ζ) through (4.2.9) and $det(\mathbf{J})$ is obtained from (4.3.12) by replacing η with ζ. Therefore

$$I_4 = -\left\{\hat{\phi^+}\right\}^T [K_4] \{\hat{\nu}\}$$

5) I_5

For an element with one face at gate, say $\xi = 1$,

$$\int_{S_B^{el}} \mathcal{U}_n \phi dS_B^{el} = \int_{-1}^{+1}\int_{-1}^{+1} \left[\mathcal{U}_n \mathbf{H} det(\mathbf{J})\right]_{\xi=1} d\eta d\zeta \left\{\hat{\phi}^+\right\} = [K_5]^{el} \left\{\hat{\phi}^+\right\} \tag{4.3.15}$$

where $\mathcal{U}_n$ is to be defined later. $[K_5]^{el}$ is element stiffness matrix. After assemblage we get

$$I_5 = -[K_5] \left\{\hat{\phi^+}\right\}$$

4.3.2 Integrals on the sea side – the 3-D radiation problem

We now switch to the global coordinates and use (3.2.14) as the outer solution, which can be rewritten as

$$\tilde{\phi^-} = \sum_{m=0}^{\infty}\sum_{n=0}^{\infty} \mu_{mn} e^{-i\alpha_{mn}x} \cos\frac{m\pi y}{a} \frac{\cosh\left[k_n(z+h)\right]}{\cosh k_n h} \tag{4.3.16}$$

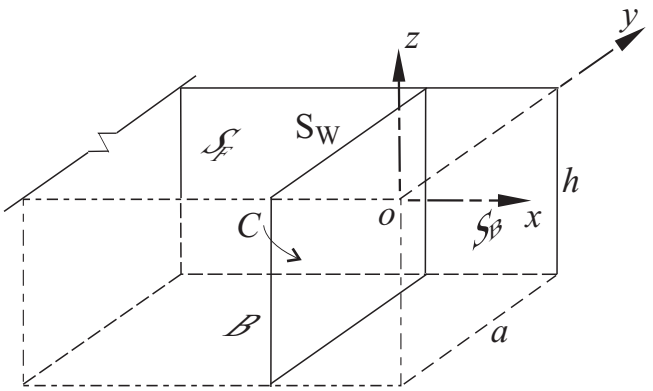

Figure 4.4: Sea side HFEM

with

$$A_{mn} = \frac{\mu_{mn}}{\cosh(k_n h)}$$

It is natural to choose a vertical rectangle C as the imaginary boundary (see Figure 4.3.2). Note that $x = x_C$ on this boundary and the normal is in the negative direction of the x axis. Therefore we have

$$\frac{\partial \tilde{\phi^-}}{\partial n} = -\frac{\partial \tilde{\phi^-}}{\partial x} = \sum_{m=0}^{M}\sum_{n=0}^{N} \mu_{mn} e^{-i\alpha_{mn}x} \cos\frac{m\pi y}{a} \frac{\cosh\left[k_n(z+h)\right]}{\cosh k_n h} i\alpha_{mn}$$

The integrals of I_1 and I_2 in (4.1.8) take the same form as those on the lagoon side. We need however to calculate I_3, I_4 and I_5.

1) I_3

$$\begin{aligned}
\int_C \tilde{\phi^-}\frac{\partial \tilde{\phi^-}}{\partial n} dS &= \int_{-h}^{0} dz \int_0^a dy \left\{ \sum_{p=0}^{M}\sum_{q=0}^{N} \mu_{pq} e^{-i\alpha_{pq}x_C} \cos\frac{p\pi y}{a} \frac{\cosh\left[k_q(z+h)\right]}{\cosh k_q h} \right\} \\
&\quad \left\{ \sum_{m=0}^{M}\sum_{n=0}^{N} \mu_{mn} e^{-i\alpha_{mn}x_C} \cos\frac{m\pi y}{a} \frac{\cosh\left[k_n(z+h)\right]}{\cosh k_n h} i\alpha_{mn} \right\} \\
&= \sum_{p=0}^{M}\sum_{q=0}^{N}\sum_{m=0}^{M}\sum_{n=0}^{N} \frac{i\alpha_{mn}\mu_{pq}\mu_{mn} e^{-i\alpha_{pq}x_C} e^{-i\alpha_{mn}x_C}}{\cosh(k_q h)\cosh(k_n h)} \\
&\quad \int_0^a \cos\frac{p\pi y}{a}\cos\frac{m\pi y}{a} dy \int_{-h}^{0} \cosh\left[k_q(z+h)\right]\cosh\left[k_n(z+h)\right] dz \\
&= \sum_{m=0}^{M}\sum_{n=0}^{N} \mu_{mn}^2 \frac{i\alpha_{mn} e^{-2i\alpha_{mn}x_C}}{\cosh^2(k_n h)} \frac{a}{\epsilon_m} C_n
\end{aligned}$$

where ϵ_m and C_n are defined in (4.3.13) and (4.3.14). Use has been made of the orthogonality of the eigen functions. Let us define an unknown column coefficient vector

$$\{\hat{\mu}\} = \Big[\begin{array}{cccc:cccc:c:cccc} \mu_{00} & \mu_{10} & \cdots & \mu_{M0} & \mu_{01} & \mu_{11} & \cdots & \mu_{M1} & \cdots & \mu_{0N} & \mu_{1N} & \cdots & \mu_{MN} \end{array} \Big]^T_{(M+1)\times(N+1)}$$

then the integral can be written in matrix form

$$\int_C \tilde{\phi^-} \frac{\partial \tilde{\phi^-}}{\partial n} dS = \{\hat{\mu}\}^T [K_3] \{\hat{\mu}\}$$

where K_3 is diagonal

$$[K_3]_{j,j} = \frac{i\alpha_{mn} e^{-2i\alpha_{mn} x_C}}{\cosh^2(k_n h)} \frac{a}{\epsilon_m} C_n$$

with

$$j = (M+1) \times n + m + 1$$

Therefore

$$I_3 = \frac{1}{2} \{\hat{\mu}\}^T [K_3] \{\hat{\mu}\}$$

2) I_4

With one face of the element on C, say $\eta = 1$,

$$\begin{aligned} \int_{C^{el}} \phi^- \frac{\partial \tilde{\phi^-}}{\partial n} dC^{el} &= \int_{-1}^{+1} \int_{-1}^{+1} \left[\mathbf{H} \hat{\phi} \mathbf{M} \hat{\mu} det(\mathbf{J}) \right]_{\eta=1} d\xi d\zeta \\ &= \left\{ \hat{\phi^-} \right\}^T \int_{-1}^{+1} \int_{-1}^{+1} \left[\mathbf{H}^T \mathbf{M} det(\mathbf{J}) \right]_{\eta=1} d\xi d\zeta \{\hat{\mu}\} \\ &= \left\{ \hat{\phi^-} \right\}^T [K_4]^{el} \{\hat{\mu}\} \end{aligned}$$

where $[K_4]^{el}$ is element stiffness matrix and $\mathbf{M}$ is a row vector with

$$\mathbf{M}_{(M+1)\times n+m+1} = e^{-i\alpha_{mn} x_C} \cos \frac{m\pi y}{a} \frac{\cosh\left[k_n(z+h)\right]}{\cosh k_n h} i\alpha_{mn}$$

The integrand is evaluated on $\eta = 1$. We switch from the global coordinates x and z to local coordinates (ξ, η, ζ) through the relation (4.2.9). The determinant $det(\mathbf{J})$ is obtained from (4.3.12) by replacing η with ζ. Therefore

$$I_4 = -\left\{ \hat{\phi^-} \right\}^T [K_4] \{\hat{\mu}\}$$

3) I_5

For an element with one face at gate, say $\xi = 1$,

$$\int_{S_B^{el}} \mathcal{U}_n \phi dS_B^{el} = \int_{-1}^{+1}\int_{-1}^{+1} \left[\mathcal{U}_n \mathbf{H} det(\mathbf{J})\right]_{\xi=1} d\eta d\zeta \left\{\hat{\phi^-}\right\} = [K_5]^{el} \left\{\hat{\phi^-}\right\}$$

where $\mathcal{U}_n$ is to be defined later. $[K_5]^{el}$ is element stiffness matrix. After assemblage we get

$$I_5 = -[K_5]\left\{\hat{\phi^-}\right\}$$

4.3.3 Minimization and solving linear system equations

On either side of the barrier, the functional is of the same form. For the sea side it reads

$$\begin{aligned}\mathcal{F}(\hat{\phi^-}, \hat{\mu}) &= \frac{1}{2}\left\{\hat{\phi^-}\right\}^T [K_1]\left\{\hat{\phi^-}\right\} + \frac{1}{2}\left\{\hat{\phi^-}\right\}^T [K_2]\left\{\hat{\phi^-}\right\} + \frac{1}{2}\hat{\mu}^T [K_3]\{\hat{\mu}\} \\ &\quad - \left\{\hat{\phi^-}\right\}^T [K_4]\{\hat{\mu}\} - [K_5]\left\{\hat{\phi^-}\right\} \end{aligned} \tag{4.3.17}$$

For the lagoon side, the stationary functional is

$$\begin{aligned}\mathcal{F}(\hat{\phi^+}, \hat{\nu}) &= \frac{1}{2}\left\{\hat{\phi^+}\right\}^T [K_1]\left\{\hat{\phi^+}\right\} + \frac{1}{2}\left\{\hat{\phi^+}\right\}^T [K_2]\left\{\hat{\phi^+}\right\} + \frac{1}{2}\hat{\nu}^T [K_3]\{\hat{\nu}\} \\ &\quad - \left\{\hat{\phi^+}\right\}^T [K_4]\{\hat{\nu}\} - [K_5]\left\{\hat{\phi^+}\right\} \end{aligned} \tag{4.3.18}$$

We take the generic form and equate to zero the first derivative with respect to unknowns ϕ_i and μ_i (or ν_i), and get,

$$[K_1]\left\{\hat{\phi}\right\} + [K_2]\left\{\hat{\phi}\right\} - [K_4]\{\hat{\mu}\} = [K_5]^T \tag{4.3.19}$$

$$[K_3]\{\hat{\mu}\} - [K_4]^T\left\{\hat{\phi}\right\} = 0 \tag{4.3.20}$$

From here on, we have two ways to solve the linear system of equations:

1. Method 1:

   Equation (4.4.40) gives

   $$\{\hat{\mu}\} = [K_3]^{-1}[K_4]^T\left\{\hat{\phi}\right\} \tag{4.3.21}$$

   Substituting it into (4.4.39), we get

   $$\left\{[K_1] + [K_2] - [K_4][K_3]^{-1}[K_4]^T\right\}\left\{\hat{\phi}\right\} = [K_5]^T$$

   and $\left\{\hat{\phi}\right\}$ is obtained. Substituting $\left\{\hat{\phi}\right\}$ back into (4.4.41) to get $\{\hat{\mu}\}$.

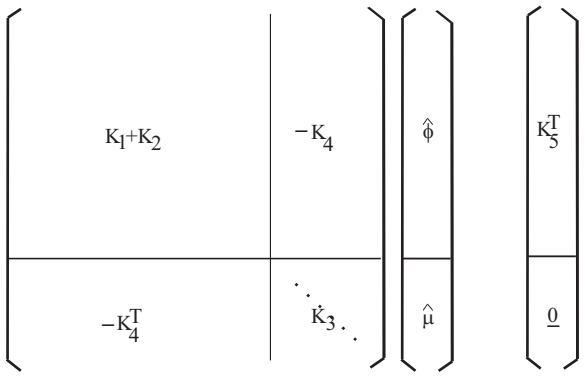

Figure 4.5: The linear system of equations after assemblage

2. Method 2:

   Assemble all the matrix on the LHS into one matrix as well as the RHS. See Figure 4.5 for detail. Then we can solve the new linear system equations to get both $\left\{\hat{\phi}\right\}$ and $\{\hat{\mu}\}$ (or $\{\hat{\nu}\}$) simultaneously.

Then the velocity potential is known in both the finite element domain and the super element, i.e., the fluid region outside the imaginary boundary C. As the computation scale increases, we try to take the advantage of sparse matrix and use the external linear system equations solver to save memory and CPU time. The second method is adopted so that we need solve the equations only once, instead of manipulations of several matrix as in the first method.

4.4 2-D diffraction on the sea side

In the diffraction problem, the gates are stationary (see Figure 4.6). For normally incident, long-crested waves, the dynamics of water is two dimensional. For vertical gates the reflected wave is trivial; for inclined gates the reflected waves must be found numerically. Details are given here for the sake of completeness.

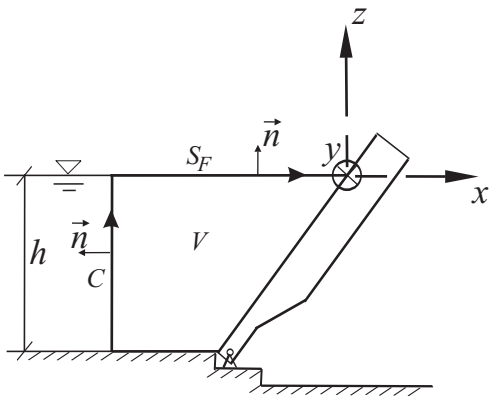

Figure 4.6: Schematic plan for diffraction problem

4.4.1 Variational principle

We let the known incident wave Φ^I be

$$\Phi^I = \varphi^I e^{-i\omega t} = \frac{-igA}{\omega}\frac{\cosh\left[k_0(z+h)\right]}{\cosh(k_0 h)}e^{ik_0 x}e^{-i\omega t} \tag{4.4.22}$$

where A is the incident wave amplitude, and the unknown reflected wave potential in the near field be

$$\Phi^R = \varphi^R e^{-i\omega t} \tag{4.4.23}$$

The total diffraction potential $\varphi^D(x,z) = \varphi^I + \varphi^R$ satisfies the conditions $(2.2 \sim 2.4)$. The reflected wave must satisfy the radiation condition. Similar to §3.1.2, it can be proven that diffraction boundary-value problem is equivalent to the stationarity of the following functional

$$\mathcal{F}(\varphi^D, \tilde{\varphi}^R) = \int_V \frac{1}{2}(\nabla\varphi^D)^2 dV - \int_{S_F}\frac{\omega^2}{2g}\left(\varphi^D\right)^2 dS + \int_C [(\frac{\tilde{\varphi}^R}{2} - \varphi^R)\frac{\partial\tilde{\varphi}}{\partial n} - \frac{\tilde{\varphi}^R}{2}\frac{\partial\varphi^I}{\partial n}]dS \tag{4.4.24}$$

where $\varphi = \varphi^R + \varphi^I$ is the total potential within the finite element domain and $\tilde{\varphi} = \tilde{\varphi}^R + \varphi^I$ is the total potential of the outer domain; $\tilde{\varphi}^R$ is the reduced 2D solution from the eigen function expansion (3.2.14), i.e.

$$\tilde{\varphi}^R = \sum_{n=0}^{\infty}\mu_n e^{-ik_n x}\frac{\cosh\left[k_n(z+h)\right]}{\cosh k_n h} \tag{4.4.25}$$

where k_0 is the real root and $k_n{}'s$ with $n = 1, 2, 3, ...$ are the imaginary roots of the dispersion relation (3.2.9).

Note that

$$\int_C \varphi^I \frac{\partial \varphi^I}{\partial n} dS$$

is a constant and drops out upon extremization, (4.4.24) can be rewritten as

$$\begin{aligned}\mathcal{F} \;=\; & \overbrace{\int_V \frac{1}{2}(\nabla\varphi^D)^2 dV}^{I_1} + \overbrace{\int_{S_F} -\frac{\omega^2}{2g}\left(\varphi^D\right)^2 dS}^{I_2} + \overbrace{\int_C \frac{\tilde{\varphi}^R}{2}\frac{\partial\tilde{\varphi}^R}{\partial n} dS}^{I_3} + \overbrace{\int_C -\varphi^D \frac{\partial\tilde{\varphi}^R}{\partial n} dS}^{I_4} \\ & + \overbrace{\int_C \varphi^I \frac{\partial\tilde{\varphi}^R}{\partial n} dS}^{I_5} + \overbrace{\int_C -\varphi^D \frac{\partial\varphi^I}{\partial n} dS}^{I_6} \end{aligned} \tag{4.4.26}$$

4.4.2 2-D Finite element formulation

In the finite element region, standard 3-node elements with piece-wise linear potentials are defined within each element:

$$\varphi^D = \sum_{i=1}^{3} \varphi_i N_i(x,z) \tag{4.4.27}$$

where φ_i is an unknown nodal potential and $N_i(x,z)$ is a interpolation function

$$N_i = (a_i + b_i x + c_i z)/2\triangle \tag{4.4.28}$$

$i = 1, 2, 3$, with

$$\begin{cases} a_1 = x_2^e z_3^e - x_3^e z_2^e \\ b_1 = z_2^e - z_3^e \\ c_1 = x_3^e - x_2^e \end{cases} \quad \begin{cases} a_2 = x_3^e z_1^e - x_1^e z_3^e \\ b_2 = z_3^e - z_1^e \\ c_2 = x_1^e - x_3^e \end{cases} \quad \begin{cases} a_3 = x_1^e z_2^e - x_2^e z_1^e \\ b_3 = z_1^e - z_2^e \\ c_3 = x_2^e - x_1^e \end{cases}$$

$\triangle$ is the area of the triangle element,

$$\triangle = \frac{a_1 + a_2 + a_3}{2}$$

Note that the nodal numbering sequence must be counter-clock-wise (see Figure 5.1) to ensure that the area of the triangle is positive.

In matrix form,

$$\varphi^D = \begin{bmatrix} N_1 & N_2 & N_3 \end{bmatrix} \begin{bmatrix} \varphi_1 \\ \varphi_2 \\ \varphi_3 \end{bmatrix} = \mathbf{N}\{\hat{\varphi}\} \tag{4.4.29}$$

therefore,

$$(\nabla\varphi^D)^2 = (\frac{\partial\varphi^D}{\partial x})^2 + (\frac{\partial\varphi^D}{\partial z})^2 = \begin{bmatrix} \frac{\partial\varphi}{\partial x} & \frac{\partial\varphi}{\partial z} \end{bmatrix} \begin{bmatrix} \frac{\partial\varphi}{\partial x} \\ \frac{\partial\varphi}{\partial z} \end{bmatrix} \tag{4.4.30}$$

Let us define

$$\begin{bmatrix} \frac{\partial\varphi^D}{\partial x} \\ \frac{\partial\varphi^D}{\partial z} \end{bmatrix} = \begin{bmatrix} \frac{\partial N_1}{\partial x} & \frac{\partial N_2}{\partial x} & \frac{\partial N_3}{\partial x} \\ \frac{\partial N_1}{\partial z} & \frac{\partial N_2}{\partial z} & \frac{\partial N_3}{\partial z} \end{bmatrix} \begin{bmatrix} \varphi_1 \\ \varphi_2 \\ \varphi_3 \end{bmatrix} = \mathbf{B}\hat{\varphi}$$

From 4.4.27 we can calculate $\mathbf{B}$ to obtain

$$\mathbf{B} = \frac{1}{2\triangle} \begin{bmatrix} b_1 & b_2 & b_3 \\ c_1 & c_2 & c_3 \end{bmatrix}$$

On the imaginary boundary $x = x_C$,

$$\frac{\partial\tilde{\varphi}^R}{\partial n} = -\frac{\partial\tilde{\varphi}^R}{\partial x} = \sum_{n=0}^{\infty} \mu_n i k_n e^{-ik_n x_C} \frac{\cosh\left[k_n(z+h)\right]}{\cosh k_n h} \tag{4.4.31}$$

and

$$\frac{\partial\varphi^I}{\partial n} = -\frac{\partial\varphi^I}{\partial x} = \frac{-gAk_0}{\omega} e^{ik_0 x_C} \frac{\cosh\left[k_0(z+h)\right]}{\cosh(k_0 h)} \tag{4.4.32}$$

Next, we evaluate the integrals one by one.

1) I_1

For an element V^{el},

$$\int_{V^{el}} (\nabla\varphi^D)^2 dV^{el} = \{\hat{\varphi}\}^T \int_{V^{el}} \mathbf{B}^T\mathbf{B} dV^{el} \{\hat{\varphi}\} = \{\hat{\varphi}\}^T [K_1]^{el} \{\hat{\varphi}\}$$

where $[K_1]^{el}$ is the element stiffness matrix

$$[K_1]_{ij}^{el} = \frac{b_i b_j + c_i c_j}{4\triangle}$$

After assemblage and redefining $\left\{\hat{\varphi^D}\right\}$ as the global nodal potential vector, we get

$$I_1 = \frac{1}{2} \left\{\hat{\varphi^D}\right\}^T [K_1] \left\{\hat{\varphi^D}\right\}$$

2) I_2

We employ two-node linear truss element and carry out the integrations under the local coordinate system. When mapping from global nodes to local nodes, we must ensure the boundary normal points towards the right-hand side when viewing into the

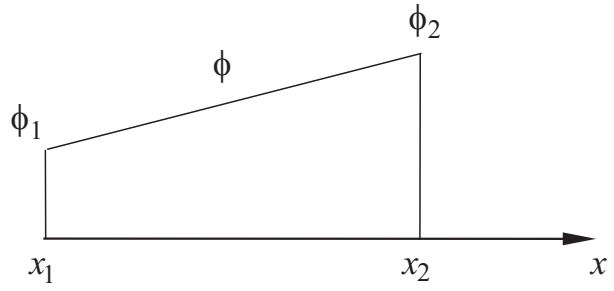

Figure 4.7: Local coordinate system for truss element

y-axis as we go from x_1 to x_2. In our example, we should integrate from node 2 to node 1 in Figure 4.7.

$$\varphi = \varphi_1 + \frac{x - x_1}{x_2 - x_1}(\varphi_2 - \varphi_1) = \frac{x_2 - x}{x_2 - x_1}\varphi_1 + \frac{x - x_1}{x_2 - x_1}\varphi_2 = h_1\varphi_1 + h_2\varphi_2$$

In matrix form,

$$\{\varphi\} = \begin{bmatrix} h_1 & h_2 \end{bmatrix} \begin{bmatrix} \varphi_1 \\ \varphi_2 \end{bmatrix} = \mathbf{H}\{\hat{\varphi}\} \tag{4.4.33}$$

For an element with one face on the free surface, say $z = 0$,

$$\int_{S_F^{el}} -\frac{\omega^2}{g}\varphi^{D^2} dS_F^{el} = \{\hat{\varphi}\}^T \int_{x_1}^{x_2} -\frac{\omega^2}{g}\mathbf{H}^T\mathbf{H}dx \;\; \{\hat{\varphi}\} = \{\hat{\varphi}\}^T [K_2]^{el} \{\hat{\varphi}\}$$

where $[K_2]^{el}$ is the element stiffness matrix. In the local coordinate system,

$$[K_2]^{el} = -\frac{\omega^2}{g} \begin{bmatrix} \frac{1}{3} & \frac{1}{6} \\ \frac{1}{6} & \frac{1}{3} \end{bmatrix} (x_2 - x_1)$$

After assemblage and using the global $\hat{\varphi}$, we can get

$$I_2 = \frac{1}{2}\left\{\hat{\varphi^D}\right\}^T [K_2] \left\{\hat{\varphi^D}\right\}$$

3) I_3

We integrate from $-h$ to 0 on the imaginary boundary $x = x_C$ so that the right-hand rule is obeyed.

$$\begin{aligned}
\int_C \tilde{\varphi}^R \frac{\partial \tilde{\varphi}^R}{\partial n} dS &= \int_{-h}^{0} dz \sum_{m=0}^{N} \mu_m e^{-ik_m x_C} \frac{\cosh[k_m(z+h)]}{\cosh k_m h} \sum_{n=0}^{N} \mu_n i k_n e^{-ik_n x_C} \frac{\cosh[k_n(z+h)]}{\cosh k_n h} \\
&= \sum_{m=0}^{N}\sum_{n=0}^{N} \frac{ik_n\mu_m\mu_n e^{-ik_m x_C} e^{-ik_n x_C}}{\cosh(k_m h)\cosh(k_n h)} \int_{-h}^{0} \cosh[k_m(z+h)]\cosh[k_n(z+h)]\, dz \\
&= \sum_{n=0}^{N} \frac{ik_n C_n \mu_n^2 e^{-2ik_n x_C}}{\cosh^2(k_n h)}
\end{aligned}$$

where use has been made of the orthogonality of the eigen functions and

$$C_n = \int_{-h}^{0} \cosh\left[k_n(z+h)\right] \cosh\left[k_n(z+h)\right] dz = \frac{1}{2k_n}(q_n + \frac{1}{2}\sinh 2q_n) \tag{4.4.34}$$

with $q_n = k_n h$. If we define an unknown column coefficient vector

$$\{\hat{\mu}\} = \left[\begin{array}{cccc} \mu_0 & \mu_1 & \cdots & \mu_N \end{array} \right]^T$$

then the integral can be written in matrix form

$$\int_C \tilde{\varphi}^R \frac{\partial \tilde{\varphi}^R}{\partial n} dS = \{\hat{\mu}\}^T [K_3] \{\hat{\mu}\}$$

where K_3 is a diagonal and

$$[K_3]_{j,j} = \frac{ik_n C_n e^{-2ik_n x_C}}{\cosh^2(k_n h)}$$

where

$$j = n + 1$$

Therefore

$$I_3 = \frac{1}{2} \{\hat{\mu}\}^T [K_3] \{\hat{\mu}\}$$

4) I_4

We still use local coordinate system as in 2) but replace x with z. Therefore,

$$\mathbf{H} = \left[\begin{array}{cc} h_1 & h_2 \end{array} \right] = \left[\begin{array}{cc} \frac{z_2 - z}{z_2 - z_1} & \frac{z - z_1}{z_2 - z_1} \end{array} \right] \tag{4.4.35}$$

Keep it in mind that the mirror from global nodes to local ones must be correct.

$$\begin{aligned} & \int_{C^{el}} \varphi^D \frac{\partial \tilde{\varphi}^R}{\partial n} dC^{el} \\ = & \int_{z_1}^{z_2} dz \mathbf{H} \{\hat{\varphi}\} \sum_{n=0}^{N} \mu_n i k_n e^{-ik_n x_C} \frac{\cosh\left[k_n(z+h)\right]}{\cosh k_n h} \\ = & \{\hat{\varphi}\}^T \int_{z_1}^{z_2} dz \mathbf{H}^T \mathbf{M} \{\hat{\mu}\} \\ = & \{\hat{\varphi}\}^T [K_4]^{el} \{\hat{\mu}\} \end{aligned}$$

where $[K_4]^{el}$ is element stiffness matrix and $\mathbf{M}$ is a row vector with

$$\mathbf{M}_{n+1} = ik_n e^{-ik_n x_C} \frac{\cosh\left[k_n(z+h)\right]}{\cosh k_n h}$$

Therefore

$$
\begin{aligned}
&[K_4]^{el}_{1,n+1} \\
&= \int_{z_1}^{z_2} dz\ h_1 i k_n e^{-ik_n x_C} \frac{\cosh\left[k_n(z+h)\right]}{\cosh k_n h} \\
&= \frac{i e^{-ik_n x_C}}{\cosh k_n h} \left\{ \frac{1}{k_n(z_2-z_1)} \left\{ \cosh\left[k_n(z_2+h)\right] - \cosh\left[k_n(z_1+h)\right] \right\} - \sinh\left[k_n(z_1+h)\right] \right\}
\end{aligned}
$$

$$
\begin{aligned}
&[K_4]^{el}_{2,n+1} \\
&= \int_{z_1}^{z_2} dz\ h_2 i k_n e^{-ik_n x_C} \frac{\cosh\left[k_n(z+h)\right]}{\cosh k_n h} \\
&= \frac{i e^{-ik_n x_C}}{\cosh k_n h} \left\{ \sinh\left[k_n(z_2+h)\right] - \frac{1}{k_n(z_2-z_1)} \left\{ \cosh\left[k_n(z_2+h)\right] - \cosh\left[k_n(z_1+h)\right] \right\} \right\}
\end{aligned}
$$

After assemblage, we get

$$
I_4 = -\left\{\hat{\varphi^D}\right\}^T [K_4] \{\hat{\mu}\}
$$

5) I_5

Integrate from $-h$ to 0, we get

$$
\begin{aligned}
\int_C \varphi^I \frac{\partial \tilde{\varphi}^R}{\partial n} dS &= \int_{-h}^{0} dz \frac{-igA}{\omega} \frac{\cosh\left[k_0(z+h)\right]}{\cosh(k_0 h)} e^{ik_0 x_C} \sum_{n=0}^{N} \mu_n i k_n e^{-ik_n x_C} \frac{\cosh\left[k_n(z+h)\right]}{\cosh k_n h} \\
&= \frac{-igAik_0}{\omega} \frac{C_0 \mu_0}{\cosh^2(k_0 h)} e^{ik_0 x_C} e^{-ik_0 x_C}
\end{aligned}
\tag{4.4.36}
$$

where C_0 is defined in (5.3.7). Use has been made of the orthogonality of the eigen functions in z. Therefore

$$
I_5 = [K_5] \{\hat{\mu}\}
$$

where $[K_5]$ is a row vector with the first component being non-zero

$$
[K_5]_1 = \frac{gAk_0 C_0}{\omega \cosh^2(k_0 h)}
$$

6) I_6

We use the same local coordinate system as in 4), i.e.

$$
\mathbf{H} = \begin{bmatrix} h_1 & h_2 \end{bmatrix} = \begin{bmatrix} \frac{z_2 - z}{z_2 - z_1} & \frac{z - z_1}{z_2 - z_1} \end{bmatrix} \tag{4.4.37}
$$

Therefore,

$$\begin{aligned}\int_{C^{el}} \varphi^D \frac{\partial \varphi^I}{\partial n} dC^{el} &= \int_{z_1}^{z_2} dz \mathbf{H} \{\hat{\varphi}\} \frac{-gAk_0}{\omega} e^{ik_0 x_C} \frac{\cosh[k_0(z+h)]}{\cosh(k_0 h)} \\ &= \hat{\varphi}^T \int_{z_1}^{z_2} dz \mathbf{H}^T \frac{-gAk_0}{\omega} \frac{\cosh[k_0(z+h)]}{\cosh(k_0 h)} e^{ik_0 x_C} \\ &= \{\hat{\varphi}\}^T [K_6]^{el}\end{aligned}$$

where $[K_6]^{el}$ is element stiffness matrix and note that we must mirror in the correct way. It follows that

$$\begin{aligned}&[K_6]_1^{el} \\ &= \int_{z_1}^{z_2} dz \; h_1 \frac{-gAk_0}{\omega} \frac{\cosh[k_0(z+h)]}{\cosh(k_0 h)} e^{ik_0 x_C} \\ &= \frac{-gAe^{ik_0 x_C}}{\omega \cosh k_0 h} \left\{ \frac{1}{k_0(z_2 - z_1)} \{\cosh[k_0(z_2+h)] - \cosh[k_0(z_1+h)]\} - \sinh[k_0(z_1+h)] \right\}\end{aligned}$$

$$\begin{aligned}&[K_6]_2^{el} \\ &= \int_{z_1}^{z_2} dz \; h_2 \frac{-gAk_0}{\omega} \frac{\cosh[k_0(z+h)]}{\cosh(k_0 h)} e^{ik_0 x_C} \\ &= \frac{-gAe^{ik_0 x_C}}{\omega \cosh k_0 h} \left\{ \sinh[k_0(z_2+h)] - \frac{1}{k_0(z_2 - z_1)} \{\cosh[k_0(z_2+h)] - \cosh[k_0(z_1+h)]\} \right\}\end{aligned}$$

After assemblage,

$$I_6 = -\left\{\hat{\varphi^D}\right\}^T [K_6]$$

and $[K_6]$ is a column vector.

In summary, the stationary functional for the reflected plane waves is

$$\begin{aligned}\mathcal{F}(\left\{\hat{\varphi^D}\right\}, \hat{\mu}) &= \frac{1}{2}\left\{\hat{\varphi^D}\right\}^T [K_1] \left\{\hat{\varphi^D}\right\} + \frac{1}{2}\left\{\hat{\varphi^D}\right\}^T [K_2] \left\{\hat{\varphi^D}\right\} + \frac{1}{2}\{\hat{\mu}\}^T [K_3] \{\hat{\mu}\} \\ &\quad - \left\{\hat{\varphi^D}\right\}^T [K_4] \{\hat{\mu}\} + [K_5] \{\hat{\mu}\} - \left\{\hat{\varphi^D}\right\}^T [K_6] \qquad (4.4.38)\end{aligned}$$

By Rayleigh-Ritz principle the first derivative with respect to unknowns φ_i and μ_i vanishes. Therefore

$$[K_1]\left\{\hat{\varphi^D}\right\} + [K_2]\left\{\hat{\varphi^D}\right\} - [K_4]\{\hat{\mu}\} = [K_6] \qquad (4.4.39)$$

$$[K_3]\{\hat{\mu}\} - [K_4]^T \left\{\hat{\varphi^D}\right\} = -[K_5]^T \qquad (4.4.40)$$

Equation (4.4.40) gives

$$\{\hat{\mu}\} = [K_3]^{-1} \left([K_4]^T \left\{ \hat{\varphi^D} \right\} - [K_5]^T \right) \tag{4.4.41}$$

When it is substituted into (4.4.39), we get

$$\left\{ [K_1] + [K_2] - [K_4] [K_3]^{-1} [K_4]^T \right\} \left\{ \hat{\varphi^D} \right\} = [K_6] - [K_4] [K_3]^{-1} [K_5]^T \tag{4.4.42}$$

Thus $\left\{ \hat{\varphi^D} \right\}$ is obtained. Replacing $\left\{ \hat{\varphi^D} \right\}$ into (4.4.41) we get $\{\hat{\mu}\}$. Afterwards the reflected wave potential is known in both the finite element and the super element.

4.5 Gate dynamics

With the radiation potentials known for unit displacement amplitudes, we can calculate the hydrodynamic forces on the gate. From the dynamical equations of gates, the angular displacements can then be found. These matters are discussed in the following chapters.

Chapter 5

Validation for vertical gates

For demonstration and validation of our 2- and 3-D numerical schemes, we consider first a barrier made of vertical gates. As reported by Adamo and Mei(2003), the radiation problem on the sea side can be solved analytically by eigenfunction expansions. On the lagoon side analytical solution can be solved by using Green's function. These results provide benchmarks for checking the correctness and accuracy of the numerical computations by scheme of HFEM. Due to the simple geometry, application of the hybrid element scheme is also relatively simple. On the lagoon side, it is only necessary to choose C large enough to enclose one gate.

5.1 2- D diffraction

We first use the standing-wave solution near a vertical wall as a check for the 2-D numerical solution. The analytical solution for the diffraction potential (incident and reflected wave potentials) in front of the wall is

$$\varphi^D = \frac{-2igA}{\omega} \frac{\cosh\left[k_0(z+h)\right]}{\cosh(k_0 h)} \cos(k_0 x) \tag{5.1.1}$$

To compare with the analytical solution, we develop the hybrid-finite-element scheme with the element mesh shown in Figure 5.1.

The numerical results are compared with the analytical solution (5.1.1) in Table 5.1 for the velocity potential on the first 20 nodes of our mesh. The agreement is excellent.

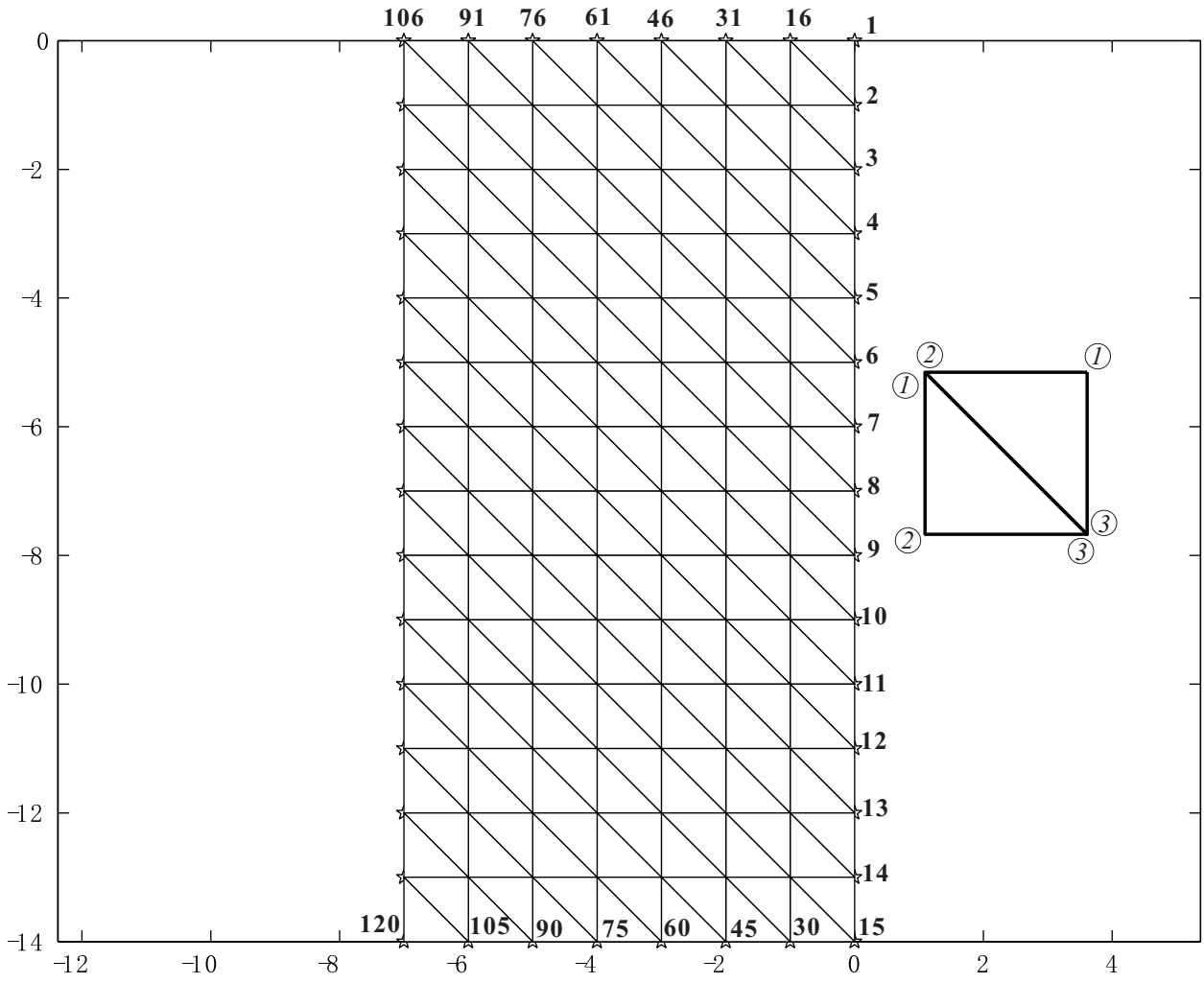

Figure 5.1: 2-D Finite element mesh for the diffraction problem

5.2 Dynamics of individual gates

We must now solve the radiation problems due to the motion of gates.

Consider a typical gates of width of B executing rotational oscillations with angular displacement

$$\Theta(t) = \vartheta e^{-i\omega t} \tag{5.2.2}$$

Conservation of angular momentum gives

$$I\Theta_{tt} + C\Theta = -\rho \iint_{S_B^{(0)}} \left(\Phi_t^D + \Phi_t^- - \Phi_t^+\right)(z+h)dS \tag{5.2.3}$$

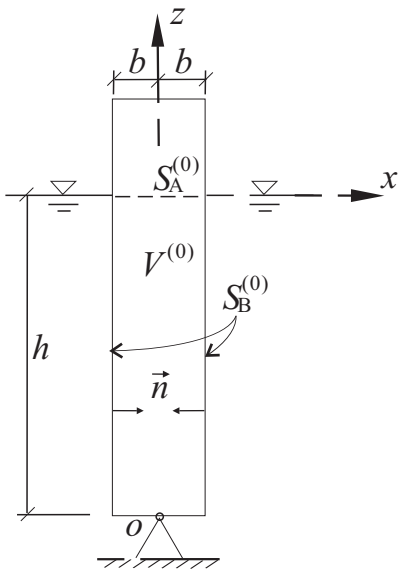

Figure 5.2: Coordinate system on the gate

where $\Phi^{\pm}$ is the spatial factors of the total potential on one side of the gate, I is the mass moment of inertia about the bottom hinge at O (see Figure 5.2)

$$I = \iiint_V \rho(x^2 + (z+h)^2)dV; \tag{5.2.4}$$

and C is the total restoring torque due to buoyancy and weight of the gate

$$C = \rho g(I_{xx}^A + I_z^V) - Mg(\bar{z}^c - Z^{(0)}) \tag{5.2.5}$$

with

$$I_{xx}^A = \iint_{S_A^{(0)}} (x - X^{(0)})^2 dx, \quad I_z^V = \iiint_{V^{(0)}} (z - Z^{(0)}) dxdz$$

For the vertical gate of rectangular cross section hinged on the bottom,

$$C = \rho g \frac{B}{2}\left[h^2 + \frac{2}{3}\left(\frac{B}{2}\right)^2\right] - Mg(\bar{z}^c + h) \tag{5.2.6}$$

where B is the width of the gate.

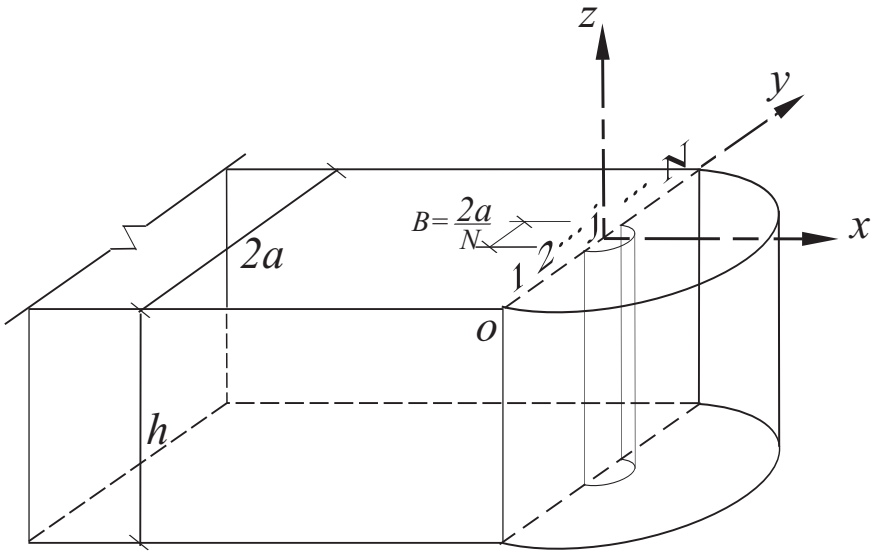

Figure 5.3: Schematic geometry for N vertical gates

5.3 Radiation problems and hydrodynamic torques

5.3.1 Sea side

For vertical gates let us first get the analytical solution.

In the global coordinate system, we denote by $\vec{L}$ the horizontal displacement of the gate,

$$\vec{L} = (z+h)\vartheta(y)e^{-i\omega t}\hat{x} \tag{5.3.1}$$

where $\hat{x}$ is the unit vector in the x direction. In this definition counter-clockwise rotation is positive when viewed from $y \sim \infty$, i.e., towards the $x-z$ plane along the negative direction of y. Therefore $\vartheta > 0$ as the gate inclines towards the lagoon. Matching the normal velocities of the gate and of the adjacent fluid, we get

$$\frac{\partial \Phi^-}{\partial x} = -i\omega(z+h)\vartheta(y)e^{-i\omega t} \quad \text{at} \quad x = 0 \tag{5.3.2}$$

After substituting (3.2.14) into (5.3.2) we get

$$\sum_{m=0}^{\infty}\sum_{n=0}^{\infty} A_{mn}\alpha_{mn}\cos\frac{m\pi y}{a}\cosh\left[k_n(z+h)\right] = \omega(z+h)\vartheta(y) \tag{5.3.3}$$

By orthogonality we can derive the expression for A_{mn}

$$A_{mn} = \omega\frac{b_m D_n}{C_n\alpha_{mn}} \tag{5.3.4}$$

where

$$b_m = \frac{\epsilon_m}{2a}\int_{-a}^{a}\vartheta(y)\cos(\frac{m\pi y}{a})dy \tag{5.3.5}$$

with

$$\epsilon_0 = 1, \quad \epsilon_m = 2,\ m = 1, 2, 3, \ldots \tag{5.3.6}$$

being the Jacobi symbol,

$$C_n = \int_{-h}^{0}\cosh[k_n(z+h)]\cosh[k_n(z+h)]dz = \frac{1}{2k_n}(q_n + \frac{1}{2}\sinh 2q_n) \tag{5.3.7}$$

$$D_n = \int_{-h}^{0}(z+h)\cosh[k_n(z+h)]dz = \frac{1}{k_n^2}(q_n\sinh q_n - \cosh q_n + 1) \tag{5.3.8}$$

and $q_n = k_n h$.

Finally the radiation potential on the sea side is

$$\varphi^- = \omega\sum_{m=0}^{\infty} b_m\cos\frac{m\pi y}{a}\sum_{n=0}^{\infty}\frac{D_n}{C_n\alpha_{mn}}e^{-i\alpha_{mn}x}\cosh\left[k_n(z+h)\right] \tag{5.3.9}$$

With N gates across the channel, we use different numbers to distinguish the gates, counting from center to the bank as shown in Figure 5.3. A vector can be defined to describe the unknown amplitude of the N gates

$$\hat{\vartheta} = \left[\begin{array}{ccccccc} \theta_1 & \vartheta_2 & \cdots & \vartheta_j & \cdots & \vartheta_N \end{array}\right]^T \tag{5.3.10}$$

where ϑ_j represents the angular displacement amplitude of the jth gate. Therefore on the sea side, $\vartheta(y)$ in (5.3.1) becomes

$$\vartheta(y) = \begin{cases} \vartheta_1\,, & y \in Y_1 = (-a,\, -a+B) \\ \vartheta_2\,, & y \in Y_2 = (-a+B,\, -a+2B) \\ \vdots & \\ \vartheta_j\,, & y \in Y_j = (-a+(j-1)B,\, -a+jB) \\ \vdots & \\ \vartheta_N\,, & y \in Y_N = (-a+(N-1)B,\, a) \end{cases} \tag{5.3.11}$$

where $B = \frac{2a}{N}$ is the width of one gate. Substituting this into (5.3.5), we get

$$b_m = \frac{\epsilon_m}{2a}\left[\int_{-a}^{-a+B}\vartheta_1\cos(\frac{m\pi y}{a})dy + \int_{-a+B}^{-a+2B}\vartheta_2\cos(\frac{m\pi y}{a})dy + \cdots + \int_{-a+(N-1)B}^{a}\vartheta_N\cos(\frac{m\pi y}{a})dy\right]$$

It follows that

$$b_0 = \frac{1}{2a}\frac{2a}{N}(\vartheta_1 + \vartheta_2 + \cdots + \vartheta_N) = \frac{1}{N}(\vartheta_1 + \vartheta_2 + \cdots + \vartheta_N)$$

and

$$\begin{aligned} b_m &= \frac{\vartheta_1}{m\pi}\sin(\frac{(2-N)m\pi}{N}) + \frac{\vartheta_2}{m\pi}\left[\sin(\frac{(4-N)m\pi}{N}) - \sin(\frac{(2-N)m\pi}{N})\right] + \cdots \\ &\quad + \frac{\vartheta_j}{m\pi}\left[\sin(\frac{(2j-N)m\pi}{N}) - \sin(\frac{(2(j-1)-N)m\pi}{N})\right] + \cdots - \frac{\vartheta_N}{m\pi}\sin(\frac{(N-2)m\pi}{N}) \end{aligned}$$

for $m \neq 0$.

From (5.3.9), the potential Φ^- can be written as

$$\Phi^- = (\vartheta_1\phi_1^- + \vartheta_2\phi_2^- + \cdots + \vartheta_j\phi_j^- + \cdots + \vartheta_N\phi_N^-)e^{-i\omega t} \tag{5.3.12}$$

where

$$\begin{aligned} \phi_j^- &= \omega\left\{\frac{1}{N}\sum_{n=0}^{\infty}\frac{D_n}{C_n k_n}e^{-ik_n x}\cosh\left[k_n(z+h)\right]\right. \\ &+ \sum_{m=1}^{\infty}\frac{1}{m\pi}\left[\sin(\frac{(2j-N)m\pi}{N}) - \sin(\frac{(2(j-1)-N)m\pi}{N})\right]\cos\frac{m\pi y}{a} \\ &\left.\sum_{n=0}^{\infty}\frac{D_n}{C_n\alpha_{mn}}e^{-i\alpha_{mn}x}\cosh\left[k_n(z+h)\right]\right\} \end{aligned}$$

is the radiation potential due to the motion of the jth gate, when all others are stationary. In order to express the right-hand side of (5.2.3) more explicitly, we define the excitation on pth gate due to the unit amplitude motion of the jth gate,

$$F_{pj}^- = i\omega\rho\int_{S_B^p} dy\int_{-h}^{0}\left[\phi_j^-\right]_{x=0}(z+h)dz \tag{5.3.13}$$

Therefore

$$\begin{aligned} F_{pj}^- &= i\rho\omega^2 a\left\{\frac{2}{N^2}\sum_{n=0}^{\infty}\frac{D_n^2}{C_n k_n}\right. \\ &+ \sum_{m=1}^{\infty}\frac{1}{m^2\pi^2}\left[\sin(\frac{(2j-N)m\pi}{N}) - \sin(\frac{(2(j-1)-N)m\pi}{N})\right] \\ &\left.\left[\sin(\frac{(2p-N)m\pi}{N}) - \sin(\frac{(2(p-1)-N)m\pi}{N})\right]\sum_{n=0}^{\infty}\frac{D_n^2}{C_n\alpha_{mn}}\right\} \end{aligned}$$

It is easy to see that $F_{pj}^- = F_{jp}^-$.

Since the diffraction potential (sum of incident and reflected wave potentials) on the sea side is

$$\Phi^D = \frac{-igA}{\omega}\frac{\cosh\left[k_0(z+h)\right]}{\cosh(k_0h)}(e^{-ik_0x}+e^{ik_0x})e^{-i\omega t} = \frac{-2igA}{\omega}\frac{\cosh\left[k_0(z+h)\right]}{\cosh(k_0h)}\cos(k_0x)e^{-i\omega t} \tag{5.3.14}$$

The excitation force on j-th (stationary) gate is simply

$$F_j^D = i\omega\rho\int_{S_B^j} dy\int_{-h}^{0}\left[\phi^D\right]_{x=0}(z+h)dz = \frac{2\rho gAD_0}{\cosh(k_0h)}\frac{2a}{N} \tag{5.3.15}$$

5.3.2 The lagoon side

On the lagoon side, the radiation potential can be obtained by the Hybrid Finite Element Method. Recall that in examining the effect of each gate, all other gates are assumed to be stationary. Since the problem is in the half plane and all gates are situated on the same vertical plane, the radiation potential due to the motion of any single gate takes on the same form, except for a shift of origin. It is therefore only necessary to consider any one of the gates, say, the j-th gate. The near field, defined by the semi-circular cylinder bounded by C and centered at the center of gate j, is discretized by finite elements. In the super-element outside C, the potential is expressed by the series expansion. We apply the numerical scheme in Section 3.3, where the coordinate system is local. In this local coordinate system, the horizontal displacement of the gate can be expressed as

$$\vec{L} = (z+h)\vartheta(y)e^{-i\omega t}\hat{x}$$

where $\hat{x}$ is the unit vector in x direction. Note that $\vartheta > 0$ if the gate rotates towards lagoon. Then the horizontal velocity of the gate is

$$\dot{\vec{L}} = -i\omega(z+h)\vartheta(y)\hat{x}e^{-i\omega t}$$

Since the normal $\vec{n}$ on the gate surface points outward from the fluid as shown in the figure, matching gate velocity and adjacent fluid for unit angular-displacement amplitude of the gate motion gives the boundary condition on the moving gate

$$\frac{\partial\phi_j^+}{\partial n} = -i\omega(z+h)\hat{x}\cdot(-\hat{x}) = i\omega(z+h), \quad \text{on gate } j \text{ only} \tag{5.3.16}$$

which is to be used in (4.3.15) to calculate K_5. From the numerical solution by the Hybrid Finite Element Method, the radiation potential ϕ_j^l is found.

Let us define F_{pj}^+ to be the exciting force on p-th gate due to the unit amplitude motion of the j-th gate. Then

$$F_{pj}^+ = -i\omega\rho \int_{\frac{2|j-p|a}{N}-\frac{a}{N}}^{\frac{2|j-p|a}{N}+\frac{a}{N}} dr \int_{-h}^{0} \left[\phi_j^+\right]_{\theta=0 \ or \ \theta=\pi} (z+h)dz \tag{5.3.17}$$

where use is made of $\Phi_j^+ = \phi_j^+ e^{-i\omega t}$. For $p = j$, the integral above is carried out numerically.

$$F_{jj}^+ = -i\rho\omega \sum_{el\in S_B} \int_{S_B^+} \phi_j^+(z+h)dS_B^+ = -i\rho\omega \sum_{el\in S_B} \int_{-1}^{+1}\int_{-1}^{+1} \left[(z+h)\mathbf{H}\hat{\phi}det(\mathbf{J})\right]_{\xi=1} d\eta d\zeta$$

For $p \neq j$, we make use of the series expansion (3.3.18) for the super element. Therefore

$$\begin{aligned}
F_{pj}^+ &= -i\omega\rho \int_{\frac{2|j-p|a}{N}-\frac{a}{N}}^{\frac{2|j-p|a}{N}+\frac{a}{N}} \int_{-h}^{0} \{\sum_{m=0}^{\infty}\sum_{n=0}^{\infty} \mu_{mn} \frac{\cosh\left[k_n(z+h)\right]}{\cosh(k_n h)} \frac{H_{2m}^{(1)}(k_n r)}{H_{2m}^{(1)}(k_n r_C)}\}(z+h)drdz \\
&= -i\omega\rho \sum_{m=0}^{\infty}\sum_{n=0}^{\infty} \frac{\mu_{mn}}{\cosh(k_n h)} \int_{\frac{2|j-p|a}{N}-\frac{a}{N}}^{\frac{2|j-p|a}{N}+\frac{a}{N}} \frac{H_{2m}^{(1)}(k_n r)}{H_{2m}^{(1)}(k_n r_C)} dr \int_{-h}^{0} \cosh\left[k_n(z+h)\right](z+h)dz \\
&= -i\omega\rho \sum_{m=0}^{\infty}\sum_{n=0}^{\infty} \frac{\mu_{mn} D_n}{\cosh(k_n h) H_{2m}^{(1)}(k_n r_C)} \int_{\frac{2|j-p|a}{N}-\frac{a}{N}}^{\frac{2|j-p|a}{N}+\frac{a}{N}} H_{2m}^{(1)}(k_n r)dr
\end{aligned}$$

Recall that the local coordinates are used here. It is evident again that $F_{pj}^+ = F_{jp}^+$.

Now the gate dynamics.

In matrix form, the dynamic equations of the N gates are

$$-\omega^2 \mathbf{I}\hat{\vartheta} + \mathbf{C}\hat{\vartheta} = \mathbf{F}^-\hat{\vartheta} + \mathbf{F}^+\hat{\vartheta} + \mathbf{F}^D \tag{5.3.18}$$

where $\mathbf{I}$ and $\mathbf{C}$ are diagonal. $\mathbf{F}^s$ and $\mathbf{F}^l$ are symmetric and their components are defined above with $\mathbf{F}^D$ being a known vector.

We test the HFEM code for a vertical gate with the overall dimensions similar to those of the Malamocco gate. The height is reduced to 20m (about $\frac{2}{3}$ height of prototype gate) and the thickness is kept at $4.5m$. The mass center X_g is 10m above the sea bottom. For the dry weight the gate walls are estimated as 3cm thick steel plate with density being $7700kg \cdot m^{-3}$.). The calculated parameters are as follows: moment of inertia $I = 33.337e6\ kg \cdot m^2$, weight $W = 2619kN$, buoyancy restoring torque $C = 60.246e6\ kg \cdot m^2 \cdot s^{-2}$, gate width $B = 20m$, water depth $h = 14.0m$, density of water $\rho = 1000kg \cdot m^{-3}$, gravity $g = 9.8m \cdot s^{-2}$.

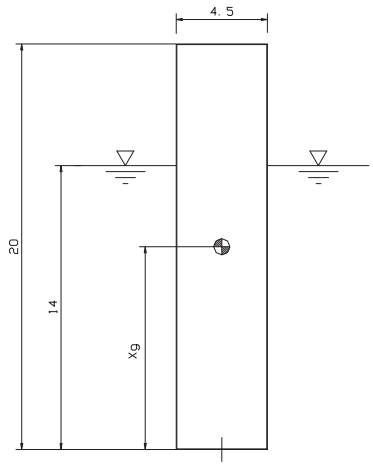

Figure 5.4: Simplified Malamocco flapgate

As an extra check, we have modified the HFEM method by using a rectangular box for the imaginary boundary C, and compare the nodal potentials from the semi-circular imaginary boundary C. Referring to Figure 5.4 and Figure 5.5, the potential values at 13 nodes along the center line of the gate are compared in Table 5.2. The agreement is excellent.

For later application of HFEM to inclined gates, we test the numerical scheme by applying finite elements in front of 5 vertical gates on sea side. In Table 5.3 the hydrodynamic forces F_{ij}^{-} from the analytical solution (5.3.14) are compared with those from numerical computations. The complex values in the table are expressed in the form of $modulus \times 10^7\ kg \cdot m^2 \cdot s^{-2}$ and angle $\angle phase\ angle$. The agreement is excellent.

Next we apply HFEM for 20 vertical gates by using a rectangular imaginary boundary on the lagoon side, and complete the scattering/radiation problem for normally incident waves for a wide range of periods. After accounting for the gate dynamics, the computed maximum gate amplitudes vs. periods are plotted in Figure 5.6. For comparison, the analytical theory by Adamo & Mei (2003) in Report IV are marked in circles. The agreement is also excellent except in certain peak amplitudes. This is likely due to the coarse increments in period in the analytical computation. Finally the computational

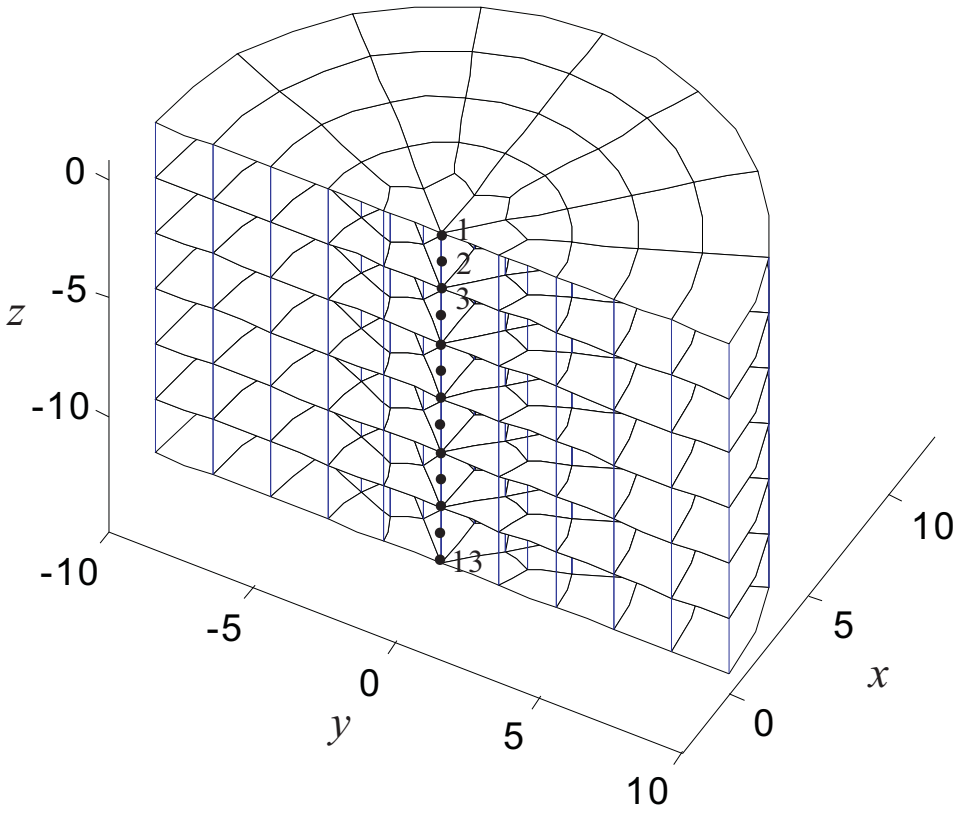

Figure 5.5: Semi-circle boundary and mesh

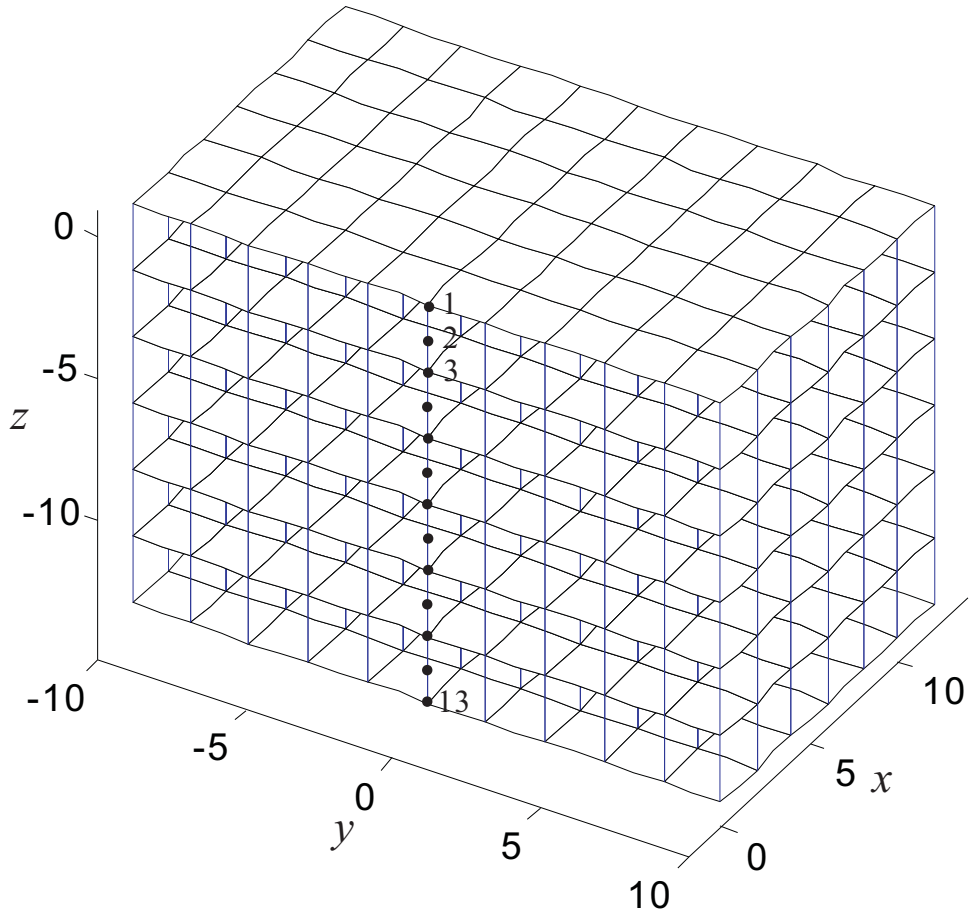

Figure 5.6: Rectangular boundary and mesh

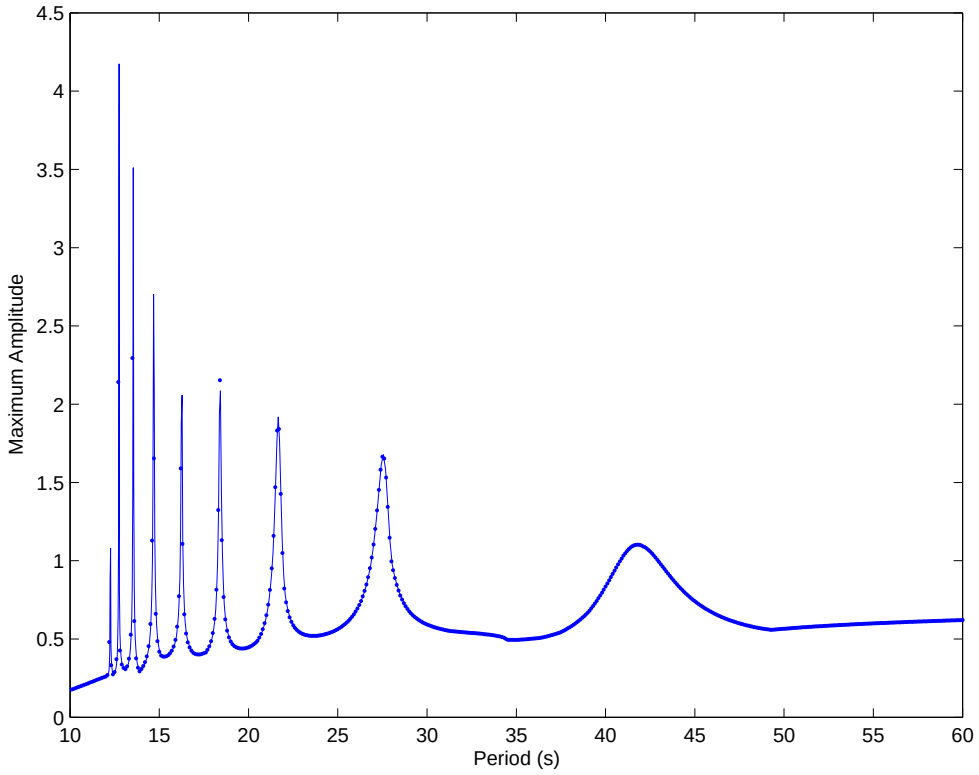

Figure 5.7: Maximum gate amplitudes for a wide range of incident wave periods. The total number of gates is 20.

accuracy is checked by computing the error defined by the difference in energy input and output as derived in Chapter 5,

$$\text{error} = \frac{|E_{in} - E_{out}|}{|E_{in}|} \tag{5.3.19}$$

The error is shown in Figure 5.7, showing good accuracy.

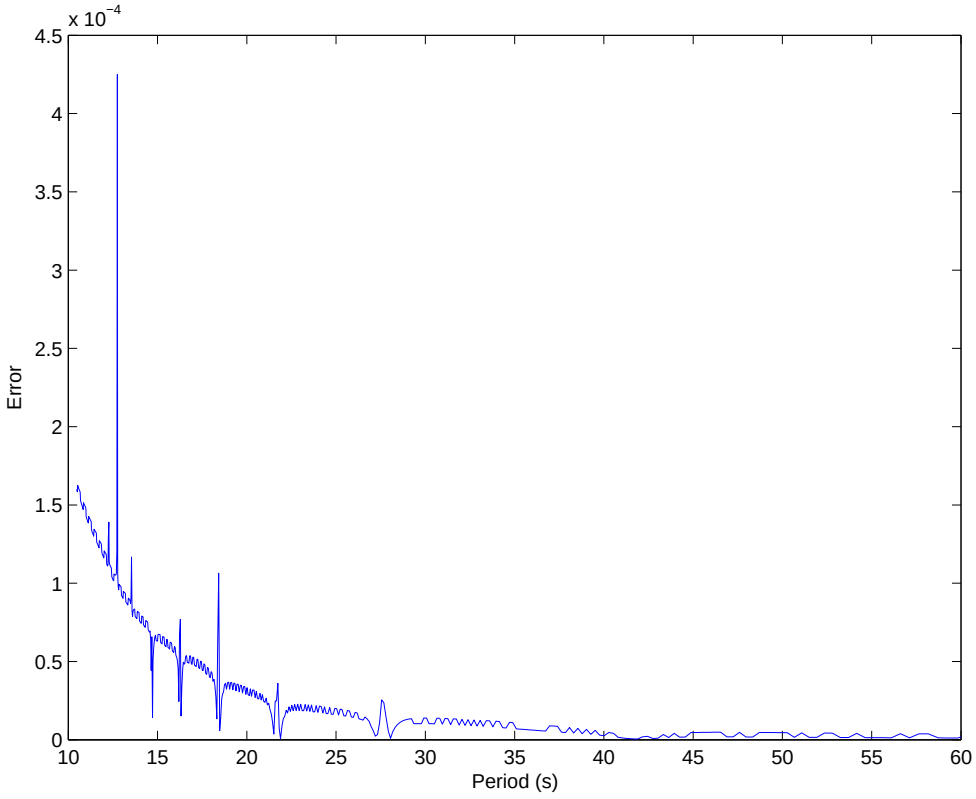

Figure 5.8: The error defined by energy conservation.

Node number	Numerical	Analytical
1	-0.0016 -56.5758i	-56.5806i
2	-0.0016 -55.9094i	-55.9139i
3	-0.0015 -55.2947i	-55.2991i
4	-0.0015 -54.7313i	-54.7355i
5	-0.0015 -54.2186i	-54.2227i
6	-0.0015 -53.7561i	-53.7601i
7	-0.0015 -53.3434i	-53.3473i
8	-0.0015 -52.9802i	-52.9840i
9	-0.0015 -52.6661i	-52.6699i
10	-0.0015 -52.4007i	-52.4045i
11	-0.0015 -52.1840i	-52.1878i
12	-0.0015 -52.0156i	-52.0194i
13	-0.0014 -51.8955i	-51.8992i
14	-0.0014 -51.8234i	-51.8271i
15	-0.0014 -51.7994i	-51.8031i
16	-0.0016 -56.5496i	-56.5544i
17	-0.0016 -55.8835i	-55.8880i
18	-0.0015 -55.2691i	-55.2735i
19	-0.0015 -54.7059i	-54.7101i
20	-0.0015 -54.1934i	-54.1975i

Table 5.1: Comparison of nodal potentials for sea side diffraction

Node number	Semi-circular C	Rectangular C
1	-25.6121 +45.8337i	-25.8621 +46.3792i
2	-25.2623 +44.7986i	-25.5089 +45.2938i
3	-24.9443 +42.5915i	-25.1879 +43.6928i
4	-24.6579 +40.1952i	-24.8986 +41.8085i
5	-24.4026 +38.2469i	-24.6408 +39.7328i
6	-24.1780 +36.1568i	-24.4140 +37.5615i
7	-23.9840 +34.1091i	-24.2181 +35.3621i
8	-23.8202 +32.1003i	-24.0528 +33.2030i
9	-23.6865 +30.2101i	-23.9177 +31.1555i
10	-23.5827 +28.5043i	-23.8129 +29.2896i
11	-23.5086 +27.0760i	-23.7381 +27.7120i
12	-23.4642 +26.0329i	-23.6933 +26.5248i
13	-23.4494 +25.5949i	-23.6783 +25.9987i

Table 5.2: Comparison of nodal potentials for two types of imaginary boundary and mesh scheme

$j \rightarrow$	1	2	3	4	5
$i \downarrow$	mag. : phase°	mag. : phase°	mag. : phase°	mag. : phase°	mag. : phase°
1 anal.	8.9142 :7.1733	4.1764 :15.4579	1.3472 :124.2858	4.9018 :166.8744	7.1987 :171.1047
1 num.	8.9098 :7.1774	4.1769 :15.4570	1.3472 :124.2809	4.9003 :166.8694	7.1963 :171.1011
2 anal.	4.1764 :15.4579	4.2100 :15.3313	1.1132 :89.4604	3.2913 :160.2323	4.9018 :166.8744
2 num.	4.1769 :15.4570	4.2053 :15.3499	1.1133 :89.3579	3.2904 :160.2252	4.9003 :166.8694
3 anal.	1.3472 :124.2858	1.1132 :89.4604	2.0503 :32.880	1.1132 :89.4604	1.3472 :124.2858
3 num.	1.3472 :124.2809	1.1133 :89.3579	2.0470 :32.9444	1.1133 :89.3579	1.3472 :124.2809
4 anal.	4.9018 :166.8744	3.2913 :160.2323	1.1132 :89.464	4.2100 :15.3313	4.1764 :15.4579
4 num.	4.9003 :166.8694	3.2904 :160.2252	1.1133 :89.3579	4.2053 :15.3499	4.1769 :15.4570
5 anal.	7.1987 :171.1047	4.9018 :166.8744	1.3472 :124.2858	4.1764 :15.4579	8.9142 :7.1733
5 num.	7.1963 :171.1011	4.9003 :166.8694	1.3472 :124.2809	4.1769 :15.4570	8.9098 :7.1774

Table 5.3: Comparison of numerical and analytical solutions for hydrodynamic torque F_{ij}^{-}.. (Torque on the sea side of gate j due to unit motion of gate i.)

Chapter 6

Inclined gates

Venice storm gates are designed to operate at the equilibrium inclination of $45^\circ \sim 50^\circ$ from the horizon. To solve the diffraction problem when the gates are stationary, two dimensional finite elements are distributed near the gates on the sea side. For the radiation potentials, three dimensional finite elements are needed on both the sea side and the lagoon side. To reduce computations we take advantage of symmetry for normally incident waves. Only one half of the fluid domain needs to be considered. The finite element domains cover half of the gates in a barrier.

We first discuss the simulation of the 1/30 model of seven gates (two half gates and five full gates) spanning half the inlet. Numerical results for 20 gates spanning Chioggia inlet will be presented.

For the 2-D diffraction potential on the sea side, the finite element mesh is shown in Figure 6.

For the inclined gates, there is no analytical solution. However, the magnitude of the reflection coefficient is expected to be unity. In other words the potential amplitude of the reflected wave in the far field is expected to be the same as that of the incident waves. Recalling (4.4.25), the first mode corresponds the reflected wave (other modes are evanescent). Therefore we can compare the coefficient μ_0 with g/ω from the incident wave. As an example, we use incident period $T = 5.5s$. Therefore $g/\omega = 8.5785$ and we obtain from our numerical method $\mu_0 = -8.4869 - 1.2497i$. The absolute value is $|\mu_0| = 8.5785$ which agrees with the analytical result.

By numerical integration of the pressure on the gate surface, the diffraction torque

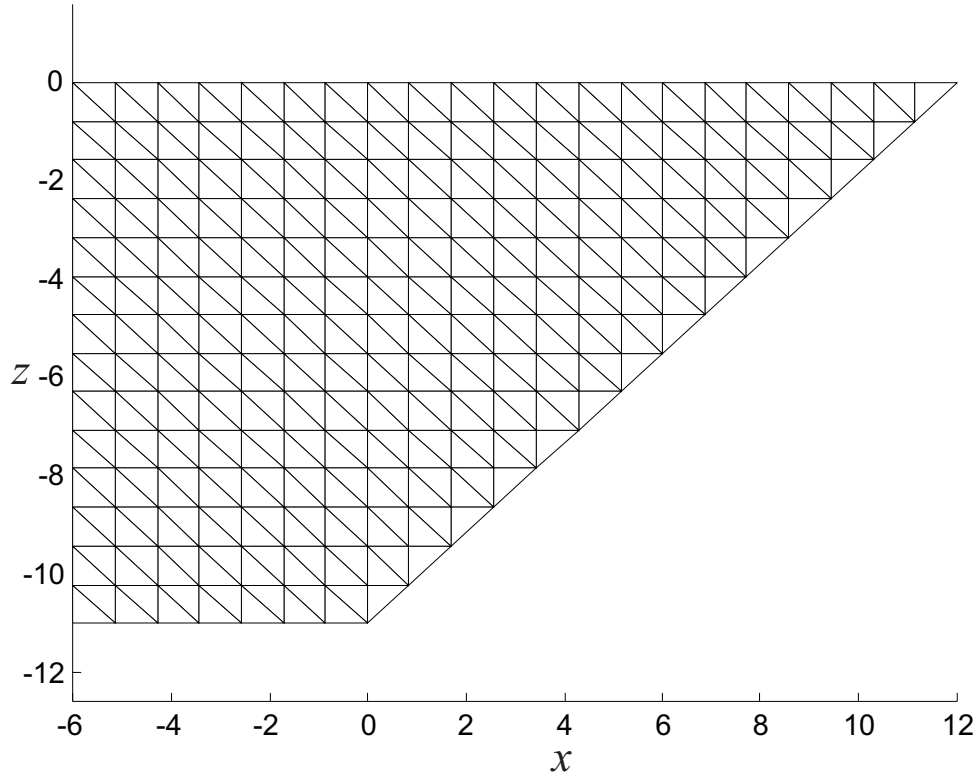

Figure 6.1: Finite element mesh on the sea side of an inclined gate.

is found.

For the 3D radiation problems due to unit motion of one gate, finite elements on the sea side are distributed in front of all gates, as shown in Figure 6.2.

On the lagoon side, the finite elements will be displayed later.

6.1 Comparison with measurements for a 1/30 model

Ing. Alberto Venuti, of Protecno has kindly provided us some information on the Voltaborozzo experiments for a 1/30 model with five whole gates and two half gates spanning one half of the inlet. The following gate data are cited in Table 6.1: In our numerical simulations we use the immersed values in the table. From the geometry the diagonal buoyancy torque $\mathbf{C} = C_{ij} = C\delta_{ij}$ is calculated to be 93,000 kN-m. The depth is $h = 11$ m on both side the gate.

Also we assume that the gates are so situated that at depth $h = 11$ m the water line

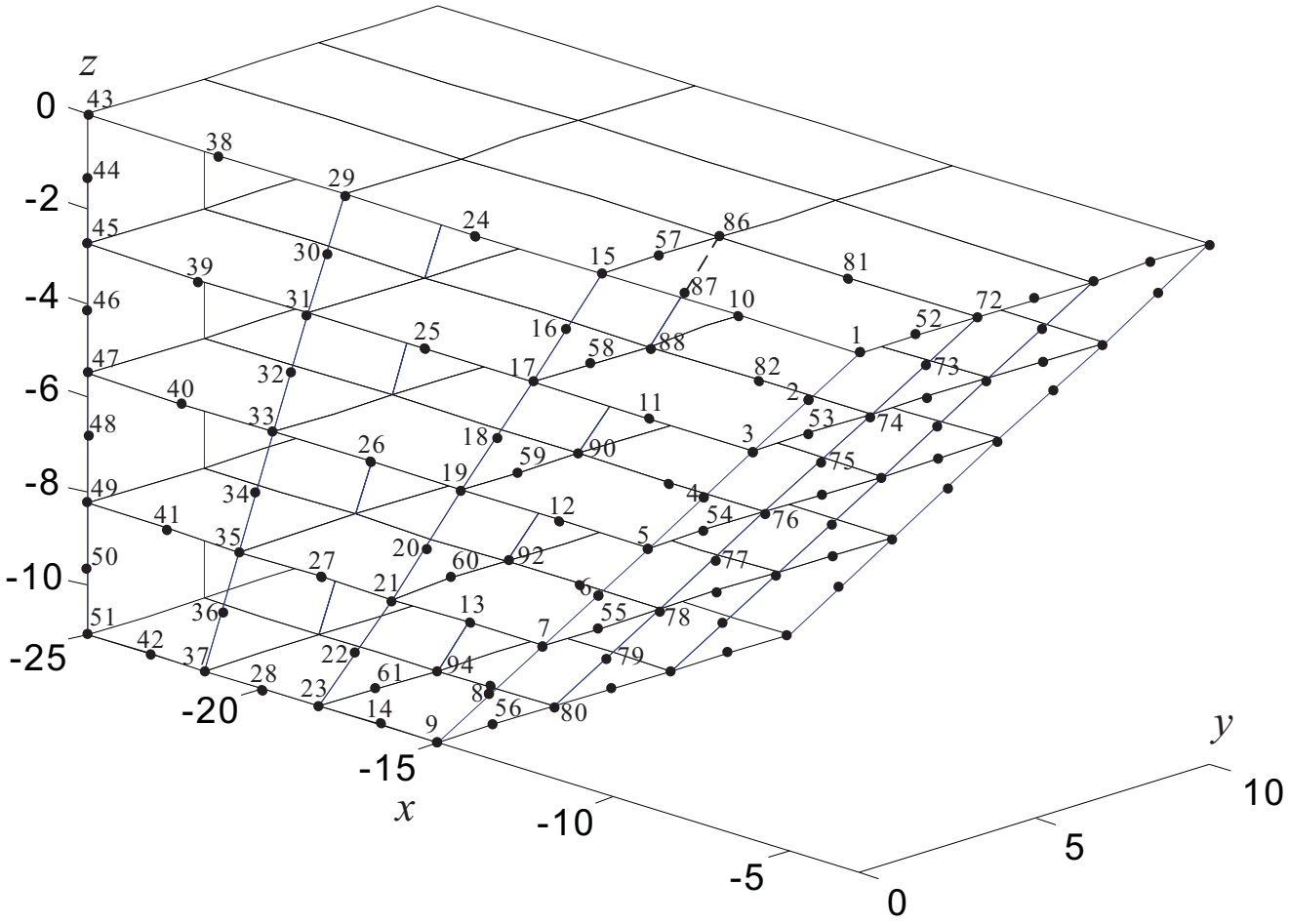

Figure 6.2: Finite element mesh for sea side radiation

on the lagoon side coincides with the coastline.

We report below numerical simulations for 9 tests of regular waves : code named $Reg1002500-30$ to $Reg1302500-30$. Listed in Table 6.2 are the maximum amplitude of the gate rotation (in degrees) for the same (9) incident wave periods, all with the same incident wave height of 2.5m and 0.0m water depth difference. All gates have essentially the same phase, therefore there is no resonance.

With an equilibrium inclination of 42.5 degrees, we plot the maximum absolute oscillations versus period curves in Figure 6.3. For comparison, the CVN data is reproduced in Figure 6.4. The agreement is good.

For the 7 gates model configuration, we have also carried out a series of computations

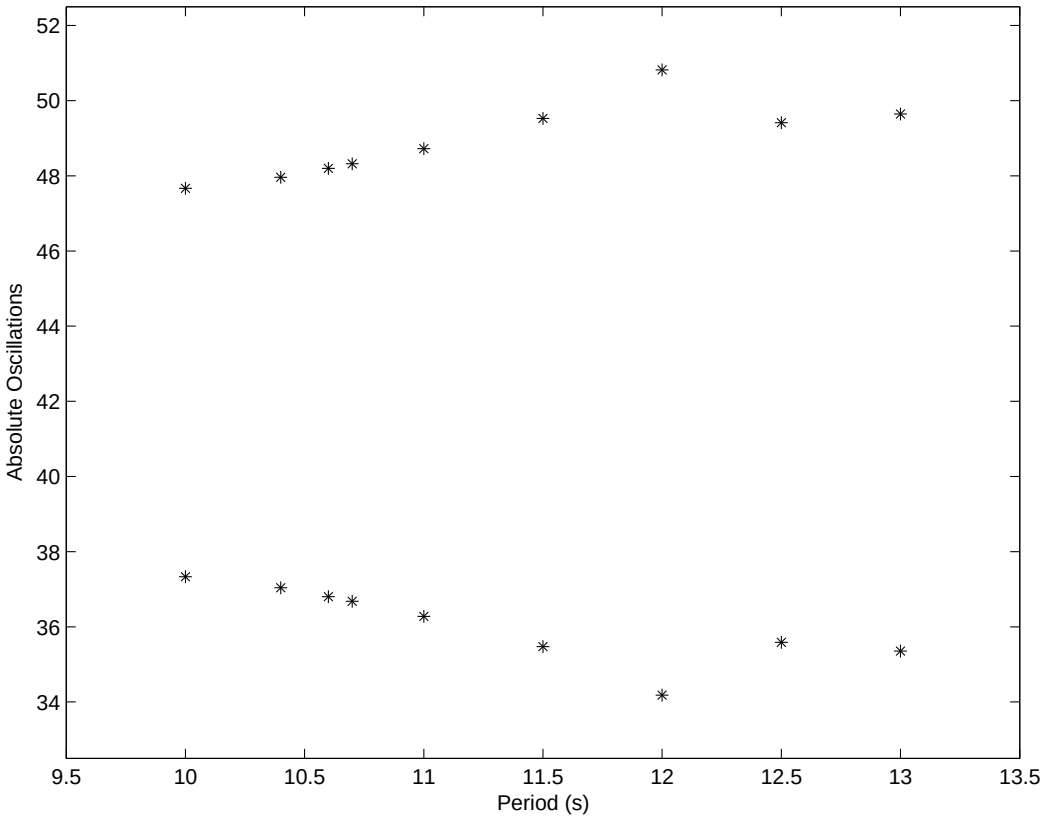

Figure 6.3: Numerical results for maximum absolute oscillations

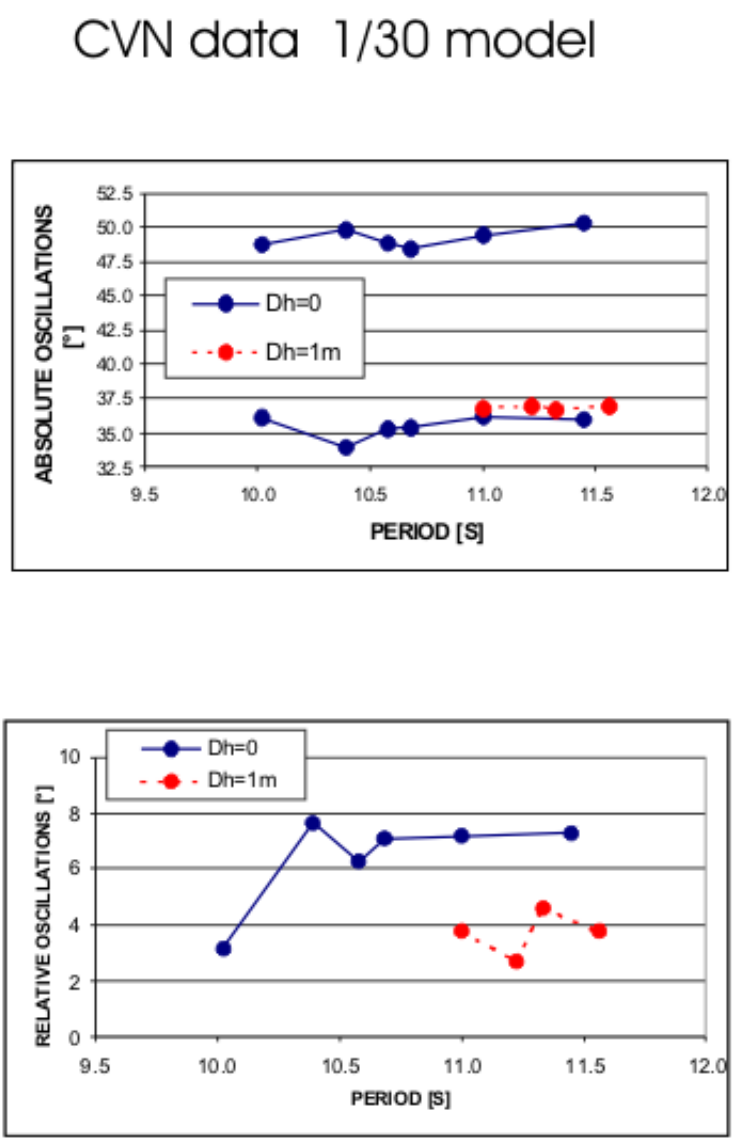

Figure 6.4: Measured absolute oscillations by CVN for 1/30 model

	Immersed conditions	Dry conditions
Weight(kN)	2498.88	3103.65
X center of mass (m)	14.76	13.95
Y center of mass (m)	-1.83	-1.8
Moment of inertia (kg m^2)	85973400	85973400

Table 6.1: Characteristics of 1/30 model in Voltaborozzo experiments

Reg1??2500-30	00	04	06	07	10	15	20	25	30
period (sec)	10.0	10.4	10.6	10.7	11.0	11.5	12.0	12.5	13.0
Ampl (degr..)	5.1698	5.4624	5.6980	5.8221	6.2234	7.0276	8.3192	6.9134	7.1475
Max. (degr.)	47.6698	47.9624	48.1980	48.3221	48.7234	49.5276	59.8192	49.4134	49.6475
Min. (degr.)	37.3302	37.0376	36.8020	36.6766	36.2776	35.4724	34.1808	35.5866	35.3525

Table 6.2: Numerical results for the maximum amplitude of all gates.. Responses to regular waves. The test is identified in the top row according to CVN code: Reg-1??2500-30, etc.

for a wide range of incident wave periods from 9 seconds to 22 seconds. The response curve of maximum amplitude (in radians) versus period is plotted in Figure 6.5. Within this period range, three resonance peaks are found at 16.6 sec, 17.3 sec and 19.5 sec respectively. The first peak with the lowest period (highest frequency) corresponds to Mode 1 resonance in which the neighboring gates are in opposite phase and all gate amplitudes are essentially equal. The complex amplitudes of the seven gates are listed in Table 6.3 and the modal shape is shown in Figure 6.6. That the resonance period is so much longer than the earlier designs ($\sim 12.5 sec$) may be explained by the new and much larger gate dimensions and weight.

The corresponding error curve by energy conservation is plotted in Figure 6.7. The maximum error is less than 0.25 percent, and is acceptable.

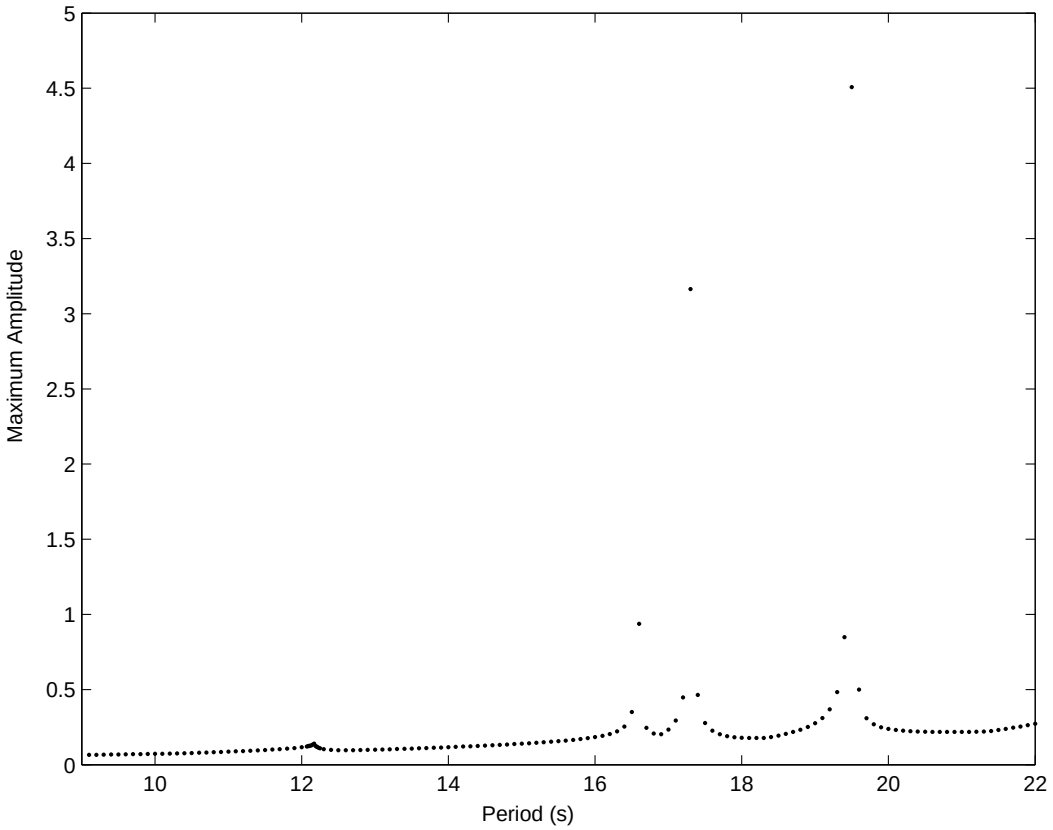

Figure 6.5: Numerical results for maximum amplitude of the 7 gates on a range of period

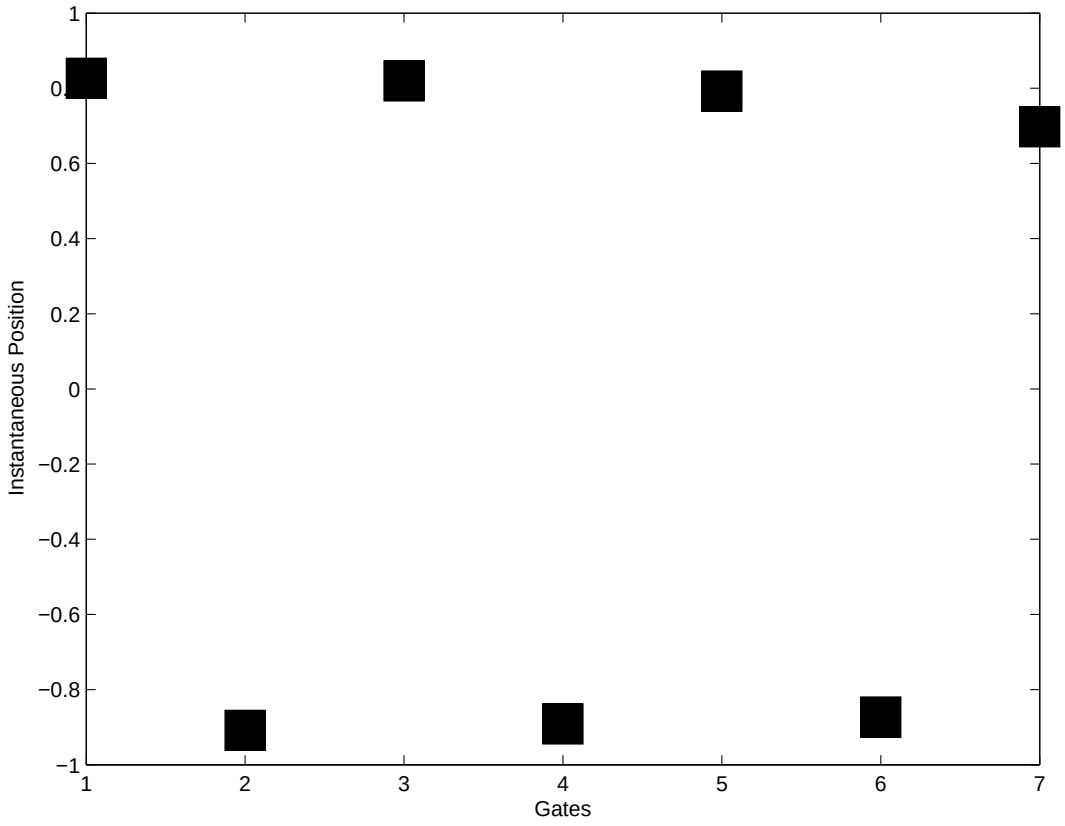

Figure 6.6: Modal shape of the seven gate in response to 16.6 sec incident wave.

Gate 1	Gate 2	Gate 3	Gate 4
0.827+0.0074i	-0.909+0.228i	0.82+0.0041i	-0.891+0.217i
Gate 5	Gate 6	Gate 7	
0.793-0.0058i	-0.873+0.197i	0.70-0.0133i	

Table 6.3: Complex amplitudes of seven gates in response to 16.6 sec. incident wave. Gate 1 and gate 7 are half gates at the center and the edge of the inlet.

6.2 Response of a 20-gates barrier to regular incident waves

As the final example, we now apply our HFEM code for a 20-gates barriers with the design dimensions of Chioggia Inlet, as specified in the 1/30 model of Volraborozzo. In addition, the housing is included. The finite element meshes are shown in Figure 6.8 for a side view of the center plane. The top view is shown in Figure 6.9. A three-dimensional perspective is shown in Figure 6.10. Note that the design geometry of the gate and the housing are included[1].

Figure 6.11 shows the single frequency response of maximum gate amplitude for incident waves of 2.5m wave height. The gates move in phase at the minor peak at period 13 sec . At the second major peak of 16.8 sec, neighboring gates are in opposite phases as can be inferred from the complex amplitudes listed in Table 6.4. As a further proof we show in Figure 6.12 the gate positions. Note that not only are neighboring gates in opposite phases. but the envelope has a minimum at the edge and at the center of the inlet, and maximum at the quarter point of the inlet. This is precisely as predicted in Figure 9, p. 14. Report Part III July 10, 2003!!!

The energy error of these computations are shown in Figure 6.13, and is quite acceptable.

With the potentials and gate displacements found, other design information such as the total torque on each gate can be calculated.

[1]Using Matlab the reader can view the grids at any angle.

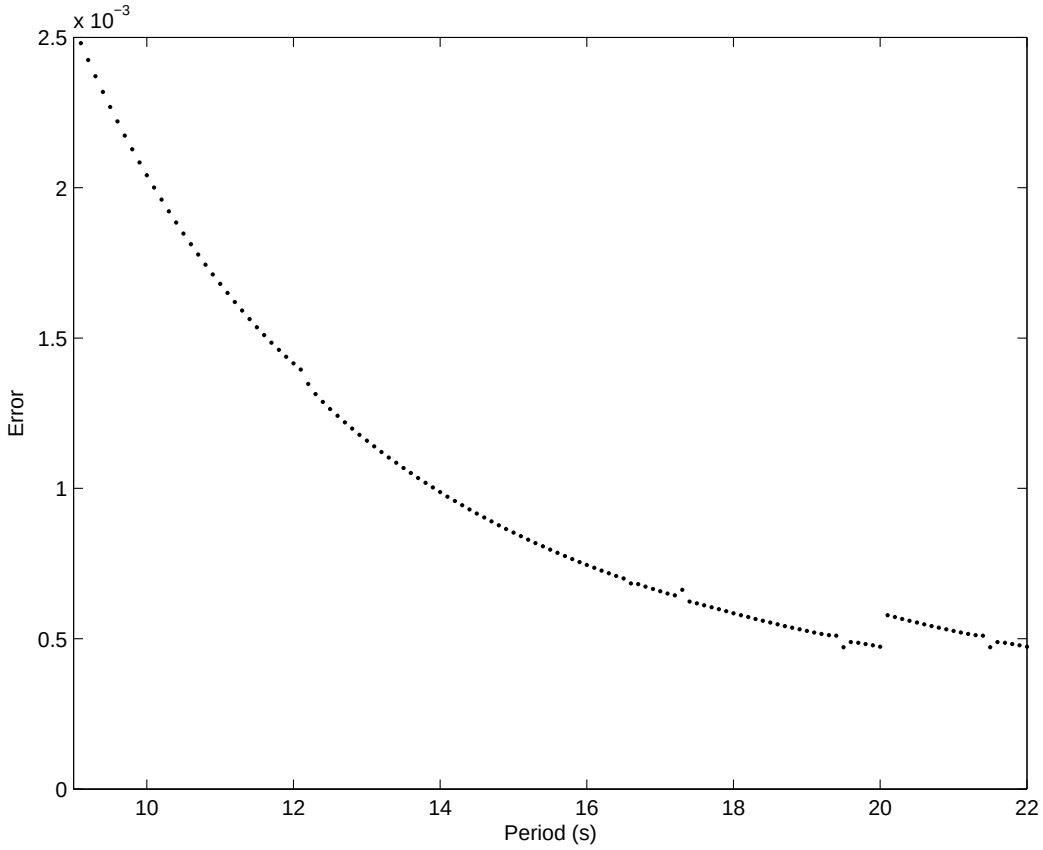

Figure 6.7: Error defined by energy conservation for the 7-gates model.

Gate 1	Gate 2	Gate 3	Gate 4	Gate 5
-0.0215 + 0.1104i	-0.1193 + 0.1243i	0.0729 + 0.1000i	-0.1893 + 0.1364i	0.1284 + 0.0944i
Gate 6	Gate 7	Gate 8	Gate 9	Gate 10
-0.2123 + 0.1391i	0.1231 + 0.0914i	-0.1829 + 0.1273i	0.0530 + 0.0886i	-0.1351 + 0.1060i

Table 6.4: Complex amplitudes of 10 gates (one half of Chioggia Inlet barrier) in response to incident wave of period =16.8 sec.

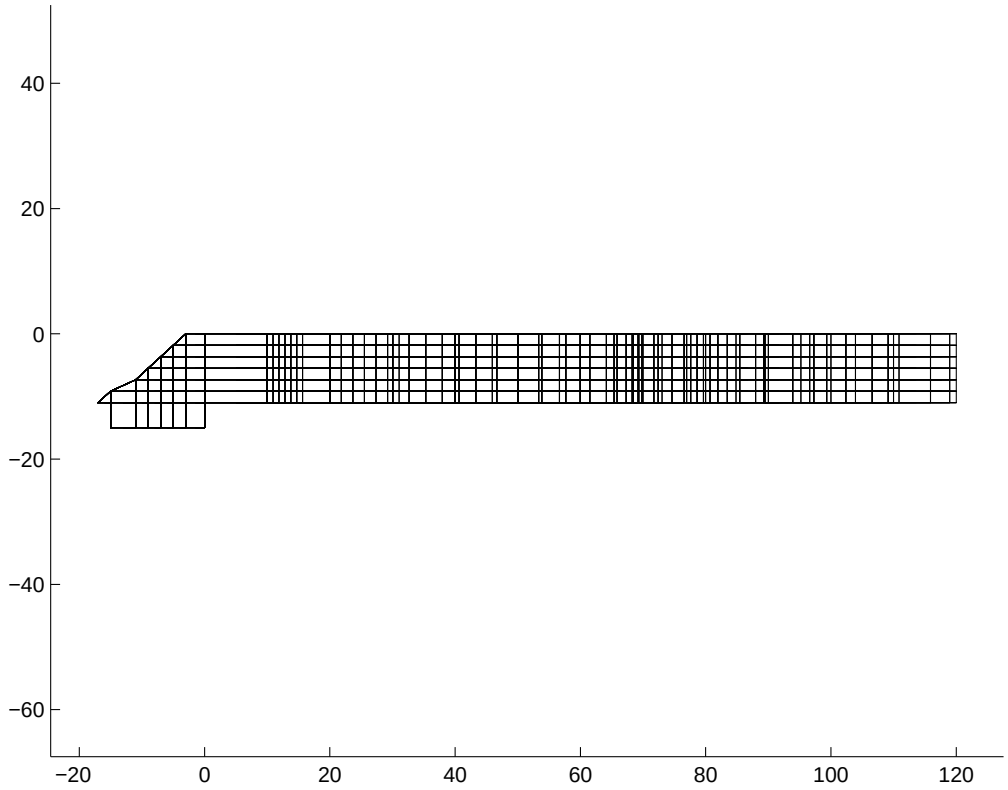

Figure 6.8: Finite element mesh for lagoon side radiation– perspective from the center plane along the x-axis. Mesh lines in vertical planes parallel to the centerplanes are also seen.

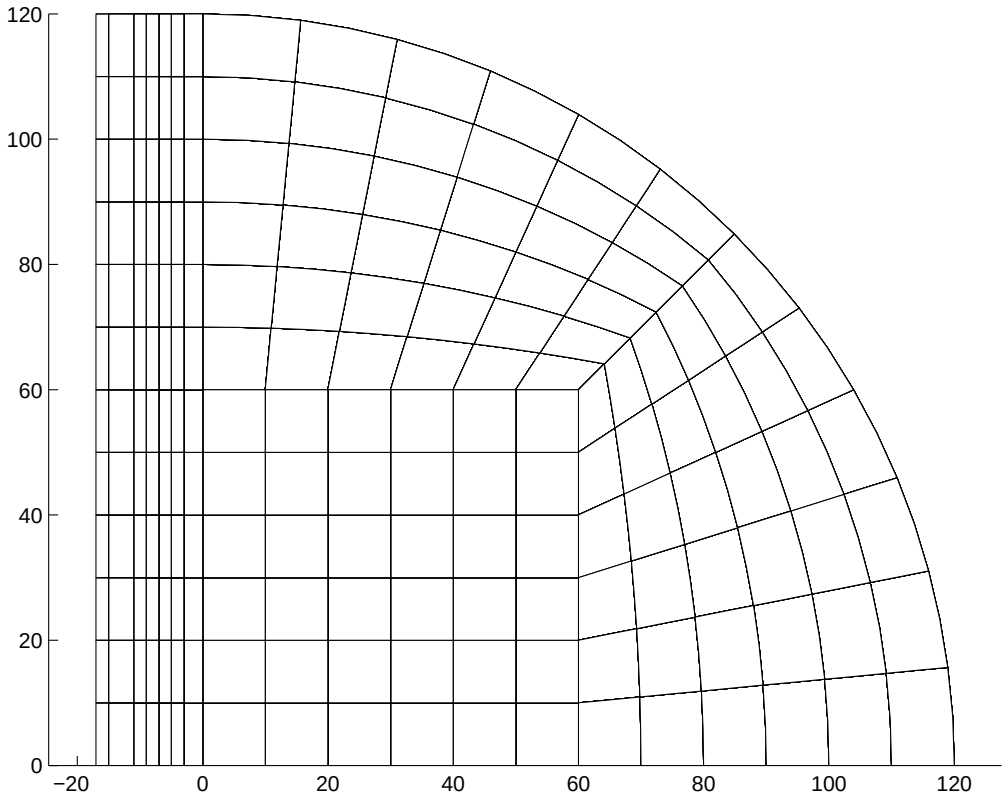

Figure 6.9: Finite element mesh for lagoon side radiation–the top view.

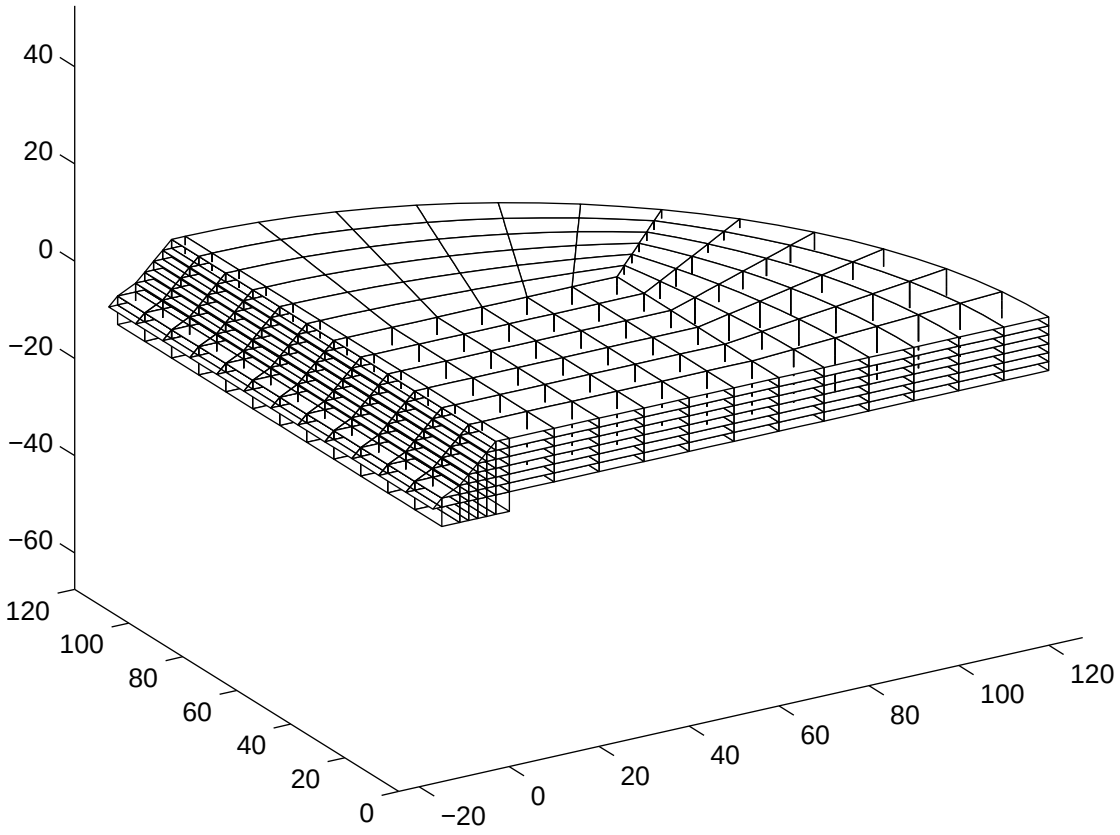

Figure 6.10: Finite element mesh for lagoon side radiation–the 3-D perspective

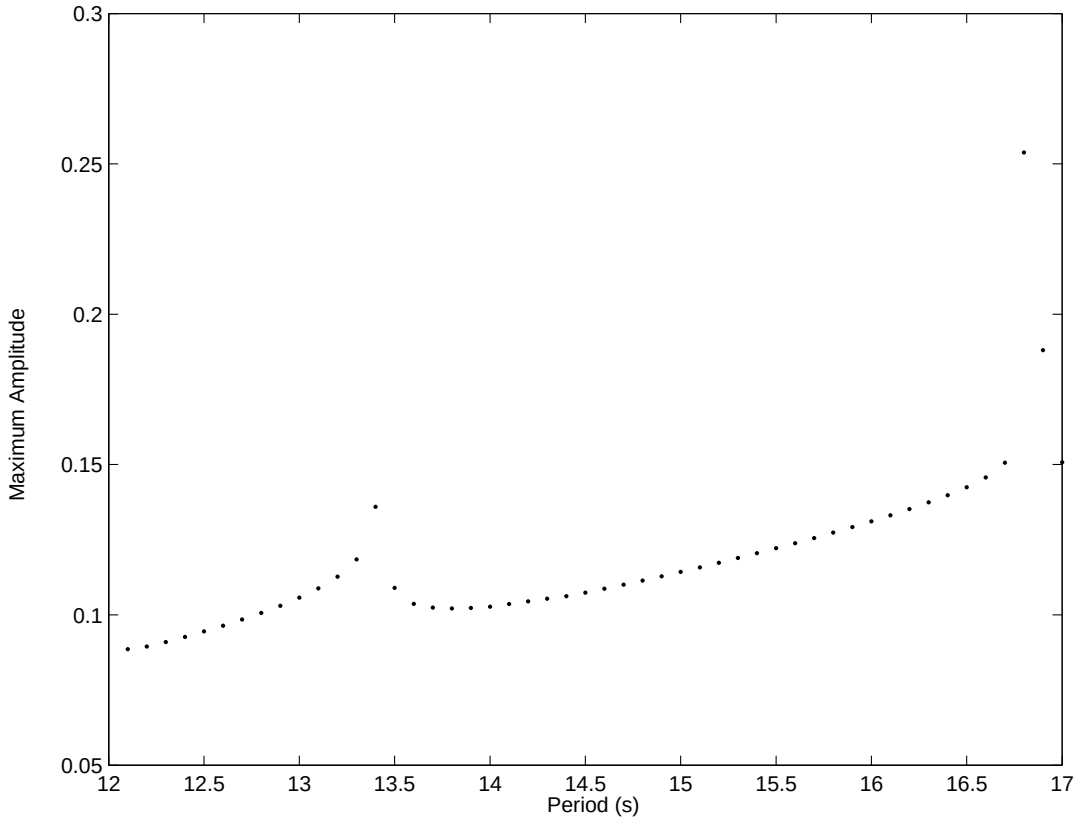

Figure 6.11: Single-frequency response of the 20-gates barrier to regular incident wave. Maximum gate amplitude is in radians. The peak at 16.8 sec corresponds to out-of-phase resonance of Mode N 2. the peak at 13 sec show in- phase motion only.

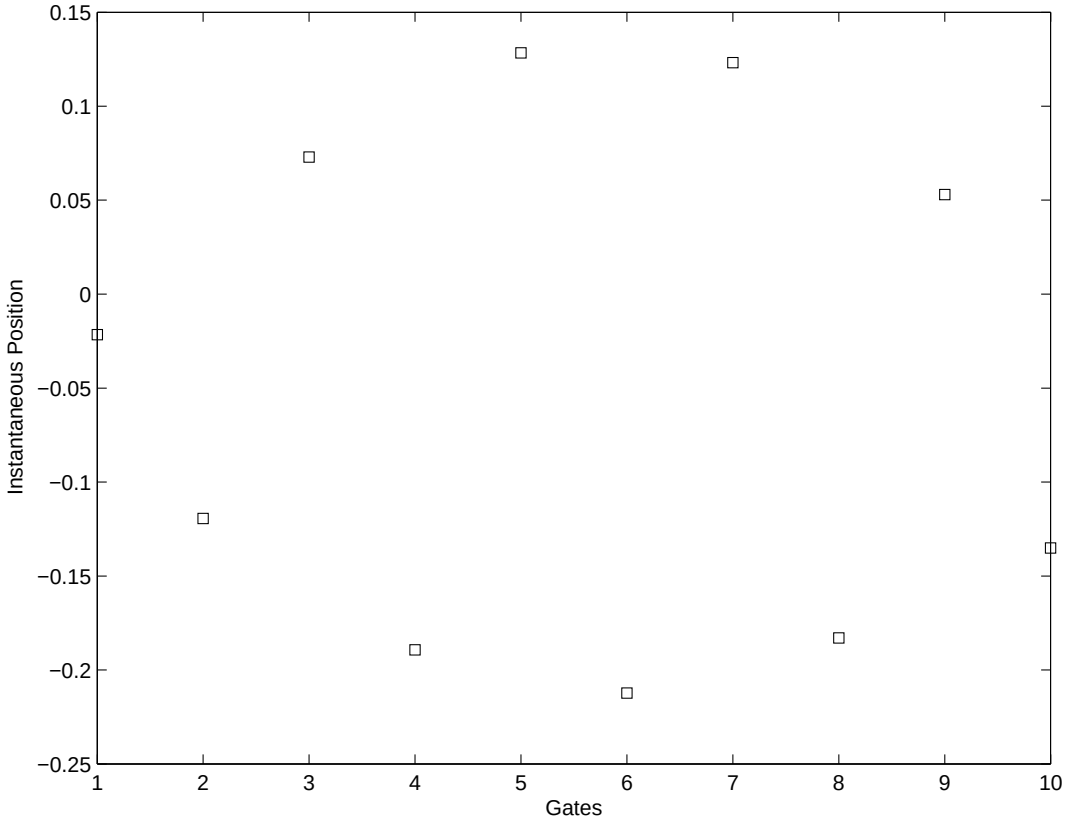

Figure 6.12: Modal shape of the 20-gates in response to 16.8 sec incident wave. Only one half of the symmetric inlet (10 gates) is shown.

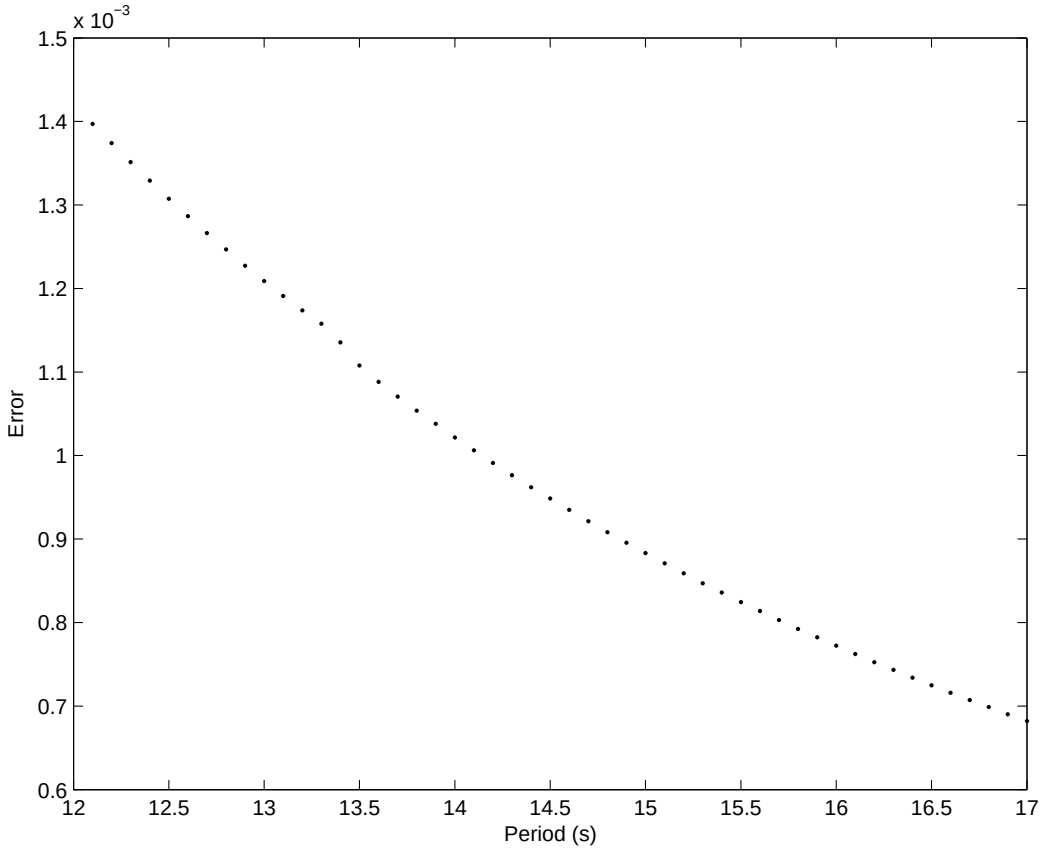

Figure 6.13: Error defined by energy conservation for the 20-gates barrier.

Chapter 7

Concluding remarks

For the linear response of multi-gates barrier spanning an inlet with jetties only on the seaside, both the theory and computer codes are now fully developed for inclined gates with the complex gate geometry fully accounted for. Details are recorded in the manual. The mathematical tool developed here can now be used to adjust the dimensions, the inclination and the water depths, in order to minimize the danger of resonance.

To ensure greater safety in future operations, further study of gate response to random incident waves with proper account of subharmonic resonance is important and is proposed.

Appendix A

Energy conservation

A.1 Energy fluxes

Physically the incident wave energy on the sea side must be equal to the radiated wave energy outflux on both sides. This identity can be derived by Green's theorem, as shown in Adamo & Mei (2003) for vertical gates, and will not be repeated here.

We first write down the energy fluxes in terms of the far-field solutions, and evaluate the fluxes for vertical and inclined gates separately.

Using the global coordinate system defined in the Figure A.1, we express the total potential Φ as

$$\Phi(x, y, z, t) = \mathcal{R}e\{\varphi(x, y, z)e^{-i\omega t}\} \tag{A.1.1}$$

The dynamical pressure is

$$p = -\rho\Phi_t = \mathcal{R}e\{i\rho\omega\varphi e^{-i\omega t}\}$$

Consider first the energy influx across a straight cross section in the far field of the channel side $x = X$,

$$E_{in} = \overline{\int_0^a \int_{-h}^0 pu \; dy \; dz} = \int_0^a \int_{-h}^0 \overline{pu} \; dy \; dz = \int_0^a \int_{-h}^0 \frac{1}{2}\mathcal{R}e\{i\rho\omega\varphi\varphi_x^*\} \; dy \; dz$$

In the far field of the lagoon, the energy outflux across the circular cylinder $r = R$ is

$$E_{out} = \overline{\int_{-\frac{\pi}{2}}^{\frac{\pi}{2}} \int_{-h}^0 puRd\varphi dz} = \int_{-\frac{\pi}{2}}^{\frac{\pi}{2}} \int_{-h}^0 \frac{1}{2}\mathcal{R}e\{i\rho\omega\varphi\varphi_r^*\}Rd\sigma dz$$

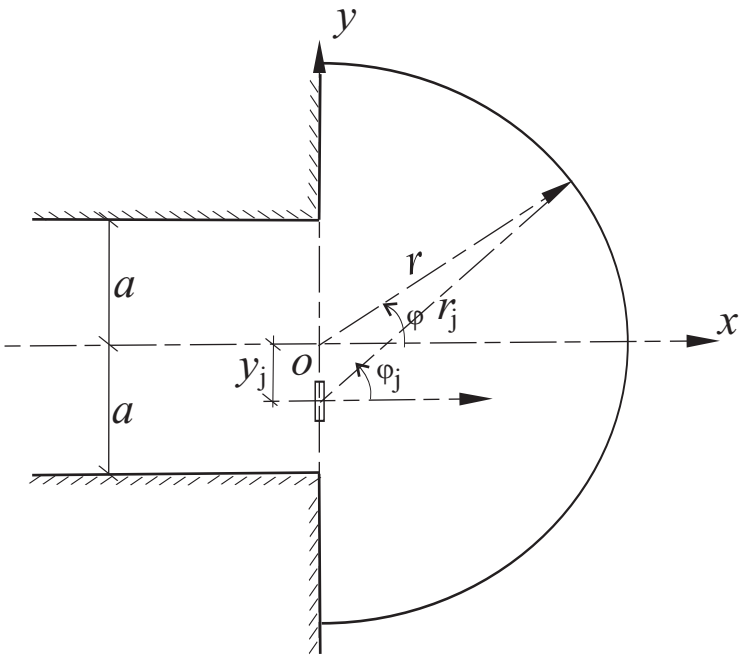

Figure A.1: Relation between local and global coordinate system

Equating the two fluxes, the identity of energy conservation(which can be derived by Green's theorem), reads

$$E_{in} = E_{out} \Rightarrow \left\{ \int_0^a \int_{-h}^0 \mathcal{I}m\{\varphi\varphi_x^*\}\ dy\ dz \right\}_{x=X} = \left\{ \int_{-\frac{\pi}{2}}^{\frac{\pi}{2}} \int_{-h}^0 \mathcal{I}m\{\varphi\varphi_r^*\} R d\sigma dz \right\}_{r=R}$$

For late checks of numerical accuracy we define the energy error as

$$\text{error} = \frac{|E_{in} - E_{out}|}{|E_{in}|} \tag{A.1.2}$$

We now express the energy fluxes in terms of the gate displacement amplitudes. It is convenient to treat the vertical and inclined gates separately.

A.2 Vertical gates

A.2.1 Sea side

On the sea side at $x = X \sim -\infty$,

$$\varphi = \varphi^I + \varphi^R + \varphi^- = \varphi^D + \sum \phi_j^- \vartheta_j$$

where φ^D is the diffraction potential due to incident and reflected wave as in (5.3.14)

$$\varphi^D = \frac{-2ig}{\omega}\frac{\cosh\left[k_0(z+h)\right]}{\cosh(k_0h)}\cos(k_0x) \tag{A.2.3}$$

with unit incident wave amplitude $A = 1$. Normalized for unit rotation amplitude, ϕ_j^- is the radiation potential due to the oscillation of jth gate, as in (5.3.13). By retaining only the propagating mode for large X, we get for the radiated waves due the motion of gate j,

$$\begin{aligned}\phi_j^- &\sim \frac{\omega}{N}\frac{D_0}{C_0k_0}\cosh\left[k_0(z+h)\right]e^{-ik_0x} \\ &+ \sum_{m=1}^{M}\frac{\omega D_0}{m\pi C_0\alpha_{m0}}\left[\sin(\frac{(2j-N)m\pi}{N}) - \sin(\frac{(2(j-1)-N)m\pi}{N})\right] \\ &\cos\frac{m\pi y}{a}\cosh\left[k_0(z+h)\right]e^{-i\alpha_{m0}x}\end{aligned} \tag{A.2.4}$$

where

$$\alpha_{m0} = \sqrt{k_0^2 - (\frac{m\pi}{a})^2}$$

and M is the maximum m for real α_{m0}.

$$\begin{aligned}\frac{\partial\phi_j^-}{\partial x} &\sim \frac{-i\omega}{N}\frac{D_0}{C_0}\cosh\left[k_0(z+h)\right]e^{-ik_0x} \\ &+ \sum_{m=1}^{M}\frac{-i\omega D_0}{m\pi C_0}\left[\sin(\frac{(2j-N)m\pi}{N}) - \sin(\frac{(2(j-1)-N)m\pi}{N})\right] \\ &\cos\frac{m\pi y}{a}\cosh\left[k_0(z+h)\right]e^{-i\alpha_{m0}x}\end{aligned}$$

Therefore, the total potential is

$$\begin{aligned}\varphi &\sim \frac{-2ig}{\omega}\frac{\cosh\left[k_0(z+h)\right]}{\cosh(k_0h)}\cos(k_0x) + \sum_{j=1}^{N}\vartheta_j\left\{\frac{\omega}{N}\frac{D_0}{C_0k_0}\cosh\left[k_0(z+h)\right]e^{-ik_0x}\right. \\ &+ \sum_{m=1}^{M}\frac{\omega D_0}{m\pi C_0\alpha_{m0}}\left[\sin(\frac{(2j-N)m\pi}{N}) - \sin(\frac{(2(j-1)-N)m\pi}{N})\right] \\ &\left.\cos\frac{m\pi y}{a}\cosh\left[k_0(z+h)\right]e^{-i\alpha_{m0}x}\right\}\end{aligned}$$

and the complex conjugate of the total velocity is

$$\begin{aligned}{\varphi_x}^* &= \frac{-2igk_0}{\omega}\frac{\cosh\left[k_0(z+h)\right]}{\cosh(k_0h)}\sin(k_0x) + \sum_{j=1}^{N}\vartheta_j^*\left\{\frac{i\omega}{N}\frac{D_0}{C_0}\cosh\left[k_0(z+h)\right]e^{ik_0x}\right. \\ &+ \left.\sum_{m=1}^{M}\frac{i\omega D_0}{m\pi C_0}\left[\sin(\frac{(2j-N)m\pi}{N}) - \sin(\frac{(2(j-1)-N)m\pi}{N})\right]\cos\frac{m\pi y}{a}\cosh\left[k_0(z+h)\right]e^{i\alpha_{m0}x}\right\}\end{aligned}$$

Defining the following real parameters from brevity

$$a_0 = \frac{-2g}{\omega \cosh(k_0 h)}; \quad b_0 = \frac{\omega D_0}{N C_0 k_0}; \quad b_m(p) = \frac{\omega D_0}{m\pi C_0 \alpha_{m0}} \left[\sin(\frac{(2j-N)m\pi}{N}) - \sin(\frac{(2(j-1)-N)m\pi}{N}) \right],$$

then

$$\begin{aligned} \varphi {\varphi_x}^* &= \cosh^2\left[k_0(z+h)\right] \left\{ i a_0 \cos(k_0 x) + \sum_{p=1}^{N} \vartheta_p \left[b_0 e^{-ik_0 x} + \sum_{m=1}^{M} b_m(p) \cos\frac{m\pi y}{a} e^{-i\alpha_{m0} x} \right] \right\} \\ & \left\{ i k_0 a_0 \sin(k_0 x) + \sum_{q=1}^{N} \vartheta_q^* \left[i k_0 b_0 e^{ik_0 x} + \sum_{m=1}^{M} b_m(q) i\alpha_{m0} \cos\frac{m\pi y}{a} e^{i\alpha_{m0} x} \right] \right\} \end{aligned}$$

The energy influx is

$$\begin{aligned} \int_{-a}^{a}\int_{-h}^{0} \mathcal{I}m\{\varphi {\varphi_x}^*\}\, dy\, dz &= 2C_0 a \mathcal{I}m \left\{ i a_0 \cos(k_0 x) \sum_{q=1}^{N} \vartheta_q^* \left(i k_0 b_0 e^{ik_0 x} \right) \right\} \\ &+ 2C_0 a \mathcal{I}m \left\{ i k_0 a_0 \sin(k_0 x) \sum_{p=1}^{N} \vartheta_p \left(b_0 e^{-ik_0 x} \right) \right\} \\ &+ 2C_0 a \mathcal{I}m \left\{ \sum_{p=1}^{N}\sum_{q=1}^{N} \vartheta_p \vartheta_q^* i k_0 b_0^2 \right\} \\ &+ C_0 \mathcal{I}m \left\{ \sum_{p=1}^{N}\sum_{q=1}^{N} \vartheta_p \vartheta_q^* \sum_{m=1}^{M} b_m(p) b_m(q) i\alpha_{m0} \int_{-a}^{a} \cos^2\frac{m\pi y}{a} dy \right\} \\ &= -2C_0 a k_0 a_0 b_0 \cos^2(k_0 x) \mathcal{I}m \left\{ \sum_{q=1}^{N} \vartheta_q^* \right\} \\ &+ 2C_0 a k_0 a_0 b_0 \sin^2(k_0 x) \mathcal{I}m \left\{ \sum_{p=1}^{N} \vartheta_p \right\} \\ &+ 2C_0 a k_0 b_0^2 \mathcal{R}e \left\{ \sum_{p=1}^{N}\sum_{q=1}^{N} \vartheta_p \vartheta_q^* \right\} \\ &+ C_0 \mathcal{R}e \left\{ \sum_{p=1}^{N}\sum_{q=1}^{N} \vartheta_p \vartheta_q^* \sum_{m=1}^{M} b_m(p) b_m(q) \alpha_{m0} \int_{-a}^{a} \cos^2\frac{m\pi y}{a} dy \right\} \\ &= 2C_0 a k_0 a_0 b_0 \mathcal{I}m \left\{ \sum_{j=1}^{N} \vartheta_j \right\} \\ &+ 2C_0 a k_0 b_0^2 \mathcal{R}e \left\{ \sum_{p=1}^{N}\sum_{q=1}^{N} \vartheta_p \vartheta_q^* \right\} \\ &+ C_0 a \mathcal{R}e \left\{ \sum_{p=1}^{N}\sum_{q=1}^{N} \vartheta_p \vartheta_q^* \sum_{m=1}^{M} b_m(p) b_m(q) \alpha_{m0} \right\} \end{aligned}$$

Some terms have disappeared due to either the orthogonality of $\cos\frac{m\pi y}{a}$ or being purely real. Use has been made of the general identities

$$\mathcal{I}m\left\{A\right\} = -\mathcal{I}m\left\{A^*\right\}; \quad (AB)^* = A^*B^*$$

A.2.2 Lagoon side

On the lagoon side, there are only radiated waves,

$$\varphi = \varphi^+ = \sum \phi_j^+ \vartheta_j$$

where ϕ_j^+ is the radiation potential due to the rotation of j-th gate at unit amplitude, as in (3.3.16). Referring to figure (A.1), we now employ the local coordinate system, whose origin is located at the center of the jth gate, and has the global coordinate $(0, Y_j, 0)$.In the far field (large R), we exclude evanescent modes corresponding to imaginary $k_n = i\bar{k}_n, n = 1, 2, ...$

$$\phi_j^+ = \sum_{m=0}^{\infty} \nu_{m0} \frac{\cosh\left[k_0(z+h)\right]}{\cosh(k_0 h)} \frac{H_{2m}^{(1)}(k_0 r_j)}{H_{2m}^{(1)}(k_0 r_C)} \cos 2m\sigma_j \tag{A.2.5}$$

In the far field, $\frac{y_j}{r} \ll 1$, we have the approximate relation between local and global coordinates up to the first order:

$$r_j = \sqrt{r^2 + Y_j^2 - 2rY_j \sin\sigma} \simeq r\left(1 - \frac{Y_j}{r}\sin\sigma + ...\right); \quad \sigma_j \simeq \sigma - \frac{Y_j}{r}\cos\sigma + ...$$

where use has been made of the laws of cosines and sines. By Taylor expansion,

$$\cos 2m\sigma_j = \cos\left[2m\left(\sigma - \frac{Y_j}{r}\cos\sigma + ...\right)\right] = \cos 2m\sigma + 2m\frac{Y_j}{r}\sin 2m\sigma\cos\sigma + ...$$

Making use of the asymptotic form of Hankel functions for large argument

$$H_n^{(1)}(x) \simeq \sqrt{\frac{2}{\pi x}} e^{i\left[x - \left(n+\frac{1}{2}\right)\frac{\pi}{2}\right]}$$

it follows that

$$H_{2m}^{(1)}(k_0 r_j) = \sqrt{\frac{2}{\pi k_0 r}} e^{i(k_0 r - m\pi - \frac{\pi}{4})} e^{-ik_0 y_j \sin\sigma} + O\left(\frac{Y_j}{r}\sqrt{\frac{1}{k_0 r}}\right)$$

and,

$$\frac{\partial\phi_j^+}{\partial r} = \sum_{m=0}^{\infty} \frac{\nu_{m0}\cosh\left[k_0(z+h)\right]}{H_{2m}^{(1)}(k_0 r_C)\cosh(k_0 h)} ik_0 \left[\sqrt{\frac{2}{\pi k_0 r}} e^{i(k_0 r - m\pi - \frac{\pi}{4})} e^{-ik_0 Y_j \sin\sigma}\cos 2m\sigma + O\left(\frac{1}{k_0 r}\sqrt{\frac{1}{k_0 r}}\right)\right]$$

$$\begin{aligned}
\varphi^{+}\varphi_r^{+*} &= \sum_{p=1}^{N}\sum_{q=1}^{N}\vartheta_p\phi_p^{+}\vartheta_q^{*}\frac{\partial\phi_q^{+*}}{\partial r} \\
&= \frac{\cosh^2\left[k_0(z+h)\right]}{\cosh^2(k_0h)}\sum_{p=1}^{N}\sum_{q=1}^{N}\vartheta_p\vartheta_q^{*}\sum_{m=0}^{\infty}\frac{\mu_{m0}}{H_{2m}^{(1)}(k_0r_C)}\sum_{n=0}^{\infty}\frac{\mu_{n0}^{*}}{H_{2n}^{(1)*}(k_0r_C)} \\
&\quad \left[\frac{-2i}{\pi r}e^{i(n-m)\pi}e^{-ik_0(Y_p-Y_q)\sin\sigma}\cos 2m\sigma\cos 2n\sigma\right]
\end{aligned}$$

The total energy outflux is

$$\begin{aligned}
\int_{-\frac{\pi}{2}}^{\frac{\pi}{2}}\int_{-h}^{0}\mathcal{I}m\{\varphi^{+}\varphi_r^{+*}\}Rd\sigma dz &= \mathcal{I}m\left\{\frac{-2iC_0}{\pi\cosh^2(k_0h)}\sum_{p=1}^{N}\sum_{q=1}^{N}\sum_{m=0}^{\infty}\sum_{n=0}^{\infty}\frac{\nu_{m0}\nu_{n0}^{*}\vartheta_p\vartheta_q^{*}e^{i(n-m)\pi}}{H_{2m}^{(1)}(k_0r_C)H_{2n}^{(1)*}(k_0r_C)}\right. \\
&\quad \left.\int_{-\frac{\pi}{2}}^{\frac{\pi}{2}}d\sigma\left[e^{-ik_0(Y_p-Y_q)\sin\sigma}\cos 2m\sigma\cos 2n\sigma\right]\right\} \\
&= \frac{-2C_0}{\pi\cosh^2(k_0h)}\mathcal{R}e\left\{\sum_{p=1}^{N}\sum_{q=1}^{N}\sum_{m=0}^{\infty}\sum_{n=0}^{\infty}\frac{\nu_{m0}\nu_{n0}^{*}\vartheta_p\vartheta_q^{*}e^{i(n-m)\pi}}{H_{2m}^{(1)}(k_0r_C)H_{2n}^{(1)*}(k_0r_C)}\right. \\
&\quad \left.\int_{-\frac{\pi}{2}}^{\frac{\pi}{2}}d\sigma\left[e^{-ik_0(Y_p-Y_q)\sin\sigma}\cos 2m\sigma\cos 2n\sigma\right]\right\}
\end{aligned}$$

Finally, equating the energy fluxes gives the following identity

$$\begin{aligned}
2C_0ak_0a_0b_0\mathcal{I}m\left\{\sum_{j=1}^{N}\vartheta_j\right\} &+ 2C_0ak_0b_0^2\mathcal{R}e\left\{\sum_{p=1}^{N}\sum_{q=1}^{N}\vartheta_p\vartheta_q^{*}\right\} \\
&+ C_0a\mathcal{R}e\left\{\sum_{p=1}^{N}\sum_{q=1}^{N}\vartheta_p\vartheta_q^{*}\sum_{m=1}^{M}b_m(p)b_m(q)\alpha_{m0}\right\} \\
&= \frac{-2C_0}{\pi\cosh^2(k_0h)}\mathcal{R}e\left\{\sum_{p=1}^{N}\sum_{q=1}^{N}\sum_{m=0}^{\infty}\sum_{n=0}^{\infty}\frac{\nu_{m0}\nu_{n0}^{*}\vartheta_p\vartheta_q^{*}e^{i(n-m)\pi}}{H_{2m}^{(1)}(k_0r_C)H_{2n}^{(1)*}(k_0r_C)}\right. \\
&\quad \left.\int_{-\frac{\pi}{2}}^{\frac{\pi}{2}}d\sigma\left[e^{-ik_0(Y_p-Y_q)\sin\sigma}\cos 2m\sigma\cos 2n\sigma\right]\right\} \qquad \text{(A.2.6)}
\end{aligned}$$

which must be satisfied by the computed gate amplitudes ϑ_j for $j = 1, ..., N$. Note that this identity is expressed in terms of the global coordinates.

The identity (A.2.6) is the basis of the error defined later in (5.3.19) for checking the numerical accuracy shown in figure 5.7.

A.3 Inclined gates

On the sea side on the far field surface $x = X \sim -\infty$,

$$\varphi = \varphi^D + \sum_{j=1}^{N} \phi_j^- \vartheta_j$$

where φ^D is the diffraction potential due to the sum of the prescribed incident wave

$$\varphi^I = \frac{-ig}{\omega} \frac{\cosh\left[k_0(z+h)\right]}{\cosh(k_0 h)} e^{ik_0 x} \tag{A.3.7}$$

and the unknown reflected wave as in (4.4.25)

$$\varphi^R = \mu_0 \frac{\cosh\left[k_0(z+h)\right]}{\cosh k_0 h} e^{-ik_0 x} \tag{A.3.8}$$

Note that the evanescent modes are excluded for large X and the complex coefficient μ_0 must be found by the 2-D HFEM. On the other hand the normalized radiation potential ϕ_j^+ due to the unit motion of jth gate is given by (4.3.16). Keeping only the propagating mode, we get

$$\phi_j^- = \sum_{m=0}^{M} \mu_{m0}^j \cos\frac{m\pi y}{a} \frac{\cosh\left[k_0(z+h)\right]}{\cosh(k_0 h)} e^{-i\alpha_{m0} x}$$

where

$$\alpha_{m0} = \sqrt{k_0^2 - (\frac{m\pi}{a})^2}$$

and M is the maximum m for real α_{m0}. Thus,

$$\frac{\partial \phi_j^-}{\partial x} = \sum_{m=0}^{M} -i\alpha_{m0}\mu_{m0}^j \cos\frac{m\pi y}{a} \frac{\cosh\left[k_0(z+h)\right]}{\cosh(k_0 h)} e^{-i\alpha_{m0} x}$$

Unlike vertical gates the coefficients μ_{m0} must be found numerically by 3-D HFEM. We can now calculate for $x = X$ the total potential,

$$\begin{aligned} \varphi &= \frac{-ig}{\omega} \frac{\cosh\left[k_0(z+h)\right]}{\cosh(k_0 h)} e^{ik_0 x} + \mu_0 e^{-ik_0 x} \frac{\cosh\left[k_0(z+h)\right]}{\cosh k_0 h} \\ &+ \sum_{j=1}^{N} \vartheta_j \left\{ \sum_{m=0}^{M} \mu_{m0}^j \cos\frac{m\pi y}{a} \frac{\cosh\left[k_0(z+h)\right]}{\cosh(k_0 h)} e^{-i\alpha_{m0} x} \right\} \end{aligned}$$

and

$$\begin{aligned} \varphi_x{}^* &= \frac{k_0 g}{\omega} \frac{\cosh\left[k_0(z+h)\right]}{\cosh(k_0 h)} e^{-ik_0 x} + ik_0 \mu_0^* e^{ik_0 x} \frac{\cosh\left[k_0(z+h)\right]}{\cosh k_0 h} \\ &+ \sum_{j=1}^{N} \vartheta_j^* \left\{ \sum_{m=0}^{M} i\alpha_{m0}\mu_{m0}^{j*} \cos\frac{m\pi y}{a} \frac{\cosh\left[k_0(z+h)\right]}{\cosh(k_0 h)} e^{i\alpha_{m0} x} \right\} \end{aligned}$$

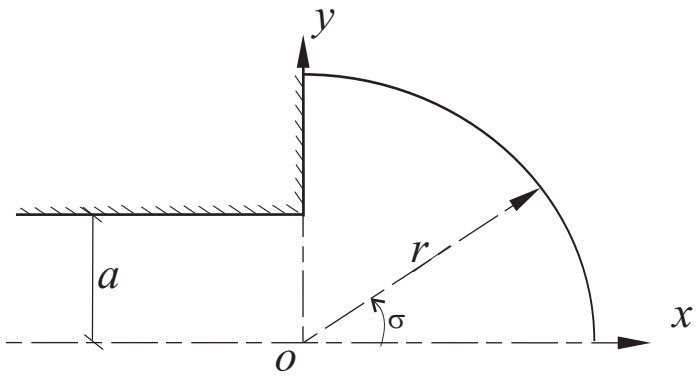

Figure A.2: Global coordinate system on lagoon side

The total energy influx across $x = X$ due to diffraction and radiation on the Adriatic side is

$$\begin{aligned}
\int_0^a \int_{-h}^0 \mathcal{I}m\{\varphi {\varphi_x}^*\}\, dy\, dz &= \frac{C_0}{\cosh^2(k_0 h)} \mathcal{I}m \left\{ k_0 a \frac{g}{\omega} \mu_0^* e^{2ik_0 x} + k_0 a \frac{g}{\omega} \mu_0 e^{-2ik_0 x} \right. \\
&+ \sum_{j=1}^N \vartheta_j^* k_0 a \frac{g}{\omega} \mu_{00}^{j*} e^{2ik_0 x} + \sum_{j=1}^N \vartheta_j k_0 a \frac{g}{\omega} \mu_{00}^j e^{-2ik_0 x} \\
&- ik_0 a \frac{g^2}{\omega^2} + iak_0 \mu_0 \mu_0^* + \sum_{j=1}^N \vartheta_j^* iak_0 \mu_0 \mu_{00}^{j*} \\
&+ \left. \sum_{j=1}^N \vartheta_j iak_0 \mu_0^* \mu_{00}^j + \sum_{p=1}^N \sum_{q=1}^N \vartheta_p \vartheta_q^* \sum_{m=0}^M \mu_{m0}^p \mu_{m0}^{q*} i\alpha_{m0} \frac{a}{\epsilon_m} \right\} \\
&= \frac{C_0}{\cosh^2(k_0 h)} \mathcal{I}m \left\{ -ik_0 a \frac{g^2}{\omega^2} + iak_0 \mu_0 \mu_0^* \right. \\
&+ \left. 2i\mathcal{I}m \left\{ \sum_{j=1}^N \vartheta_j^* iak_0 \mu_0 \mu_{00}^{j*} \right\} + \sum_{p=1}^N \sum_{q=1}^N \vartheta_p \vartheta_q^* \sum_{m=0}^M \mu_{m0}^p \mu_{m0}^{q*} i\alpha_{m0} \frac{a}{\epsilon_m} \right\} \\
&= \frac{C_0}{\cosh^2(k_0 h)} \mathcal{R}e \left\{ -k_0 a \frac{g^2}{\omega^2} + ak_0 \mu_0 \mu_0^* + \sum_{j=1}^N 2\vartheta_j^* ak_0 \mu_0 \mu_{00}^{j*} \right. \\
&+ \left. \sum_{p=1}^N \sum_{q=1}^N \vartheta_p \vartheta_q^* \sum_{m=0}^M \mu_{m0}^p \mu_{m0}^{q*} \alpha_{m0} \frac{a}{\epsilon_m} \right\}
\end{aligned}$$

Some terms have disappeared due to either the orthogonality of $\cos \frac{m\pi y}{a}$ or being pure real.

On the lagoon side, it is now more convenient to use only the global coordinate system as shown in figure A.3. Therefore, the far field solution for potential due to

the motion of one generic gate is the series expansion (3.3.18). We emphasize that for different gate, the series coefficients ν_{mn} are different. On the large semi-circle with $r = R$, we exclude evanescent modes with imaginary $k_n (n = 1, 2, ...)$. The potential due to the oscillation of gate j is

$$\phi_j^+ = \sum_{m=0}^{\infty} \nu_{m0}^j \frac{\cosh\left[k_0(z+h)\right]}{\cosh(k_0 h)} \frac{H_{2m}^{(1)}(k_0 r)}{H_{2m}^{(1)}(k_0 r_C)} \cos 2m\sigma \tag{A.3.9}$$

Therefore,

$$\frac{\partial \phi_j^+}{\partial r} = \sum_{m=0}^{\infty} \nu_{m0}^j \frac{\cosh\left[k_0(z+h)\right]}{\cosh(k_0 h)} \frac{H_{2m}^{(1)'}(k_0 r)}{H_{2m}^{(1)}(k_0 r_C)} k_0 \cos 2m\sigma$$

for gate j and

$$\begin{aligned}
\varphi^+ \varphi_r^{+*} &= \sum_{p=1}^{N}\sum_{q=1}^{N} \vartheta_p \phi_p \vartheta_q^* \frac{\partial \phi_q}{\partial r}^* \\
&= \frac{\cosh^2\left[k_0(z+h)\right]}{\cosh^2(k_0 h)} \sum_{p=1}^{N}\sum_{q=1}^{N} \vartheta_p \vartheta_q^* \sum_{m=0}^{\infty} \frac{\nu_{m0}^p}{H_{2m}^{(1)}(k_0 r_C)} \sum_{n=0}^{\infty} \frac{\nu_{n0}^{q*}}{H_{2n}^{(1)*}(k_0 r_C)} \\
&\quad \left[H_{2m}^{(1)}(k_0 r) \cos 2m\sigma H_{2n}^{(1)'*}(k_0 r) k_0 \cos 2n\sigma\right]
\end{aligned}$$

for all gates. The total energy outflux is

$$\begin{aligned}
&\int_0^{\frac{\pi}{2}} \int_{-h}^{0} \mathcal{I}m\{\varphi^+ \varphi_r^{+*}\} R d\sigma dz = \mathcal{I}m \left\{ \frac{k_0 C_0 R}{\cosh^2(k_0 h)} \sum_{p=1}^{N}\sum_{q=1}^{N}\sum_{m=0}^{\infty} \nu_{m0}^p \nu_{m0}^{q*} \vartheta_p \vartheta_q^* \right. \\
&\left. \frac{H_{2m}^{(1)}(k_0 r) H_{2m}^{(1)'*}(k_0 r)}{H_{2m}^{(1)}(k_0 r_C) H_{2m}^{(1)*}(k_0 r_C)} \int_0^{\frac{\pi}{2}} \left(\cos 2m\sigma\right)^2 d\sigma \right\} \\
= \; & \frac{\pi k_0 C_0 R}{2\cosh^2(k_0 h)} \mathcal{I}m \left\{ \sum_{p=1}^{N}\sum_{q=1}^{N}\sum_{m=0}^{\infty} \nu_{m0}^p \nu_{m0}^{q*} \vartheta_p \vartheta_q^* \frac{H_{2m}^{(1)}(k_0 r) H_{2m}^{(1)'*}(k_0 r)}{\epsilon_m H_{2m}^{(1)}(k_0 r_C) H_{2m}^{(1)*}(k_0 r_C)} \right\}
\end{aligned} \tag{A.3.10}$$

For large argument, we replace the Hankel function by its asymptotic form

$$H_n^{(1)}(x) \simeq \sqrt{\frac{2}{\pi x}} e^{i\left[x - \left(n+\frac{1}{2}\right)\frac{\pi}{2}\right]}$$

and

$$H_n^{(1)'}(x) \simeq i\sqrt{\frac{2}{\pi x}} e^{i\left[x - \left(n+\frac{1}{2}\right)\frac{\pi}{2}\right]} + O\left(\frac{1}{x}\sqrt{\frac{1}{x}}\right)$$

Therefore

$$H_{2m}^{(1)}(k_0 r) = \sqrt{\frac{2}{\pi k_0 r}} e^{i(k_0 r - m\pi - \frac{\pi}{4})}$$

and

$$H_{2m}^{(1)'*}(k_0 r) = -i\sqrt{\frac{2}{\pi k_0 r}} e^{-i(k_0 r - m\pi - \frac{\pi}{4})}$$

Substituting these into (A.3.10), we get

$$\begin{aligned}
&\int_0^{\frac{\pi}{2}} \int_{-h}^{0} \mathcal{I}m\{\varphi^{+}\varphi_r^{+*}\} R d\sigma dz \\
= \;& \frac{C_0}{\cosh^2(k_0 h)} \mathcal{I}m \left\{ \sum_{p=1}^{N} \sum_{q=1}^{N} \sum_{m=0}^{\infty} \frac{-i\nu_{m0}^{p} \nu_{m0}^{q*} \vartheta_p \vartheta_q^*}{\epsilon_m H_{2m}^{(1)}(k_0 r_C) H_{2m}^{(1)*}(k_0 r_C)} \right\} \\
= \;& \frac{C_0}{\cosh^2(k_0 h)} \mathcal{R}e \left\{ \sum_{p=1}^{N} \sum_{q=1}^{N} \sum_{m=0}^{\infty} \frac{-\nu_{m0}^{p} \nu_{m0}^{q*} \vartheta_p \vartheta_q^*}{\epsilon_m H_{2m}^{(1)}(k_0 r_C) H_{2m}^{(1)*}(k_0 r_C)} \right\}
\end{aligned}$$

Finally, the energy conservation identity reads

$$\begin{aligned}
&\frac{C_0}{\cosh^2(k_0 h)} \mathcal{R}e \left\{ a k_0 \mu_0 \mu_0^* - k_0 a \frac{g^2}{\omega^2} + \sum_{j=1}^{N} 2\vartheta_j^* a k_0 \mu_0 \mu_{00}^{j*} + \sum_{p=1}^{N} \sum_{q=1}^{N} \vartheta_p \vartheta_q^* \sum_{m=0}^{M} \nu_{m0}^{p} \nu_{m0}^{q*} \alpha_{m0} \frac{a}{\epsilon_m} \right\} \\
&\qquad = \frac{C_0}{\cosh^2(k_0 h)} \mathcal{R}e \left\{ \sum_{p=1}^{N} \sum_{q=1}^{N} \sum_{m=0}^{\infty} \frac{-\nu_{m0}^{p} \nu_{m0}^{q*} \vartheta_p \vartheta_q^*}{\epsilon_m H_{2m}^{(1)}(k_0 r_C) H_{2m}^{(1)*}(k_0 r_C)} \right\}
\end{aligned}$$

which must be satisfied by the numerically computed coefficients μ_{mo} and amplitudes ϑ_p. This will be used for checking the correctness and accuracy of the numerical computations by our 2-D and 3-D schemes of HFEM.